IDENTIFICATION OF ALBITITE ZONE USING MULTISENSOR DATA IN EASTERN RAJASTHAN

Ph.D. Thesis

by

Poonam S. Tiwari

DEPARTMENT OF EARTH SCIENCES
INDIAN INSTITUTE OF TECHNOLOGY ROORKEE
ROORKEE- 247 667 (INDIA)

MARCH, 2013

IDENTIFICATION OF ALBITITE ZONE USING MULTISENSOR DATA IN EASTERN RAJASTHAN

A THESIS

Submitted in Partial fulfilment of the

requirements for the award of the degree

of

DOCTOR OF PHILOSOPHY

in

DEPARTMENT OF EARTH SCIENCES

by

POONAM S. TIWARI

DEPARTMENT OF EARTH SCIENCES
INDIAN INSTITUTE OF TECHNOLOGY ROORKEE
ROORKEE- 247 667 (INDIA)

MARCH, 2013

INDIAN INSTITUTE OF TECHNOLOGY ROORKEE
ROORKEE

CANDIDATE'S DECLARATION

I hereby certify that the work which is being presented in the thesis entitled "**Identification of Albitite Zone Using Multisensor Data in Eastern Rajasthan"** in partial fulfilment of the requirements for the award of the degree of Doctor of Philosophy and submitted in Department of Earth Sciences of the Indian Institute of Technology Roorkee, Roorkee is an authentic record of my own work carried out during a period from January 2008 to July 2013 under the supervision of Dr. A.K. Sen, Professor, Department of Earth Sciences, Dr. R.D. Garg, Associate Professor, Geomatics Engineering Group, Department of Civil Engineering, Indian Institute of Technology Roorkee, Roorkee and Dr. V.K. Dadhwal, Director, National Remote Sensing Centre, ISRO, Department of Space, Government of India, Hyderabad.

The matter presented in the thesis has not been submitted by me for the award of any other degree of this or any other Institute.

(Poonam S.Tiwari)

This is to certify that the above statement made by the candidate is correct to the best of our knowledge.

(V.K. Dadhwal)	(R.D. Garg)	(A.K. Sen)
Supervisor	Supervisor	Supervisor

Date:

The Ph.D Viva-Voce Examination of **Ms. Poonam S. Tiwari**, Research Scholar, Department of Earth Sciences, has been held on …….

Signature of Supervisors Chairman, SRC External Examiner

Head of the Department/Chairman, ODC

Contents

	Page no.
Abstract	
Acknowledgement	
Contents	
List of Figures	
List of Tables	
Chapter 1: Introduction	1
1.1 General Background	1
1.2 Motivation	7
1.3 Objectives	8
1.4 Scientific Impact	8
1.5 Organization of the thesis	9
Chapter 2: Study Area and its Literature Review	11
2.1 Literature Review of the study area	11
2.2 Literature Review of Geologic Remote Sensing for Mineral mapping	14
2.2.1 Multispectral Remote Sensing for Mineral identification	14
2.2.2 ASTER data for Mineral mapping	16
2.3 Literature Review Of Cartosat-1 Stereo Processing And DEM Applications For Geomorphological Mapping	19
2.4. Study Area	20
2.4.1 Physiography	21
2.4.2 Geology	22
2.4.3 Albtite Zone	27
Chapter 3: Materials and Methods	29
3.1 Remote sensing image data	29
3.1.1 ASTER	29
3.1.2 Landsat	31
3.1.3 Cartosat-1	31

3.2 Ancillary data and creation of a GIS database	32
3.2.1 Base Map	33
3.2.2 Drainage Map	34
3.2.3 Contour Map	35
3.2.1 Geology Map	36
3.2.1 Lineament Map	36
3.3 Field and laboratory data	37
3.4 Software tools	37
3.5Methodology overview	38
3.5.1 Sample Collection and Preparation	38
3.5.2 Preprocessing of the data	39
3.5.3 Data Processing	40
Chapter 4:Field and Laboratory Studies	43
4.1 Area selection and definition of analytical objectives for field and lab studies	43
4.2 Field studies and sample collection	44
4.3 Petrographic Study of the Samples	51
4.4 Field Spectra collection	63
4.4.1 Instrument	63
4.4.2 Instrument calibration	64
4.4.3 Creation of ASD spectral library	64
Chapter 5: Preprocessing of Data	67
5.1 Atmospheric Correction	68
5.1.1 Background and Methods	68
5. 2 Atmospheric correction of ASTER L1B data	70
5.2.1 Atmospheric correction of ASTER VNIR-SWIR data and reflectance retrieval	71
5.2.2 Methods of relative atmospheric correction	71

5.2.3 Methods of absolute atmospheric correction	74
5.3 Atmospheric correction of ASTER TIR data	80
5.4 Discussion on atmospheric correction results	82
Chapter 6: Data Processing	84
6.1 DPCA processing of LANDSAT and ASTER data	85
6.1.1 Albite	89
6.1.2 Epidote	90
6.1.3 Calcite	92
6.1.4 Chlorite	94
6.1.5 Kaolinite	96
6.2 Stereo Processing for DEM Generation	98
6.2.1 GCP Data Collection	99
6.2.2 Stereo restitution	100
6.2.3 DEM Data: Structural Analysis	101
6.3 Spectral Processing of ASTER Data	104
6.3.1 Band composites	104
6.3.2 Decorrelation stretch images	106
6.3.3 Band ratios, RBD images, and Ratio Composites	107
6.3.4 Spectral Similarity Analysis	113
6.3.4.1 Spectral Angle Mapper	114
6.3.4.2 Mixture Tuned matched Filtering	117
6.3.4.3 Spectral Feature Fitting	120
6.3.5 Spectral Similarity Analysis for TIR ASTER data	122
Chapter 7: Synthesis of Results and Interpretation	127
7.1 Data preprocessing: Correction of atmospheric effects	127
7.2 Satellite data processing for alteration mapping	129
7.3 Spectral Processing of ASTER data	130
7.3.1 Accuracy Assesement for Classification	131

7.3.2 Identification of Albitite Zone	134
7.4 Synthesis of results and interpretation	148
7.5 Summary of Conclusions	151

List of Figures

Figure no.	Caption	Page No.
Fig. 1.1	Interdependency of the chapters in the thesis	10
Fig. 2.1	Location map of the study area	21
Fig. 2.2	a) Geological map of northern part of main Delhi basin	25
	b) Geological Map of the study area	26
Fig. 2.3	Lineaments marked on ASTER image	27
Fig. 3.1	Base Map of the Study Area	34
Fig. 3.2	Drainage Map of the Study Area	35
Fig. 3.3	Contour Map of the Study Area	36
Fig. 3.4	Procedural flowchart of the methodology	38
Fig. 4.1	Field Locations at Kushwali Dhani Near Mavanda Tarla	46
Fig. 4.2	Field Locations Near Mevara Jatuwas	47
Fig. 4.3	Field Locations Near Mevara Gurjawas and Mevara Jatuwas	47
Fig. 4.4	Sample 1 a) Hand Specimen b) Thin Section 4xp c) Thin Section 4xc	51
Fig. 4.5	Sample 2 a) Hand Specimen b) Thin Section 4xp c) Thin Section 4xc	52
Fig. 4.6	Sample 3 a) Hand Specimen b) Thin Section 4xp c) Thin Section 4xc	53
Fig. 4.7	Sample 4 a) Hand Specimen b) Thin Section 4xp c) Thin Section 4xc	53
Fig. 4.8	Sample 7 a) Hand Specimen b) Thin Section 4xp c) Thin Section 4xc	54
Fig. 4.9	Sample 8 a) Hand Specimen b) Thin Section 4xp c) Thin Section 4xc	55
Fig. 4.10	Sample 9 a) Hand Specimen b) Thin Section 4xp c) Thin Section 4xc	55
Fig. 4.11	Sample 11 a) Hand Specimen b) Thin Section 4xp c) Thin Section 4xc	56

Fig. 4.12	Sample 12 a) Hand Specimen b) Thin Section 4xp	56
Fig. 4.13	Sample 13 a) Hand Specimen b) Thin Section 4xp c) Thin Section 4xc	57
Fig. 4.14	Sample 14 a) Hand Specimen b) Thin Section 4xp c) Thin Section 4xc	58
Fig. 4.15	Sample 15 a) Hand Specimen b) Thin Section 4xp c) Thin Section 4xc	58
Fig. 4.16	Sample 16 a) Hand Specimen b) Thin Section 4xp	59
Fig. 4.17	Sample 17 a) Hand Specimen b) Thin Section 4xp	59
Fig. 4.18	Sample 18 & 19 a) Hand Specimen b) Thin Section 4xp c) Thin Section 4xc	60
Fig. 4.19	Sample 20 a) Hand Specimen b) Thin Section 4xp	60
Fig. 4.20	Sample 21 a) Hand Specimen b) Thin Section 4xp c) Thin Section 4xc	61
Fig. 4.21	Sample 22 a) Hand Specimen b) Thin Section 4xp c) Thin Section 4xc	62
Fig. 4.22	Sample 23 a) Hand Specimen b) Thin Section 4xp c) Thin Section 4xc	62
Fig. 4.23 a & b	Lab Spectra from ASD FieldSpec®-Pro spectroradiometer	65
Fig. 4.24 a & b	Resampled Lab Spectra according to ASTER data	66
Fig. 5.1	Schematic representation of crosstalk in ASTER SWIR	70
Fig. 5.2	Log Residual Correction a) Corrected image b) Image spectra Vs Reference spectra	72
Fig. 5.3	IARR Correction a) Corrected image b) Image spectra Vs Reference spectra	73
Fig. 5.4	Modified Flat Field Correction a) Corrected image b) Image spectra Vs Reference spectra	74
Fig. 5.5	FLAASH Correction a) Corrected image b) Image spectra Vs	79

	Reference spectra	
Fig. 5.6	ATCOR Correction a) Corrected image b) Image spectra Vs Reference spectra	80
Fig. 5.7	Thermal Atmospheric Correction a) Corrected image b) Corrected Spectra for Albitite	81
Fig. 6.1	Methodology for Crosta Processing	87
Fig. 6.2	Aster and Landsat 7 spectral bands in electromagnetic spectrum	88
Fig. 6.3	Laboratory spectra of muscovite, kaolinite, alunite,epidote, calcite and chlorite resampled to ASTER band passes.	88
Fig. 6.4	Spectral Reflectance Curve for Albite	89
Fig. 6.5	Albite rich areas a) PC 3 of Aster data b) PC 1 of Landsat data	90
Fig. 6.6	Spectral Reflectance Curve for Epidote	91
Fig. 6.7	Epidote rich areas a) PC 3 of Aster data b) PC 1 of Landsat data	92
Fig. 6.8	Spectral Reflectance Curve for Calcite	93
Fig. 6.9	Calcite rich areas a) PC 1 of Aster data b) PC 1 of Landsat data	94
Fig. 6.10	Spectral Reflectance Curve for Chlorite	95
Fig. 6.11	Chlorite rich areas a) PC 1 of Aster data b) PC 1 of Landsat data	96
Fig. 6.12	Spectral Reflectance Curve for Kaolinite	96
Fig. 6.13	Kaolinite rich areas a) PC 1 of Aster data b) PC 1 of Landsat data	97
Fig. 6.14	Methodology adopted for DSM generation	98
Fig. 6.15	Leica GPS 500 system	99
Fig. 6.16	GCP Collection in the field	99
Fig. 6.17	GCP distributions in area	100
Fig. 6.18	DSM of the study area	101

Fig. 6.19(a)	Lineaments in the study area interpreted from Cartosat DSM	102
Fig. 6.19(b)	Lineaments extracted from Cartosat -1 DSM overlayed on ASTER image	103
Fig. 6.20	False Color Composites with maximum variance. a) 4-6-8 (for SWIR data alone) b) 6-3-1 (for VNIR-SW1R combined data)	105
Fig. 6.21	Decorrelation Stretch Image. a) 4-6-8 b) 5-7-9	107
Fig. 6.22	Aster Spectral Indices a) Ferric, b) Ferrous, c) amphibole, d) epidote/chlorite, e) Mg-OH, f) alunite/kaolinite/pyrophyllite	110
Fig. 6.23	Colour Ratio Composite of band ratios (red: 5/6, green: 7/6 and blue: 7/5) for phengitic, sericitic and kaolinitic alteration in the study area. The minerals typical of phyllic and argillic alteration are concentrated along the NE-SW trending shear zone, on both sides of the albitite zone	111
Fig. 6.24	Color Ratio Composite of band ratios (red: $5*7/6^2$, green: 6/8 and blue: 4/5) for clay, amphibole and laterite alteration in the study area. Clay is mapped in red colour, amphibole in green and laterite in blue colour. Clay minerals and amphibole are concentrated along the reported shear zone. Laterite is seen adjoining the clay minerals A laterite patch is also seen in the SE part of the image	112
Fig. 6.25	Color Ratio Composite of band ratios a) General Lithological Mapping red: 4/1, green: 3/1, blue: 12/14 b) Gossan Alteration red: 4/2, green: 4/5, blue: 5/6.	113
Fig. 6.26	Spectral Angle Mapping concept. (a) For a given feature type, the vector corresponding to its spectrum will lie along a line passing through the origin, with the magnitude of the vector being smaller (A) or larger (B) under lower or higher illumination, respectively. (b) When comparing the vector for an unknown feature type (C) to a known material with laboratorymeasured spectral vector (D), the two features	115

	match if the angle ‘a’ is smaller than a specified tolerance value.	
Fig. 6.27	Albitite classified area- SAM classification	117
Fig. 6.28	Diagram Showing Mixture Tuned Matched Filtering Technique	118
Fig. 6.29	Albitite classified area- MTMF classification	119
Fig. 6.30	RMS and Scale images for Albitite	121
Fig. 6.31	Albitite classified area (VNIR-SWIR ASTER) - SFF classification	122
Fig. 6.32	Albite spectra in ASTER bands	
Fig. 6.33	Albitite classified area (TIR ASTER) - SAM classification	124
Fig. 6.34	Albitite classified area (TIR ASTER) - MTMF classification	125
Fig. 6.35	Albitite classified area (TIR ASTER) - SFF classification	126
Fig. 7.1	Reported Albitite Occurances and Sample Sites	132
Fig. 7.2	Abundance Map of SAM Classified Data a) Full Map b) Zoomed view with abundance range.	135
Fig. 7.3	Abundance values wrt longitudinal Coordinate for SAM classified image	137
Fig. 7.4	Albitite Zone classified using SAM Algorithm	140
Fig. 7.5	Abundance values wrt X Coordinate for SFF classified image	142
Fig. 7.6	Albitite Zone classified using SFF Algorithm	144
Fig. 7.7	Abundance values wrt X Coordinate for MTMF classified image	146
Fig. 7.8	Albitite Zone classified using MTMF Algorithm	148
Fig. 7.9	Locations outside the albitite zone exhibiting high spectral similarity to albitite	150

List of Tables

Table no.	Caption	Page no.
Table 2.1	Stratigraphic sequence of Aravalli Supergroup	24
Table 3.1	ASTER Specifications	30
Table 3.2	ASTER Band Specifications **(www.infoterra-global.com)**	30
Table 3.3	Landsat ETM Data Specifications	31
Table 3.4	Cartosat Data Specifications	32
Table 3.5	Ancillary Data used in the Study	33
Table 4.1	Description of Field Measurement Locations	44-46
Table 4.2	Analytical Spectral Device FieldSpec-FR specifications (source: FieldSpec® Pro User Guide)	63
Table 5.1	Column water vapor amounts and surface temperatures for the MODTRAN model atmospheres (Source: FLAASH user guide)	75
Table 5.2	ENVI FLAASH input parameters for the ASTER scene used	77
Table5.3	Acquisition parameters for the ASTER LIB dataset used	78
Table 5.4	Solar exo-atmospheric irradiance values for the nine reflective bands of ASTER (VNIR+SWIR)	78
Table 5.5	Haze value computation for ASTER VNIR+SWIR bands using the image-based DOS technique (COST meod Chavez, 1996) under moderate scattering atmospheric condition (Chavez, 1989)	78
Table 6.1	Loading of bands on principal components for albite a) Aster b) ETM+	89
Table 6.2	Loading of bands on principal components for epidote a) Aster b) ETM+	91
Table6.3	Loading of bands on principal components for calcite a) Aster b) ETM+	93

Table6.4	Loading of bands on principal components for chlorite a) Aster b) ETM+	95
Table6.5	Loading of bands on principal components for kaolinite a) Aster b) ETM+	97
Table6.6	a) Aster Band Ratios for Mineral Identification	109
	b) Common ratio & band combinations for Aster	110
Table7.1	Area Statistics for Albitite with ASTER data	131
Table7.2	Accuracy Assesement of ASTER classified products	133
Table 7.3	Albitite Abundance Range	134

CHAPTER 1

INTRODUCTION

1.1 GENERAL BACKGROUND

Albitite is a coarse grained, deep pink to brick red colour porphyritic rock which has randomly oriented subhedral laths of feldspar as the principal mineral. Albitite occurrences are very rare even on global scale and only a few reported occurrences have been documented so far from India. The generation of albitite is attributed to the replacement of alkali feldspar and plagioclase of the original granite by pure albite. Almost all descriptions associate the deposits with zones of extensive tectonic activity. Belevtsev (1980) and Grechishnicov (1980) described albitites in the Kirovograd-Krivoi Rog district. They reported that in this area the albitites are located adjacent to deep-penetrating fault extending over 100 km at surface and are associated with a combination of pegmatite intrusion, cataclasis and mylonitisation. Belevtsev (1980) studied albitites in The Beaverlodge district. Here the albitites are hosted within a major fault zone, the St Louis Fault. Albitites at Lagoa Real are developed along shear zones (Lobato and Fyfe, 1990). Occurrence of albitite in Guyana is reported from two sub-parallel, east-west trending fault zones (Alexandre, 2009).

Potential sources of uranium are known to be hosted in albitites, albitised granitoids, and albitised metasedimentary rocks. Several such economically viable uranium deposits have been reported from Krivoy Rog and Zheltye Vody in Ukraine, Espinharas and Lagoa Real in Brazil, Pleutajokk and Arjeplog in Sweden, Kitongo in North Cameroon (Barthel, 1987).

A few occurrences of albitite have been reported from a narrow linear zone in Khetri Copper Belt (KCB) in eastern Rajasthan, India. The detailed field survey in KCB has located albitite bodies distributed in a narrow zone of 170 km length. This zone is designated as ‘albitite zone’ of northern Rajasthan. The different albitite bodies occur in three linear sectors viz., the Sakhun Ladera, Khandela-Guhala and Maonda-Sior sectors.

The KCB forms the northern boundary of the Aravalli mountain range in Rajasthan, northwest India. It extends from Singhana in the NE to Raghunathgarh in the SW and is about 80 km long. The Kantli fault which strikes NW-SE divides the belt into two parts - viz., North KCB (NKCB) and South KCB (SKCB) (Das Gupta, 1968; Gupta *et al.*, 1998). The geological interest in the area is mainly because of the copper mineralization. KCB is a well studied, thoroughly documented, regionally metamorphosed mineralized belt, and is among the main indigenous sources of base metals (Cu, Co, Pb, Zn and related metals) in the country. The geological investigation in the area were mainly focused on description of the regional geology and the nature of mineralization in the area. Hacket (1877, 1880, and 1881) and Heron (1923, 1925) carried out detailed survey and documented the regional geology. The studies were also focused on exploring the potential of copper (Cu) mineralization and also to locate other economically viable Cu deposits in the area. Varma and Krishnanni (1963) analysed the mineralization in selected pockets of the study area. Further studies on ore mineralization were also carried out by Roy Chowdhury and Venkatesh (1971). The geological history of the area has been researched and discussed by various geoscientists. Researches indicate that the geological evolution of the area has been inferred by multistage development and sinking of intracratonic basin, deposition of different sedimentary facies and associated Cu mineralization. This was followed by events related to various deformational activities and multiphase metamorphism of the strata (Roy *et al.*, 1998). KCB is characterized by an unconformable basement-cover relationship between the high grade paragneiss-quartzite-calc-silicate rock sequence and copper hosted metasedimentary sequence. The metasedimentary rocks of the KCB display a NNE—SSW to NE—SW trend and are folded into a number of regional anticlines and synclines with culminations and depressions (Das Gupta, 1968).

The compressional tectonic activity resulted in structural deformation and multilevel folding, faulting and fracturing. Two main deformation stages affected the Proterozoic sequence probably at the end of Proterozoic-I (as indicated by 1700 Ma syn-second deformation Gothro Granite). The earlier deformation produced folds with axes plunging towards NW-SE to NNW-SSE direction. The associated gently dipping tangential shear zones indicate an overall shear in the NW to NNW direction, which, however, did not

induce appreciable tectonic stacking of lithologic successions. The later stage of deformation produced folds (macroscopic sinistral fold near Khetri-Rajota) and crenulation cleavage generally striking NNE-SSW. The axis of later folds plunges gently towards South (as towards North of Kalota) with occasional plunge reversal (Roy Chowdhury and Das Gupta, 1965). Large dextral shear zones, such as the NE- SW Singhana-Jaspura shear zone and the Babai-Taonda shear zone (running diagonally across the study area) are responsible for the arcuate shape of the Proterozoic sequence. Prograde metamorphism associated with earlier deformation is characterized by a pressure decrease and is followed by a temperature increase, linked to granitic emplacement during later deformation. Late tectonic stages are characterized by brittle deformation and the development of regional NE-SW striking fault zones as well as localized NW-SE trending transverse faults. Within the Proterozoic sequence, stratabound copper deposits with a cumulative strike length of 16 km, show broad stratigraphic control by Fe-Mg rich and carbonate bearing metasedirnents, which correspond to the transition zone between near shore detrital facies and deeper argillaceous marine sediments (Das Gupta, 1968).

Apart from copper mineralization, there is another geologic feature of great interest. This feature is a long narrow zone following a major crustal fracture. Along this zone presence of some pegmatite and adventurine (Fe rich) albitite has been reported by Ray (1987). Geomorphological evidences in the area suggest that this zone is younger than Kantli fault. The circumstantial evidences indicate that the compressional tectonic activity was followed by an extensional regime which resulted in a narrow linear zone which facilitated movement of fluids and subsequent hydrothermal activity resulting in mineralization differing from the previous Cu mineralization in the area.

Hydrothermal alteration of the country rock has led to intense lithological and geochemical heterogeneity in the area. Some of the hydrothermal alteration assemblages are characteristic of certain types of mineral deposits. In KCB area albitites are associated with uranium mineralization. In 1994, Atomic Mineral Department, Government of India, started ground based reconnaissance surveys to locate albitite-hosted uranium mineralization in Khetri, Rajasthan. They have demarcated various patches of uranium mineralization at different locations in the albitite line.

Presence of several uranium and other atomic mineral occurrences have been reported in ore samples from various parts of Rajasthan and Haryana in studies carried out in the albitite zone of western India (Singh *et al*., 1998). Atomic Minerals Directorate (AMD) for Exploration and Research has located about 200 radioactivity anomalies within and near the albitite zone in western India. The field surveyed data indicates that uranium, multiple oxide (containing Nb, Ta, and Ti), thorium, yttrium in this area are hosted in varied rock types, including basement rocks, albitised-metasedimentary, and associated sedimentary rocks of the Mesoproterozoic Delhi Supergroup.

The albitites in KCB are thought to be emplaced because of deep crustal fracture and associated cogenetic ultramafic bodies. A close genetic relationship between alkali metasomatism and uranium mineralization has been revealed through petrographic and lithogeochemical studies. The metasomatising fluid mobilized uranium and other large ion lithophile elements (LILE) and resulted in their mineralization along shear zones at a later stage.

Remote Sensing has proved its credibility in mapping geological and geomporphological features based on their regional morphology, pattern and relief. Geoscientists have been equipped with better techniques for discriminating and mapping surface mineralogy with the use of advanced optical remote sensing (Rowan *et al*., 2005). In addition remotely sensed stereo images are capable of providing high resolution digital elevation model (DEM). The structural and geomorphologic features are not easily identifiable in field investigations due to their scale or limitations due to inaccessible terrain. Three dimensional models of the terrain would enhance interpretational capabilities of geologists in extracting geomorphological and structural features. Three-dimensional visualization of the earth's surface and its investigation from varying view points and different orientations has proven to be particularly helpful in geological and geomorphological studies.

Wavelength range and the spectral resolution of the sensor dictates the discrimination potential of remotely sensed image data. Though remote sensors may have restricted capacity to capture data from the diagnostic subsurface horizon, they definitely provide extremely useful information from the surface to optimize fieldwork and mapping for geological applications. Since many of the minerals have diagnostic absorption features

in short wave infrared region (SWIR) because of the presence of OH and other hydroxyl bonds, thus this region of the electromagnetic spectrum is widely utilized for identification of mineralization. Thermal infrared (TIR) emissivity completes the spectral information about the minerals because of its greater sensitivity to quartz content than the VNIR (Visible and Near Infrared)-SWIR reflectance. Albite, the principle mineral of albitite displays small absorption features at wavelengths of 1.42 μm, 2.2 μm in the VNIR-SWIR region of the EMS. These absorption dips are feeble and are not characterstic dips for the identification of the mineral. In thermal region the mineral exhibits a characterstic absorption dip at 8.5 μm, thus it seems logical to utilize the entire spectrum starting from VNIR-SWIR to TIR for enhanced albitite mapping. Since thermal information is available with Landsat and ASTER data, hence theses two datasets were utilized for the study. For deriving high resolution topographic information, cartosat-1 stereo data is utilized. The research is carried out with a hypothesis that an integrated approach utilizing these sensor data could be helpful in identifying albitite in the study area.

Conventional multispectral scanning systems, such as Landsat TM and SPOT XS have the capability of recording up to 10 spectral bands with broad bandwidths of the order of 0.10 μm (Gens, 2010). Hyperspectral scanners are a special type of multispectral scanner that records a large number of bands with bandwidths in the order of 0.01 μm (Sabins, 1999). Hyperspectral imagers typically collect data in numerous (sometimes several hundred) contiguous narrow bands spanning a vast region of the electromagnetic spectrum. One of the first operational applications of hyperspectral remotely sensed earth observation was done in the 1980's in the field of mineral exploration. Experiments in the last 30 years indicate that hyperspectral remote sensing can significantly contribute to geological investigations, mainly in the identification and mapping of minerals. The identification is most suited for arid (non-vegetated) and semi arid areas since these instruments, owing to their narrow spectral bands are able to better resolve absorption features unique to specific mineral species, in contrast to broad-band multi-spectral scanners.

Hyperspectral data analysis involves comparing the reflectance spectra of every pixel with the reference spectra of known materials using some suitable logic (Thangavelu *et*

al., 2011). The Advanced Spaceborne Thermal Emission and Reflection Radiometer (ASTER) is designed largely to cater the needs of geologic mapping (Vani and Sanjeevi, 2002). ASTER was the first satellite with multiple bands covering the wavelength regions ranging from VNIR to SWIR and TIR. The four VNIR bands provided suitable information about iron ores and rare earth minerals (Rowan and Mars, 2003). The six SWIR bands helped in identification of molecular vibration absorption features which are diagnostic of carbonates and clays (Hook, 1990; Kruse and Broadman, 2000; Rowan and Mars, 2003). The TIR bands help in detecting changes in the position of SiO_2 restrahlen bands thereby are useful for distinguishing various silicates and also for determining feldspars as their characteristic absorption dips are located in TIR region.

The Landsat data has been used in a number of mineralogical studies and is therefore, believed to be one of the available resources for mineral mapping (Limpitlaw and Gens, 2006). ASTER can be useful in predicting mineral suites although its bandwidth might not be capable of differentiating subtle spectral features. Processing of ASTER and Landsat ETM+ data has shown very good correlation in the previous studies. Thus, in this study it is proposed to utilize the capabilities of both Landsat ETM+ and ASTER data along with field verification for identification of specific mineral, i.e. albite in the study area. The use of digitally enhanced Landsat and ASTER data has proven to provide profound results when interactively used along with the field information. The Cartosat -1 stereo images provide one of the finest resolution DEM's which have proven useful in interpreting topographical and geomorphological features. The present research has been carried out with an aim to demarcate the albitite zone which can be an input for locating potential areas of uranium mineralization in and around Khetri. The study utilizes the spectral and spatial capabilities of remote sensing technology to achieve the objective. The coarse resolution Landsat data is used primarily for the regional understanding of the geological and geomorphological set up of the area, and the ASTER data with medium spatial resolution and higher spectral resolution for identifying albitite in the area. The Cartosat -1 derived DEM is utilized for demarcation of linear features and to analyze the structural control on the mineralization. The present thesis has two major components- the remote sensing technology and the geological problem of the area which have been dealt in detail in the following sections.

1.2 MOTIVATION

KCB is a geologically dynamic and important area and detailed geologic database exists for the region. The interest in the area is mainly because of viable copper mineralization. Mining activity in the area has started in late 1960's and since then Geological Survey of India has published geological maps of the area on various scales. Though geological surveys were carried out many times in the area, still albitite zone has been noticed in much later days. Ray (1987) was among one of the first authors to report several distributed occurrences of albitite in NNE-SSW trending 20 km long zone. Later on several other albitite bodies were found from a 170 km long narrow zone. This zone was termed as the "albitite zone" or "albitite line". These studies were mainly based on a field intensive mode for locating and identifying albitite in the study area, thus the albitite zone was not looked at and demarcated in totality. The albitite zone also known as 'Albitite line' was initially known to extend over 170 km length (Ray, 1987, 1990). However the zone has now been traced over 320 km length in a NNE-SSW trending linear zone (Singh *et al.*, 1998). The albitite zone follows major lineaments and extends from Tal in the SW (Rajasthan) to Dancholi-Mewara in the NE (Haryana). In the southern part, the zone is microcline-rich thus termed as microclinite, whereas, towards the north, owing to its albite rich nature it is called as albitite.

The demarcation of albitite zone is of great geologic interest as association of albitite has been reported with mineralization, especially uranium mineralization. Since such an exercise cannot be adequately and reliably conducted purely through field surveys, the capabilities of high spectral resolution remote sensing data can be utilized to fill the gap which allows a synoptic view of the area for large spatial extent. To fulfill this objective and to establish a framework within which similar studies can be conducted for other parts of the country, an exhaustive analysis of ASTER data for a mineralized region in KCB has been conducted and reported in this thesis.

The research presents a detailed account of the analysis of multisensor satellite dataset for albitite mapping in the north KCB. This research is to contribute to delineation and demarcation of albitite zone which will assist in determining the potential for the mineralization in the area. A remote sensing approach of utilizing ASTER and Landsat

data integrated with Cartosat -1 stereo data derived elevation information offers the capability to resolve the key geological features of this area.

1.3 OBJECTIVES

The overall objective of the research is to analyze the capabilities of multisensor remote sensing datasets for mapping albitite zone in a part of the KCB in northwest India.

The study is based in the VNIR-SWIR and TIR region of the spectrum. Laboratory spectra acquired from field and image along with the petrographic analysis of hand specimens serve as guide in selecting image endmembers used as input for classification for mineral mapping. In addition to this, Cartosat -1 stereo image derived elevation data is used to map structures (lineaments) in the area which is later integrated with ASTER data to understand the impact of structure on spatial distribution of the albitite zone.

The approach adopted here has allowed for an evaluation of the potential of multisensor remote sensing data as a supporting and indirect evidential tool for known mineral anomalies in a well studied mineralized region. Results of remote sensing based mapping for the study area can, therefore, be directly compared with the field observations and geologic maps, and thus the study can serve as a test case to explore the potential of the technology for other areas. Briefly, the study has been designed to fulfill the following research objectives:

The main objective of the research is to *identify and map albitite rich zones in the Khetri KCB*. Further sub-objectives of the study are:

1. To analyse the capabilities of multispectral and hyperspectral satellite datasets for mapping albitite zones.
2. To investigate correlation between structural pattern and mapped albitite zone.
3. To evaluate various techniques of classification for mineral mapping.

1.4 SCIENTIFIC IMPACT

An understanding of spatial extent of albitite zone is of great value because it provides insight into potential mineralized areas. The goal of this research is to show the extent to which Landsat ASTER and Cartosat -1 remotely sensed data can be used to identify

albitite. For the present study, the investigations have provided a better understanding of the distribution of specific mineral, i.e. albite which can be linked to existing and potential uranium mineralized areas, and can thus serve as an exploration aid. In nutshell, the main scientific contributions of this research are outlined as follows:

- Detailed report of multisensor data analysis for albitite identification.
- Integration of Crosta technique for alteration mapping.
- Creation of a spectral library based on representative samples.
- Evaluation of various classification techniques for albitite mapping.
- Establishing remotely sensed data as a potential tool for albitite mapping.
- Delineation of albitite zone.

1.5 ORGANIZATION OF THE THESIS

This research has investigated the potential and capability of multisensory remote sensing data in albitite mapping with a case study in the KCB, in northwest India. Exhaustive analysis of ASTER data has involved investigation of data preprocessing and processing methods currently in vogue. The Landsat ETM+ and ASTER VNIR-SWIR and TIR data have been treated separately owing to the basic nature of the data. Photogrammetric processing of Cartosat -1 stereo data is done to generate DEM of the area. A ground truth database has been created to validate and interpret the findings of ASTER data analysis.

The thesis has been organized in 7 chapters on the basis of the treatment of the following components:

- Background literature review pertaining to the geology of the study area and remote sensing applications in lithologic and alteration mapping with focus on the use of ASTER data (Chapter 2).
- Discussion of the brief methodology and data employed (Chapter 3).
- Ground truth database development, in terms of field visits and laboratory investigations (petrographic and spectral) of selected field samples (Chapter 4).
- Preprocessing of ASTER VNIR-SWIR and TIR data for removal of radiometric, atmospheric and topographic effects and retrieval of the basic surface physical data (reflectance) using existing approaches (Chapter 5).

- Croasta processing of the Landsat and ASTER data for mineral mapping. Photogrammetric processing of Cartosat -1 stereo data. Analysis of ASTER VNIR-SWIR and TIR reflectance data for albitite mapping (Chapter 6).
- Synthesis of ASTER data analysis results with ground truth and validation of the results (Chapter 7).

The chapter interdependencies have been shown in Fig 1.1

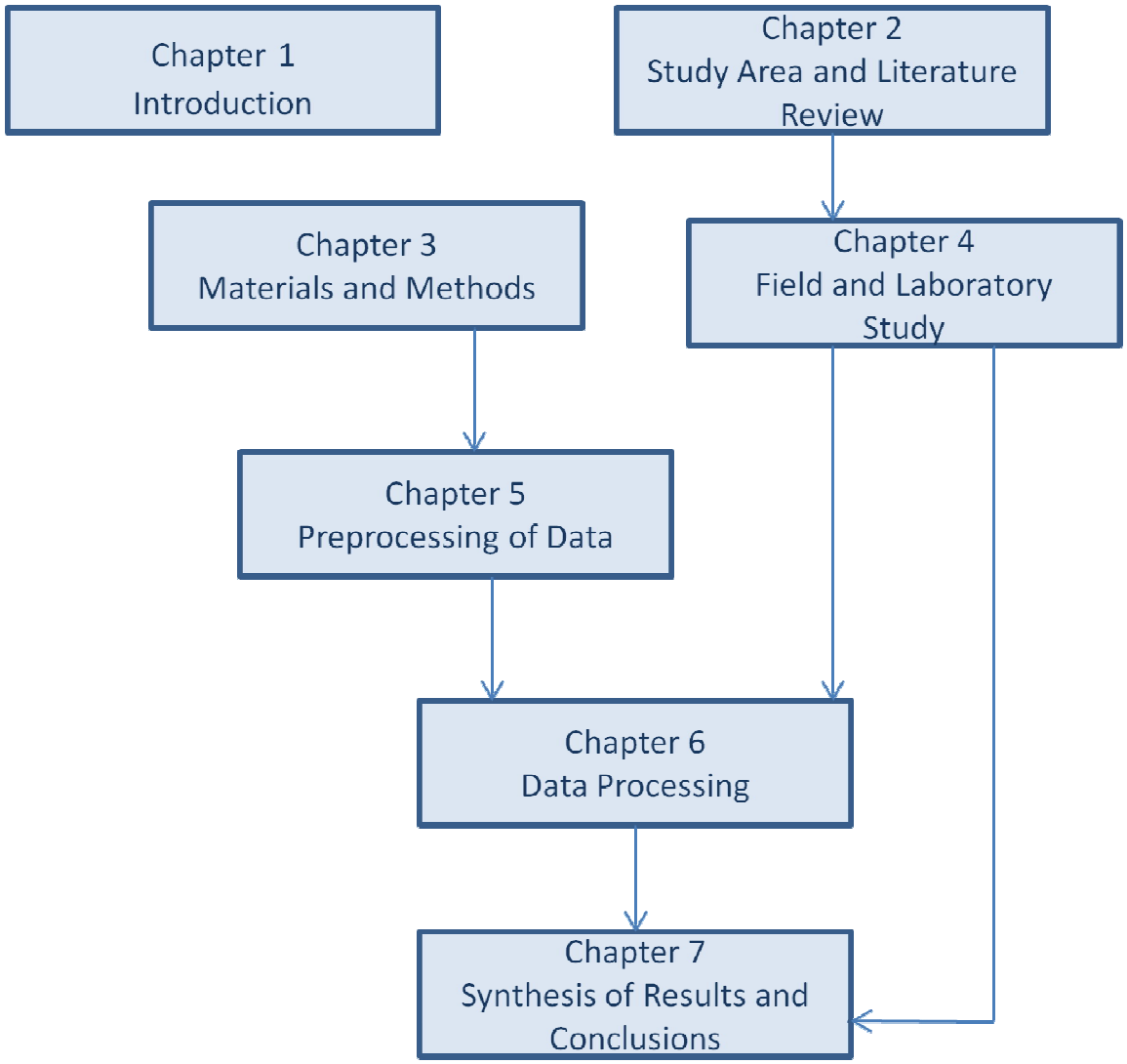

Fig 1.1: Interdependency of the chapters in the thesis

CHAPTER 2

LITERATURE REVIEW AND STUDY AREA

This research can be broadly said to have two major components. The area being of significant geologic interest because of evidences of significant zone of tectonic activity in form of dispersed albitite bodies and pegmatite veins in the host rock, the identification of a regional extent affected by albitite emplacement becomes quite significant. The area in which albitite emplacement has taken place can be used as an input for locating potential area of uranium mineralization. Thus the basic geological problem in the area is to locate the extent of the albitite zone. To cater to the present geological problem, the spectral and synoptic capabilities of remote sensing technology have been utilized. Hence keeping in view, the basic nature of the study, the literature review has also been grouped into different sections. This chapter gives a detailed review of the research related to geology of KCB in general and albitite zone in particular. It also reviews the use of spaceborne data emphasizes its utility for geological applications especially mineral identification.

2.1 LITERATURE REVIEW OF THE STUDY AREA

The KCB has attracted attention of many geologists since early days. This is mainly because of the area being rich in different ore minerals. Geology of the area, its stratigraphic sequence, nature of deformation, magmatism, metamorphism and ore mineralization in Delhi supergroup of rocks exposed in KCB have been studied by many researchers.

Hacket (1877, 1880, and 1881) was the first geologist who studied the regional geology of the area. His work in this area was subsequently modified by Heron (1923, 1925) to who goes the credit of most extensive study of the regional geology. He stressed the potentiality of the Khetri copper deposits. Deb (1948), Varma and Patni (1962) and Varma and Krishnanunni (1963) were among the first authors to carry out studies on geology and mineralization of different pockets in the Khetri area. Das Gupta (1962) did a detailed pertographic study on paragenesis of scapolite bearing amphibolites in KCB. Das Gupta (1968) studied the structural history of the KCB in Jhunjunu and Sikar districts, Rajasthan. Chandra Chowdhury *et al.* (1971) described the geology and ore

mineralization in Akwali section of KCB. Roy Chowdhury and Venkatesh (1971) have discussed the regional controls of ore localization in the belt. Wall-rock alterations in the Khetri have been discussed by Das Gupta (1962, 1964a), Das Gupta *et al.* (1963, 1965) and Sikka *et al.* (1966). Genetic aspects of the ores of Madhan-Kudan and Kolihan in particular and KCB in general have been discussed by Varma and Krishnanunn (1963), Das Gupta (1964a, 1964b) and Mukharjee (1969). Basu and Narsaya (1982) described widespread alkali metamorphism of Delhi supergroup of rocks in north eastern Rajasthan. Basu and Narsaya (1983) introduced an interesting petrological event represented by probable zone of carbonatite and fenitic rock association in the eastern part of KCB. They also reported alkali metasomatism in this area. Gupta *et al.* (1998) studied the basement cover relationship in the Khetri copper belt. They also gave a model for the emplacement mechanism of granite massifs in the study area. The geology, stratigraphy and structure of North Delhi basin was discussed by Chakrabarti and Gupta (1992).

One of the most interesting geological feature of this area, the albitite zone was not discussed till recent past. Ray (1987) reported the albitite occurrences and associated ore minerals in KCB. He discussed the regional extent and also the age of albitite emplacement. He studied albitite occurrences and ore mineral association in KCB and concluded that the uraninite and the Fe, molybdenum (Mo), and Cu-sulphide mineralization in the area is connected with a magmatic event and the associated cogenetic ultramafic rocks. The zone of this soda rich magmatic and metasomatic activity occurs as a NE-SW trending linear zone. Moreover the nature extent and tectonic significance of this magmatic/metasomatic event in a regional scale was discussed by him.

Ray and Ghosh (1989) also reported albitite dike in Dudu sector, Jaipur and discussed its tectonic significance. The total extent of albitite line divided into three sectors: Sakhun, Khandela-Guhala and Maonda, Babai, Sior was discussed by Ray (1990). Petrography and geochemistry of albitites in Banjaron Ki Dhani was discussed in detail by Jain *et al.* (1999). He observed that strong albitisation has taken place only along NE-SW, NW-SE and EW trending weak structural planes. The albitite line coincides with Kaliguman lineament in South Delhi fold belt. They also reported surface exposures of albitite in

Pachlangi, Karoth Dhanian, Maonda and Sagdu Ki Dhani. They concluded that the albitites of this area were not of magmatic origin. Albitised quartzites, albitised quartz biotite schists and albitised pegmatoids have been formed by the partial Na metasomatism of quartzites, quartz biotite schists and pegmatoids respectively. They also concluded that U-Th mineralization was not synchronous with Na metasomatism and occurred in a subsequent phase. Singh *et al.* (1998) analyzed the uranium and rare earth elements (REE) potential of the albitite-pyroxenite-microclinite belt of Rajasthan. Yadav *et al.* (2000) studied the geology and geochemistry of uraniferous albitites in Khetri area. Yadav *et al.* (2004) analyzed the tectono magmatic activation and its implication on metallogeny in Khetri sub basin. Yadav *et al.* (2008) proposed a descriptive model for albitite related uranium mineralisation of KCB. They observed evidences of hydrothermal alteration such as silification, chloritisation, haematisation and tourmalization. They also found evidences of two stages of cataclasis and albitization. It was summarized in their study that the albitization process was responsible for reducing the mechanical strength of the host rock. The ore bearing solution was alkali rich and acted as scavenger for uranium and other associated elements from metasediments.

Biju-Shekar *et al.* (2003) derived evidences from chemical ages of zircon and discussed the implications of the late paleoproterozoic magmatism in Delhi fold belt. Kaur *et al.* (2006) did an electron probe microanalyser study on Khetri granitoids. They calculated the chemical ages of zircon in the Khetri granitoids. They reported widespread late paleoproterozoic extension related magmatism in the study area. Kaur *et al.* (2012) reported two stage extreme albitisation of A type granites from Khetri, Rajasthan. They reported that 'A' type metaluminous ferroan granites in the Khetri complex of Rajasthan, NW India, have been albitised to a large extent by two metasomatic fronts, an initial transformation of oligoclase to nearly pure albite and a subsequent replacement of microcline by albite, with sharp contacts between the microcline-bearing and microcline-free zones. They also suggested that the albitisation took place at ~350°–400°C. It was caused by the infiltration of an ascending hydrothermal fluid that had acquired high Na/K and Na/Ca ratios during migration through metamorphic rocks at even lower temperatures in the periphery of the plutons.

2.2 LITERATURE REVIEW OF GEOLOGIC REMOTE SENSING FOR MINERAL MAPPING

A wealth of scientific literature is available on the applications of remote sensing technology in geology, with special focus on mineral exploration activities. Most mineral deposit models include some common elements that are relevant for remote sensing: tectonic setting, lithological association, alteration and structural control (Sabine, 1999). Most of the studies using remote sensing as a tool for mineral identification have utilized the unique spectral signatures of specific minerals. The utility of a remote sensor in mineral identification activity relies largely on its coverage of the spectral regions where these spectral features lie.

In order to see how geologic remote sensing for mineral exploration has developed and improved since the successful launch of the first Landsat satellite in 1972, a comprehensive review of the relevant literature has been made. It may be mentioned that while active remote sensing has proven its merit in geologic applications in general and mineral exploration, it has been kept out of the preview of this review, since the focus of the present study is albitite mapping. The available scientific literature on remote sensing applications in mineral exploration and geology can be grouped into the following four categories:

1. Multispectral remote sensing in mineral identification
2. ASTER data for mineral mapping

2.2.1 Multispectral Remote Sensing for Mineral identification

Initial success in operational use of remote sensing for lithologic mapping was achieved using data from the Landsat MSS and TM (and ETM+) sensors (Abrams *et al.*, l983; Podwysocki *et al.*, 1983), and these sensors continue to be the most widely used multispectral remote sensors for geologic applications. Goetz *et al.* (1983) and Sabins (1999) have provided a general overview of the use and potential of multispectral passive remote sensing in mineral exploration activity, with emphasis on the application of Landsat TM data. Most studies that have utilized the Landsat data, have focused primarily in discriminating lithologies (Crósta and Moore, 1989; Qari, 1989; Kenea, 1997; Van der Meer *et al.*, 1997; Mickus and Johnson, 2001). The early studies on

Landsat data for mineral identification started with simple image processing functions. Band rationing, contrast stretching and color compositing for visual discrimination were applied on Landsat MSS data for south-central Nevada, USA by Rowan *et al.* (1977). This was done to discriminate hydrothermally altered rocks. Results showed good discrimination between hydrothermally altered and unaltered rocks except for shale and siltstone.

Abrams *et al.* (1983) used Landsat MSS and aircraft scanner data simulating Landsat 4 TM data for separation of lithologies, discrimination of hydrothermal alteration and structural mapping. Band rationing, principal component and canonical transformations techniques were performed to distinguish iron-oxide-rich areas. It was found that TM simulator data was more useful for alteration mapping.

In the area of Central East Greenland with an objective to identify iron oxide staining for exploration of Stockwork molybdenum and other base metals, spectral ratioing and factor analysis were performed on Landsat MSS image to generate color composites for digital classification of limonitic rust zones. By using this technique about 88 significant rust zones were identified in Tertiary igneous province and Precambrian metamorphic province (Conradsen and Harpoth, 1984). Rationing, principal component analysis and IHS decorrelation techniques were performed on Landsat TM image for Aquaba-Levant structure in Wadi Araba in Jordan for the Graben, hydrothermal mapping. Enhanced spectral discrimination of phyllosilicates and iron oxides through decorelation processing was resulted by using this technique (Kaufmann, 1988).

In Hamerslay province in Western Australia, Landsat TM data was used to discriminate and identify ferric oxides. Principal component analysis of band ratios was performed on the dataset and thus discrimination between hematites and goethite-rich areas was achieved (Fraser, 1991).

Object oriented principal component analysis (OOPCA), also called feature oriented principal component selection, or FPCS or Crosta technique, spectral decorrelation, and IHS transformation technique were performed on Landsat TM of Central Mexico. The techniques for spectral enhancement of hydrothermally altered rocks in a vegetated area were compared in the study. The results showed that the discrimination of

hydrothermally altered volcanic from the unaltered can be achieved through statistical decorrelation techniques (Rutz-Armenta and Prol-Ledesma, 1988).

In Guanajuato district of Mexico, hydrothermally altered rocks were identified by spectral enhancement of selected pixels. Band subtraction and principal component analysis technique were applied on Landsat TM image resulting in discrimination of hydrothermally altered rocks in heavily vegetated terrain and identification of new zones of argillic alteration (Torres-Vera and Prol-Ledesma, 2003).

Crosta technique was applied on Landsat ETM+ image for porphyry copper alteration mapping in Southern Iranian volcanic sedimentary belt. Iron-oxide and hydroxyl-bearing minerals were mapped by applying this technique (Ranjbar *et al.*, 2004).

2.2.2 ASTER data for Mineral mapping

It is evident that the best results of remote sensing for mineral identification can be obtained from spectral data that covers spectral regions of geologic interest, in large number of closely spaced bands. This typically corresponds to the hyperspectral remote sensing. Existing airborne hyperspectral remote sensing has limitations of geographic coverage, cost and data processing expertise which hinder the popular use of hyperspectral remote sensing for geologic mapping. A major development in bridging this gap was achieved with the launch of ASTER in December 1999 as it provided high quality, global data with unique spectral coverage in Visible and Near Infra Red-Short Wave Infra Red (VNIR-SWIR) atmospheric windows (Yamaguchi *et al.*, 1998). Although multispectral by all definitions, ASTER data has provided a first superior alternative to the Landsat Thermal Infra Red (TM) data widely used and understood by most geologic remote sensing specialists. In addition to the finer spectral coverage (5 bands) of the range covered by the single TM band 7 (2.08-2.35 μm) where absorption features of key alteration minerals lie, ASTER also provides best spectral coverage (5 bands) of the TIR atmospheric window relevant to lithologic mapping applications from a spaceborne platform. Hence, ASTER offers a unique advantage of complementary geologic information. ASTER multispectral data not only offer global coverage at affordable cost, but also flexibility in data processing as it can he processed using existing image processing technology designed to handle multispectral as well as

standard hyperspectral data. Therefore, in more than one sense, ASTER data bridges the gaps between existing multispectral and hyperspectral sensors, and can be called a hybrid system. Since launch, numerous studies have amply demonstrated the utility of ASTER data in geology, particularly in lithologic mapping and hydrothermal alteration mineral detection and mapping.

Previous research has shown that the SWIR spectral range covered by ASTER allows distinguishing pure components from mineral mixtures (Kruse *et al*., 1990; Crosta *et al*., 1998) although the width of the SWIR ASTER bands have their limitations with respect to differentiating subtle spectral features. The configuration of bands 5 and 7 of TM/ETM in the SWIR portion allows the recognition of hydrothermal alteration sites, but the coarse spectral resolution does not allow the discrimination of individual minerals (Gabr *et al*., 2010). The six spectral bands of the ASTER SWIR subsystem were designed to record and distinguish absorption features for Al-OH, Fe, Mg-OH, Si-OH and CO_3 (Abram and Hook, 1995; Fujisada, 1995). Thus, the ASTER SWIR reflective bands are capable to identify mineral assemblages that include: (1) mineralogy generated by the passage of low ph fluids (alunite and pyrophylite); (2) Al-Si-(OH) and Mg-Si-(OH)-bearing minerals including kaolinite, mica and chlorite groups; (3) Ca-Al-Si-(OH) bearing minerals including epidote group and also carbonate (calcite and dolomite) as a group (Huntington, 1996).

ASTER has been used extensively for lithologic mapping (Rowan and Mars, 2003; Gomez *et al.*, 2005; Qiu *et al.*, 2006; Khan *et al.*, 2007; Li *et al.*, 2007) There are many papers describing discrimination of granite (Watts and Harris, 2005; Massironi *et al.*, 2008), ophiolite (Qiu *et al.*, 2006; Khan *et al.*, 2007) and basement rocks (Vaughan *et al.*, 2005; Gad and Kusky, 2007; Qari *et al.*, 2008).

In Mountain Pass, California, USA, ASTER data was used for discriminating calcitic rocks from dolomitic rocks. L1B VNIR-SWIR bands were calibrated to surface reflectance. These calibrated VNIR-SWIR bands and L2 AST_05 TIR surface emissivity data was utilized for the study. The results showed that apart from discrimination of calcitic rocke from dolomitic rocks, Fe-muscovite can also be distinguished from Al-muscovite. Quartzose and carbonate rocks were also mapped using TIR data (Rowan and Mars, 2003).

Rowan *et al.* (2006) mapped alteration minerals such as opal, alunite, kaolinite, muscovite and calcite using ASTER L1B VNIR –SWIR surface reflectance in Cuprite, Nevada, USA. Crosta *et al.* (2003) mapped alunite, illite, kaolinite and smectite in Patagonia, Argentina using ASTER L1B VNIR-SWIR data.

Hubbard *et al.* (2003) mapped Ferric-iron mineral suites using ASTER VNIR data in Central Andes. They also discriminated clay-sulphate mineral using ASTER SWIR data. Ninimiya *et al.* (2005) found mafic-rich, quartz-rich and carbonate-rich rocks in Beishan Mountains, China and Mt. Fitton, Australia using ASTER L1B TIR image. ASTER L2 TIR surface emissivity data was used in Hiller Mts., Nevada, USA and Tres Virgenes-La Reforma, Baja California Sur, Mexico resulting in quantitative estimation of SiO_2 weight percent (Hook *et al*., 2005). Rowan *et al.* (2005) mapped four felsic and mafic lithologic classes using ASTER VNIR-SWIR data and two classes of mafic-ultramafic rocks and four classes of quartzose-intermediate rocks using ASTER TIR surface emissivity data in Mordor, NT, Australia.

Hydrothermal hydroxyl-bearing alteration minerals in a densely vegetated terrain were mapped by Galvao *et al.* (2005) in Central Brazil using ASTER L1B SWIR calibrated to surface reflectance data. Mars and Rowan, 2006 discriminated phyllically and argillacally altered rocks using ASTER VNIR-SWIR calibrated to surface reflectance data in Zagros magmatic arc in Iran. Carranza and Hale (2002) mapped minerals characterizing silicic, potassic and phyllic zones in Infiernillo porphyry deposit in Argentina using ASTER L1B normalized to relative reflectance data. In Reko Diq, Pakistan L1B VNIR-SWIR calibrated to surface reflectance and L2 AST_05 TIR surface emmisivity data was used to map silicic quartz-bearing, phyllic muscovite, argillic alunite and propylitic chlorite by hydrothermal alteration mapping (Rowan *et al*., 2006). Identification and mapping of advanced argillic, argillic and silicic zones of Cerro La Mina, Patagonia, Argentina using ASTER SWIR calibrated to surface reflectance was carried out by Ducart *et al.* (2006). Sodic, potassic and silicic-phyllic alteration minerals were distinguished using ASTER L1B VNIR-SWIR-TIR of Chadormalu paleocrator, Bafq region of Central Iran (Moghtaderi *et al*., 2007).

Zhang *et al.* (2007) distinguished and mapped alteration minerals such as alunite, kaolinite, muscovite and montmorillonite by using ASTER L1B VNIR-SWIR-TIR of

Chocolate Mts., California, USA. Pena and Abdelsalam (2006) demonstrated the potential of ASTER data to map sedimentary terrains. They utilized the ASTER data and several other satellite sensor datasets to map sedimentary terrain in Southern Tunisia. Many authors have explored the utility of ASTER data for mineral exploration. Vaughan *et al*. (2005) mapped geothermal minerals using ASTER data. Hydrothermal minerals were identified by Zhang *et al*. (2007); Hubbard *et al*. (2003); Yamaguchi and Natio (2003); Carranza *et al*. (2008); Mars and Rowan (2006 and 2010). Madani and Emam (2011) utilized ASTER dataset for distinguishing barite mineralization areas while evaporate systems were studied by Kavak (2005) and Oztan and Suzen (2011). Some work on ASTER data also focuses on generic lithologic mapping (Hasselwimmer *et al.*, 2011). ASTER data was also utilized for granitoids mapping in western Nepal (Bertoldi *et al*., 2011) to establish a relationship between lichens and granitoids bodies. This relationship was used to map granitoids in this area.

2.3 LITERATURE REVIEW OF CARTOSAT-1 STEREO PROCESSING AND DEM APPLICATIONS FOR GEOMORPHOLOGICAL MAPPING

Digital elevation model (DEM) was described by Bretar and Chehata (2010) as digital representation of the earth surface topography. Stereo images derived from satellite help in fast derivation of elevation information for the area. Cartosat-1 is a state-of-the-art remote sensing satellite built by ISRO which is mainly intended for cartographic applications and provides along track stereo images with a spatial resolution of 2.5m. Surface models derived from Cartosat-1 data have been analyzed for planimetric and vertical accuracy. James Lutes, 2006 analyzed multiple scenes across varying terrain conditions and reported planimetric accuracy of 2-4 m and vertical accuracy of 5-10 m. Kumar, A. 2006 observed that the error was significant (100 to 200m) when only RPC information for Cartosat –1 stereo data was used, whereas the error in height was reduced to 2 to 13 m after utilizing the GCP information. Agarwal *et al.* (2008) utilized elevation data for morphometric analysis of Pein river basin. They derived lineaments from the satellite derived surface model. Similar studies using satellite stereo data was carried out by Bali *et al.*, 2011 and 2009 in Himalayan region. Tripathi, 1988 exploited the directional nature of geological lineaments and used semiautomatic methods for

lineament extraction from the surface model. He applied directional filtering for lineament extraction. Sanjeevi and Bhaskar, 2008 exploited the morphological image processing for lineament extraction. Lineaments can be extracted and enhanced using this technique.

2.4. STUDY AREA

The study area lies in the eastern part of the north Khetri copper belt. It falls within the Survey of India toposheets 45M/9 and 45M/13, in the Jhunjhunu district of Rajasthan state. The geographic extents of the study area lies between 75° 43' E to 75° 50' E longitudes and 27° 53' N to 27° 59' N latitudes. Khetri, the most important and populous town in the area, is situated to the northwest of the study area. The location map of the study area is shown in Fig. 2.1.

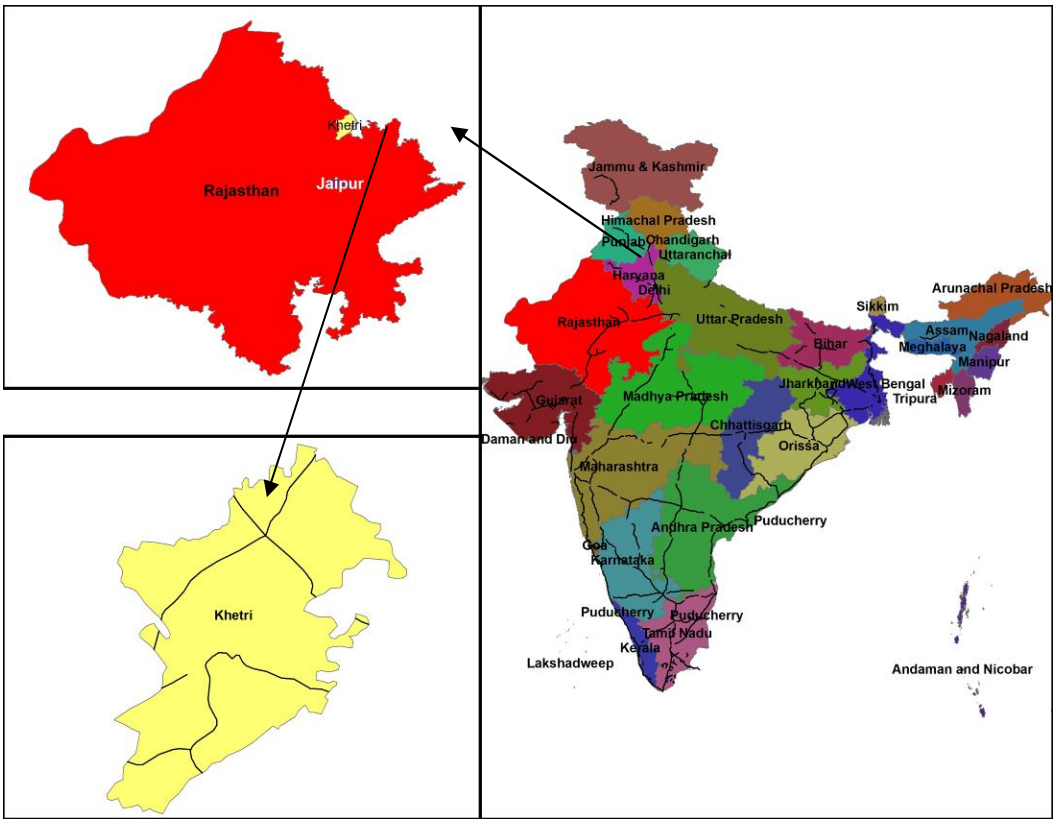

Fig. 2.1: Location map of the study area

The area is well connected to the major cities, like Delhi and Jaipur by metalled roads and railways. Large villages in the study area, like Babai, Mewara Gurjawas and Mavanda Tarla are well connected with the road network. Nearest railway station is at Chirawa, which is about 30 km from Khetri.

2.4.1 Physiography

Regionally, the area consists of slightly undulating terrain in the east and moderately high hilly ranges to the west of the main study area. The high ranges of the west belong to north and south Khetri copper belt. Beyond the hills of the west is the great Indian Thar Desert. Nearly NS trending hills of Madhogarh lie to the south-west of the area.

Quartzite ridges form the most prominent topographic features of the study area. The most prominent landforms in the area is the ridge about 3.5 km north of Papurna, with nearly uniform relief for a length of about 3 km. The ridge top with a relief of 800 m above mean sea level is made up of pure quartzites. In general the hills exhibit moderate dip to the west and steep dips to the east side. These hills represent the limbs of a regional fold called the Babai anticline. The lithology of the area is quite diverse, and exhibit different level of weathering in different areas. The quartzites which are the most resistant rocks cap major ridges in the area. Amphibolites and the calc-silicates and calcareous rocks are the other resistant rocks found in the area. The meta-pelites, feldspathic quartzites and felsic intrusives (granites, granodiorites and pegmatites) have yielded to the agents of weathering in most part. The main reason for this differential weathering is that the feldspar of the rocks is more susceptible to weathering in the hot and dry climate of the region than the carbonates.

There is no perennial drainage in the study area, though rivulets and nalas of varying magnitude dissect the hill flanks. The rivulets exhibit a dendritic pattern and are fairly dense. The major drainage follows the structural trends in the area. The Kantli river and the underlying fault lie to the southwest of the study area. Most of the westerly flowing drains disappear in the desert of the Thar, while some form feeders to the Kantli river flowing westwards. The agriculture is seasonal and highly monsoon dependent.

Climatologically the area represents a typical tropical semi-arid to arid climate. The temperature fluctuates between the far ends of the thermometer for summer and winter seasons, with mercury crossing the 45° Celsius mark in peak summers, and going below

04° Celsius in the winters. Rainfall is moderate to scanty, with an average precipitation of 25 to 30 cm annually.

The vegetation in the area is quite sparse and scanty. Xerophytes dominate the natural vegetation, which is also controlled by the bedrock regolith. The quartzites, carbonates and the intrusives (both felsic and mafic) in most part are barren and devoid of vegetation, while the schists and phyllites along with alluvium provide the best ground for vegetation in the area.

2.4.2 Geology

Major rock types in the area are the quartzite of Alwar group followed by Ajabgarh group. The Ajabgarh group mainly comprises of calc-silicate rock, quartz-biotite schist, impure marble, muscovite-quartz schist, calcareous quartz-biotite schist. Calc-silicate rocks with impure marble bands and amphibole-quartzite is one of the most dominant rock type in the study area (Roy *et al*., 1998). The rock units generally exhibit NNE-SSW trend with moderate to steep dips. Concordant and discordant pegmatite, quartz veins, calcite veins and albitites of various dimensions are also found. Granite is exposed along NE-SW trend at Dhancholi-Dhanota, Dabla, Bamanwas and Besrara. The country rocks at Sior-Mewara Gujarwas sector have been subjected to various igneous and metasomatic changes, thereby reconstituting the host-rock mineralogy. Here, multiple episodes of later feldspathic and granitic activities mostly along the regional trend have converted the host rock into granite-gneiss associated with granite bands (Fig. 2.2 a and b).

Albitisation of the country rocks is associated with varying degrees of other changes such as silicification, chloritisation and calcitisation. Rocks in Mukhauta-Jamalpur-Sior sector are invariably albitised in concordant and discordant directions (Roy *et al*., 1998). While the earlier generation follows the regional trend (NNE-SSW), later generation follows WNW-ESE to E-W trend. Associated development of amphibole, coarse euhedral magnetite and ilmenite are also seen. Epidotisation is another common feature. Albitisation is so intense at certain pockets such that the rock turns from albitised calc-silicate rock into albitite. Intense deformation and associated cataclasis has resulted in the formation of brecciated albite-hornblende-quartz rock comprising of angular pieces of albite, quartzite and calc-silicate rock intercepted by later hornblende-albite veins. Disseminated chalcopyrite, pyrite and magnetite are commonly associated.

Petrographically, at least two generations of albites are discernible, of which the first generation comprises of coarse crystalline albite, whereas the later is fine-grained and aventurine in nature. In most cases, the second generation albitite is associated with calcitisation. Sphene, minor amounts of wollastonite, apatite, zircon, xenotime and monazite are found to be associated with albitisation. The stratigraphical sequence of various lithounits of the KCB by different workers has been summarized below (Table 2.1):

Table 2.1: Stratigraphic sequence of Aravalli Supergroup

Heron (1953)	Gupta *et. al*. (1997)	Sinha- Roy *et. al*.(1998)	Roy and Jakhar (2002)
Granite , basic and ultrabasic rocks Impure limestone, quartzite, phylite, biotite schist and composite gnesis Aravalli system Quartzite, grit, conglomerate & soda syenite Local amygdaloids and tuffs ------Unconformity---- Banded gneissic complex	ARAVALLI SUPERGROUP (2000-2500 MA) Champaner Group Lunavada Group Granites, Rikhabdev ultramafic suite Jharol/Dovda/Nathdwara Groups Barilake/ Kankroli Groups Udaipur Group Debari Group ---Unconformity--- Bhilwara Supergroup	ARAVALLI SUPERGROUP Darwal Granite Jharol Group (Including Rikhabdev ultramafics) Unconformity Leucogranite Debari Group (including Jahazpur, Pur- Banera, Rajpura-Dariba etc. belts) Delwara Group ---Unconformity--- Bhiwara supergroup	ARAVALI GROUP UPPER Serpentinite Lakhavali Phyllite Kabita Dolomite Debari Formation MIDDLE Tidi Formation Bowa Formation Mochia Formation Udaipur Formation LOWER Jhamarkotra Formation Delwara Formation ---Unconformity---

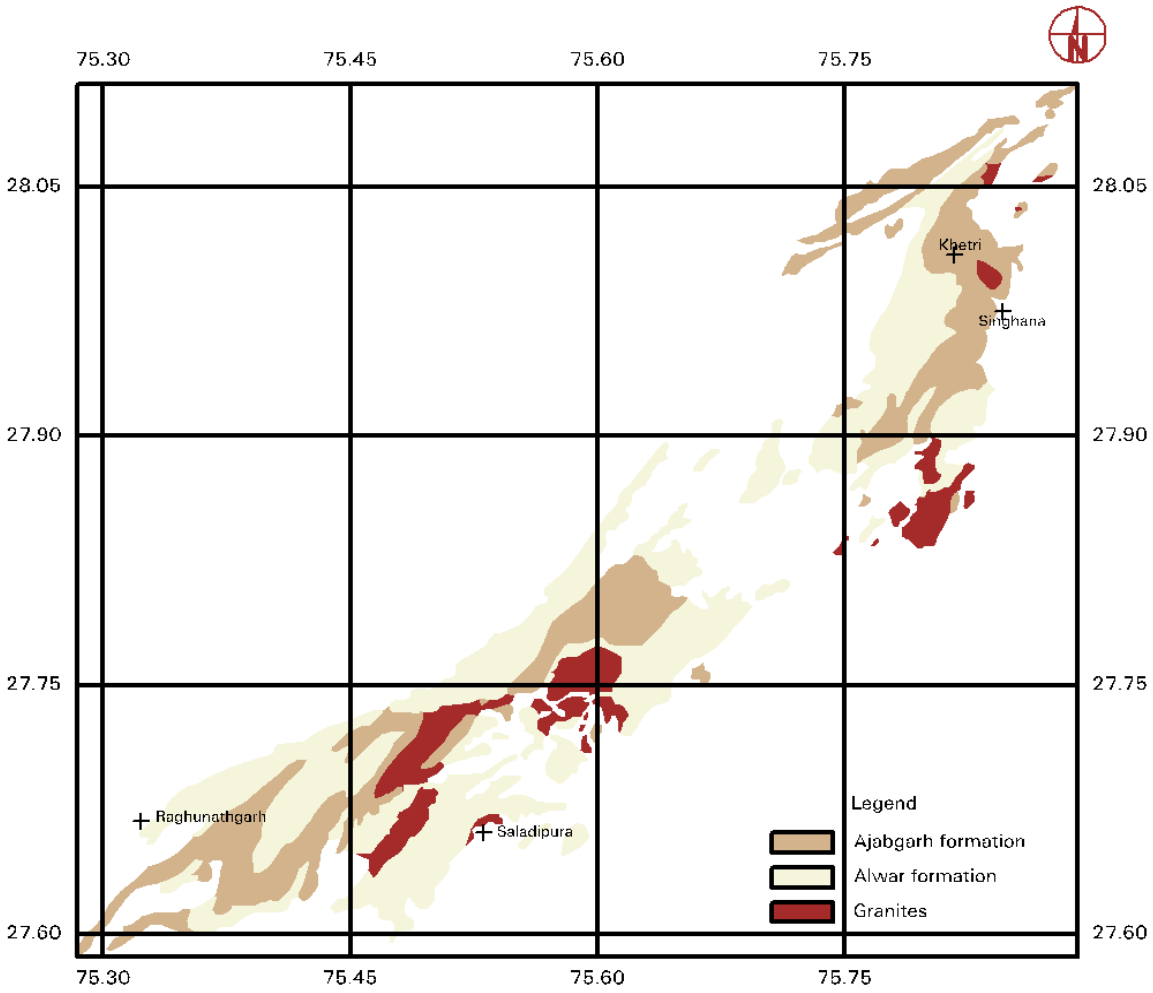

Fig. 2.2 a) Geological map of northern part of main Delhi basin

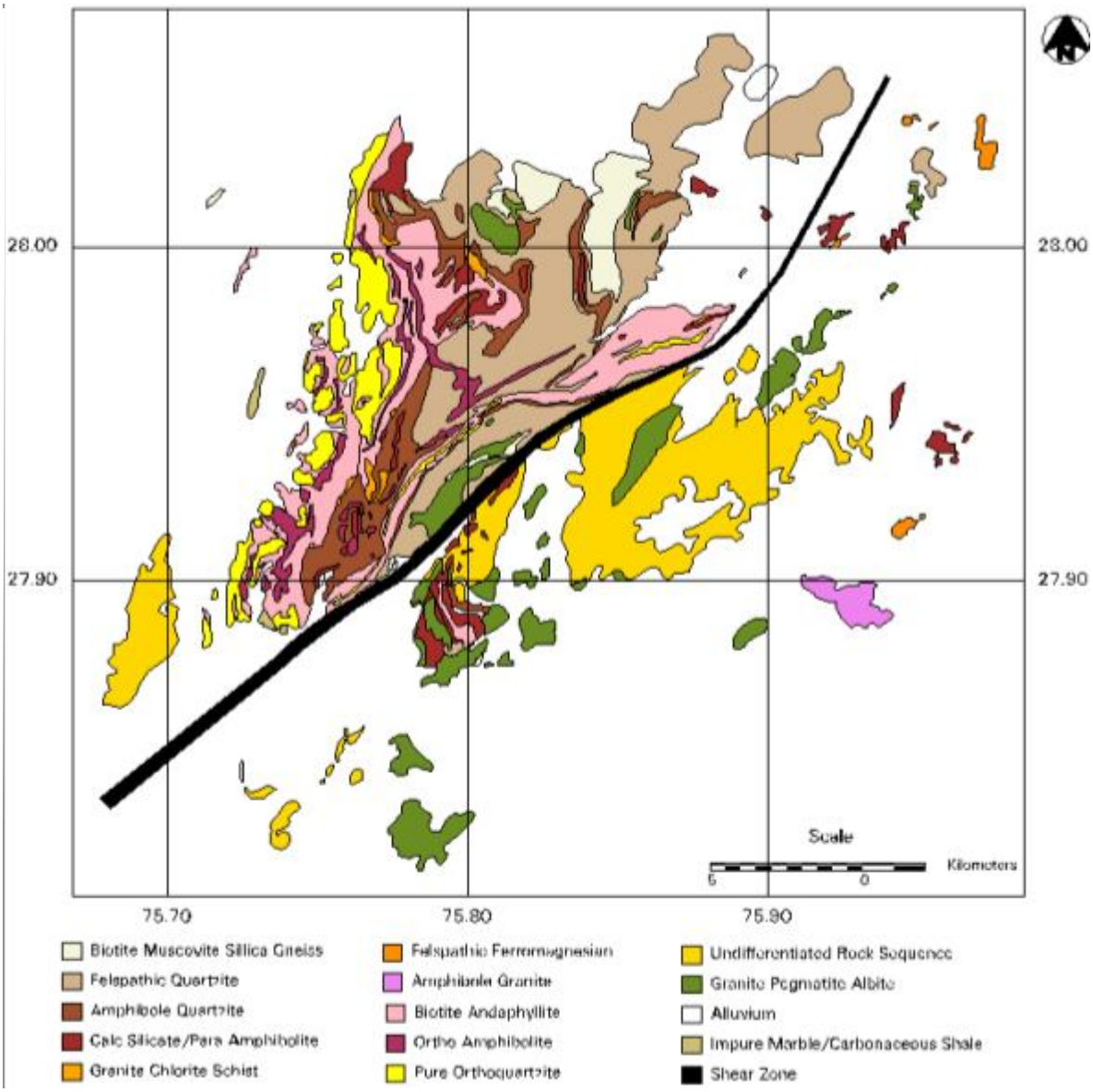

Fig. 2.2 b): Geological Map of the study area

Structurally the area is quite complex, and the region reveals a history of tectonic deformation with at least three generations of folding and faulting on micro, meso and macro levels. A large number of faults (longitudinal and transverse) and thrusts following the contacts or cutting across the various litho-units are present in the area (Fig. 2.3). They are marked by shear zones and often by alterations and mineralization.

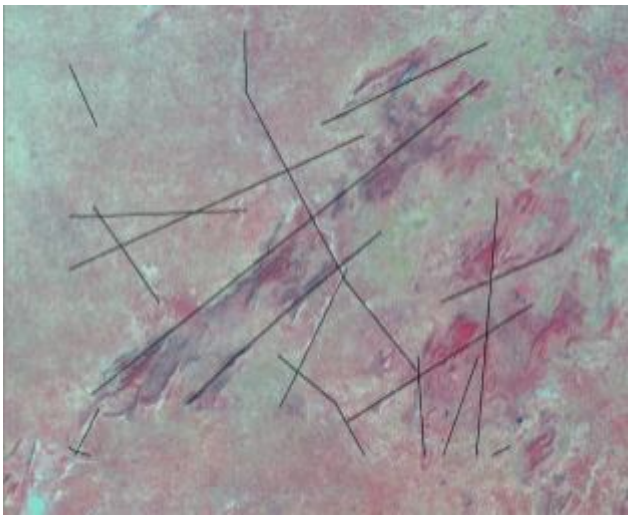

Fig. 2.3: Lineaments marked on ASTER image

2.4.3 Albitite zone

Albitite is a rare rock even at global standards and only a few occurances have so far been reported in India. Albitite is a porphyritic dike rock that is coarse-grained and composed almost entirely of albite. Randomly oriented subhedral laths of fine grained red coloured feldspar are the principal mineral of the albitites and the rock has a characterstic deep pink to brick red colour. Albitite is considered a valuable raw material for the ceramic industry. It is used as flux materials for ceramic tiles, white tiles and unglazed stoneware.

Albitite is not a common rock in nature which implies that the processes leading to albitization of host rock are also not very common. A few occurrences of albitite distributed in NNE-SSW trending zone has been described by Ray (1987) from south part of the KCB in western India. The northern extent of the zone was traced out by further detailed field investigations in the area. Ray and Ghosh (1989) designated this narrow 170 km long zone as Albitite Line or Albitite Zone. This 170 km long zone has been further traced out to be 320 km extending from Tal in the SW (Rajasthan) to Dancholi-Mewara in the NE (Haryana). The surficial albitite occurrences in Rajathan have been grouped into three sectors: Northern (Maonda-Sior sectors), Central (Khandela-Guhala) and Southern (Sakhun- Ladera).

The albitite occurrences within the Delhi metasediments extend from Mewara Gujarwas in the NE to Rohil in the SW. This belt is about 50 km long with a width of 8-10 km

(Yadav *et al.*, 2000). Number of uranium occurrences within the albitite zone have been discovered during last two decades (Yadav *et al.*, 2002). Genetic hypothesis regarding origin of albitites has fallen into two categories: magmatic origin along deep seated crustal fracture as envisaged by Ray (1990) and alkaline metasomatism, as given by Yadav *et al.* (2000).

The albitite zone lying towards the eastern fringe of Khetri sub-basin occurs in almost peneplained area. Albitisation has mostly affected metasediments of Ajabgarh group of rocks which is the upper stratigraphical sequence of Delhi supergroup (Dasgupta, 1968). There are granitic plutons Saladipura, Udaipurwati and Chapoli which are intrusive within the Delhi metasedimentaries, which fall into the age bracket of 1400-1500 million years. Mineral (biotite) of these granites have been dated around 700 million years, which has been interpreted to represent thermal resetting in response to granitic activity of 700 million years (Ray, 1987). Albitite zone is characterized by higher grade of metamorphism (sillimanite zone). The alkali metasomatic process has albititised metasedimentaries such as quartzite, calc silicate, phyllites etc. Entire albitised rock assemblage has been grouped under the term metasomatites (Yadav *et al.*, 2000). Dating of uraninite in albitites of the area by Rb/Sr method has indicated the age of quartz albitite to be in the range of 477-550 million years (Srinivasan, 2000). Two varieties of albitites are found, one is fine grained massive brick red coloured albitite occurring as isolated lenses of varying dimensions ranging in size from few meters to hundreds meter, whereas, the other variety consists of quartz albitites probably derived from coarse grained pegmatite as seen in the north eastern part of this zone.

CHAPTER 3

MATERIALS AND METHODS

The data used in this research has been categorized into two groups - remote sensing image data and ancillary data, consisting of geologic and topographic maps of the study area. In addition to these, a separate database comprising of field observations (field photographs and GPS-controlled field location data) and data generated in laboratory (petrographic and spectroradiometric data) have also been created (discussed in Chapter 4). In the following sections, the salient features of various kinds of data used in this study have been described.

3.1 REMOTE SENSING DATA

Remote sensing data of the study area comprises of:

a) ASTER Level-1B, 14-band at-sensor radiance data

b) Landsat ETM+ data

c) Cartosat –1 data

The remote sensing data have been selected for dates with minimum vegetation cover, since vegetation greatly affects the quality of radiation reflected/emitted by materials of geologic interest (rocks and soils) and obscures their spectral signatures.

3.1.1 ASTER

The Advanced Spaceborne Thermal Emission and Reflection Radiometer (ASTER) obtain high spatial and spectral resolution images of the earth's surface. The spatial resolution ranges from 15 to 90 m per pixel. There are 14 bands in the data covering from visible to thermal infrared wavelengths of the electromagnetic spectrum. ASTER was launched on the TERRA platform in December 1999. ASTER data specifications are given in Table 3.1

Table 3.1: ASTER Specifications

Launch date	18 December, 1999
Orbit	705 km, sun synchronous
Repeat cycle	16 days
Spatial Resolution	15-90 m
Swath width	60 km

ASTER provides extremely cost effective coverage and can be used for geological and environmental interpretation apart from various other applications (Prakash *et al*., 2011). ASTER data simultaneously covers the earth surface and provides images from the visible to the thermal infrared region of the EMS. It provides high radiometric and geometric resolution compared to its predecessors. It is equipped with exquisite optics that allow the instrument axis to move upto ± 24º for SWIR and TIR cross-talk direction from the nadir. The ASTER consists of three separate instrument subsystems: **VNIR** (Visible Near Infrared, **SWIR** (Short Wave Infrared) and **TIR** (Thermal Infrared). The band wise specifications are listed in Table 3.2

Table 3.2: ASTER Band Specifications (www.infoterra-global.com)

	Band Width	**Spatial Resolution (m)**
Band 1	0.52-0.60 µm (Green)	15
Band 2	0.63-0.69 µm (Red)	15
Band 3	0.76-0.86 µm (Near IR)	15
Band 4	1.60-1.70 µm (SWIR)	30
Band 5	2.145-2.185 µm (SWIR)	30
Band 6	2.185-2.225 µm (SWIR)	30
Band 7	2.235-2.285 µm (SWIR)	30
Band 8	2.295-2.365 µm (SWIR)	30
Band 9	2.36-2.43 µm (SWIR)	30
Band 10	8.125-8.475 µm (TIR)	90
Band 11	8.475-8.825 µm (TIR)	90
Band 12	8.925-9.275 µm (TIR)	90
Band 13	10.25-10.95 µm (TIR)	90
Band 14	10.95-11.65 µm (TIR)	90

3.1.2 Landsat

The Landsat series of satellites started way back in 1972 and have provided high quality multi-spectral data since then. Entire earth has been covered using these satellites and are stored in a worldwide archive of Earth observation data. Landsat 7 launched on 15th April 1999 has a better spatial resolution of 15 m in panchromatic band compared to its previous siblings. It is an ideal, multi-purpose, cost-effective tool for a huge range of applications (Woodlock *et al*., 2008). ETM+ data is enhanced version of TM with band 8 having a spatial resolution of 15 m (Plantonov *et al*., 2008). A summary of the band information for Landsat ETM+ is contained in the Table 3.3

Table 3.3: Landsat ETM Data Specifications

	Band Width	**Spatial Resolution (m)**
Band 1	0.45 - 0.515µm (blue)	30
Band 2	0.52 - 0.60µm (green)	30
Band 3	0.63 - 0.69µm (red)	30
Band 4	0.75 - 0.90µm (near infra-red)	30
Band 5	1.55 - 1.75µm (infra-red)	30
Band 6	10.4 - 12.50µm (thermal infra-red)	60
Band 7	2.09 - 2.35µm (near infra-red)	30
Band 8	0.52 – 0.9 µm	15

3.1.3 Cartosat-1

Cartosat-1 launched on May 5, 2005 is a state-of-the-art remote sensing satellite of ISRO (Vijayan *et al.*, 2012). Cartosat-1 has a 618 km high polar sun synchronous orbit. Cartosat-1 carries two panchromatic cameras that capture panchromatic stereoscopic images. The satellite images have a spatial resolution of 2.5 m and cover a swath of 30 km (Table 3.4). The cameras are mounted on the satellite in such a way that near simultaneous imaging of the same area from two different angles is possible. This facilitates the generation of accurate three-dimensional maps.

Table 3.4: Cartosat Data Specifications

Spatial resolution	2.5 m
Spectral Resolution a) No. of Bands b) Bandwidth	 1 Panchromatic 0.5 to 0.85µm
Radiometric Resolution a) Saturation Radiance b) Quantisation c) SNR	 55mW/cm^2/str/µm 10 bits 345 at Saturation Radiance
Swath (km) (Stereo)	30
Nominal Altitude	617.99 km
Orbital Repeat Cycle	116 days
Max. Wait Time for Revisit	5 days
Node for P/L Operations	Descending Node
MTF a) Across track b) Along track	 20 23
Nominal B/H Ratio for Stereo	0.62
Orbital Parameters: a) Semi-major axis b)Eccentricity c) Inclination	 6996.128 km 0.001 97.87°
Data Rate	105 Mb/s
Integration Time (ms)	0.336
Data Compression: a) Algorithm b) Compression Ratio	 JPEG Max. 3.2

3.2 ANCILLARY DATA AND CREATION OF A GIS DATABASE

Ancillary data in the form of topographic maps and geologic maps of the study area in analog (hardcopy or paper) format have been processed to create a geocoded coregistered digital database using standard GIS tools. In addition to this, a DEM has been generated from Cartosat-1 stereo image pair of the study area using standard stereo processing methodology.

The standard GIS processing involves conversion of analog data into digital format either as raster images or vector shapes, followed by georeferencing the data layers based upon a user-defined geographic reference system (Behera *et al.*, 2011). In this study, the topographic maps have been scanned, then georeferenced using geographic Latitude/Longitude coordinate system with WGS84 datum. The topographic maps are then used to create a topographic base map of the study area.

One of the basic requirements of this research is the availability of a geologic map to be used for ground-truth and to validate the results of remote sensing spectral analyses. Geologic map published by GSI on 1:50,000 scale in 1997 is taken for basic lithlogical units. The data given in Table 3.5 is used to create ancillary data required for the research.

Table 3.5: Ancillary Data used in the Study

Data	Scale	Year of production
Survey of India (SOI) Toposheet No. 45M/9, 45M/13,	1:50,000	1985-87
Geological Survey of India (GSI) Geological Map	1:50,000	1997

Using the data mentioned in table 3.5, following ancillary data is created:

3.2.1 Base map: A base map is a map on which primary data and interpretations can be plotted. A base map incorporates roads, railways, major drainage, administrative boundaries, major settlements and forest boundaries. The base map of the study area was prepared using the Survey of India toposheets. Fig. 3.1 shows the base map of the area. The map depicts various metalled roads, unmetalled roads and footpaths in the study area. A railway track with railway station at Dabla is also shown. Major settlements such as Khetri, Babai, Mavanda Tarla, Mewara Gurjawas, Mewara Jatuwas, Tibba Basai, Dabla etc. also shown. Some part of the study area is under resesrved forest.

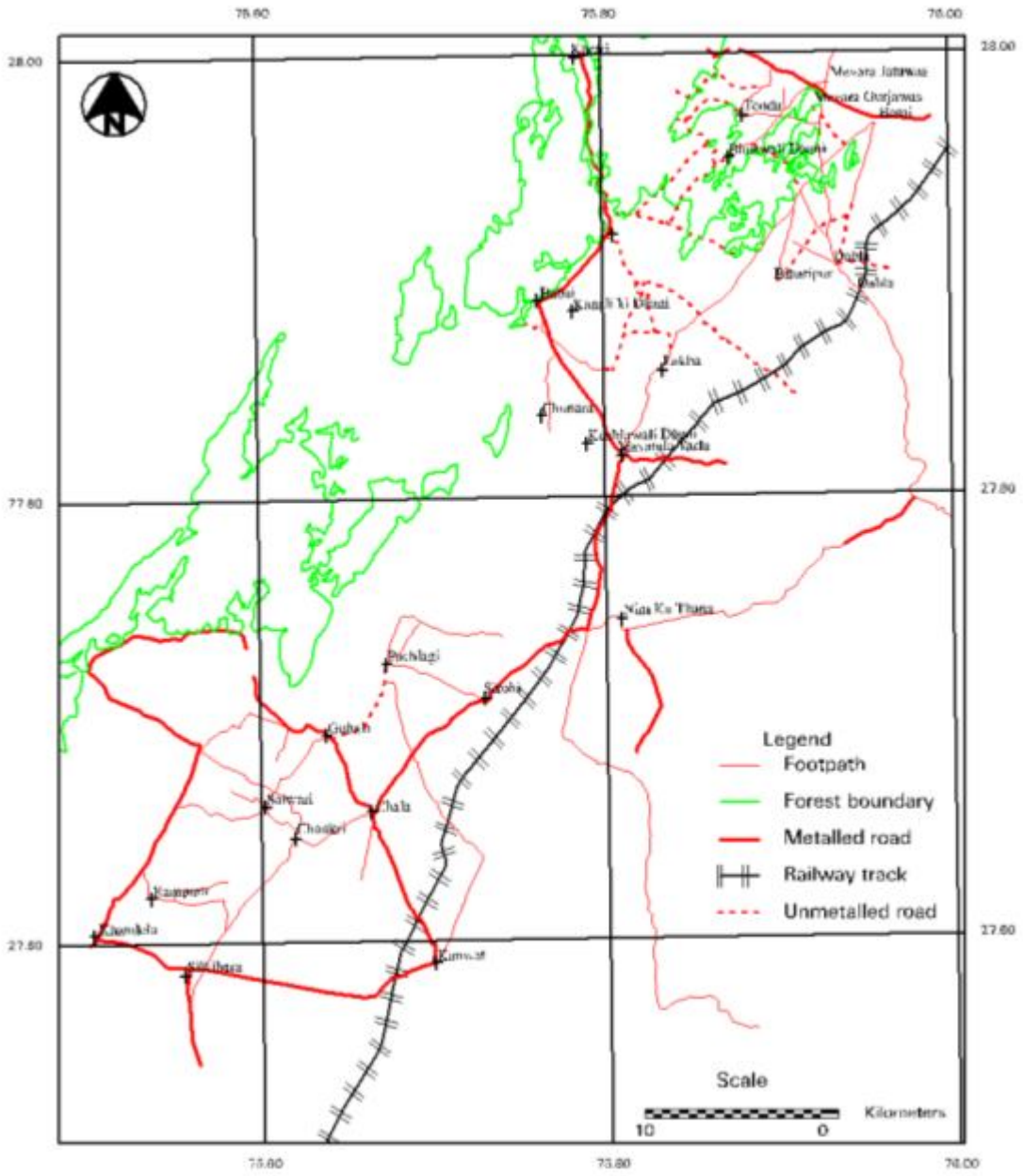

Fig. 3.1: Base Map of the Study Area

3.2.2 Drainage map: Drainage responds rapidly to tectonic changes and thus it can be used for tectonogeomorphological analysis (Agarwal *et al.*, 2008). The orientation of drainage is also helpful in identification of lineaments (Bali *et al*., 2009 and 2011). The drainage pattern in an area is dependent on the lithology of the area. The drainage map is prepared using SOI toposheets. The major river of the area is Kantli river which flows from NW to SE of the study area separating north KCB and south KCB. The boundary of

Kantli river is taken from the satellite image and the smaller streams are taken from toposheet. In general, the drainages are radial to dendritic in pattern. The maximum drainage order is seven. Fig. 3.2 shows the drainage map of the study area.

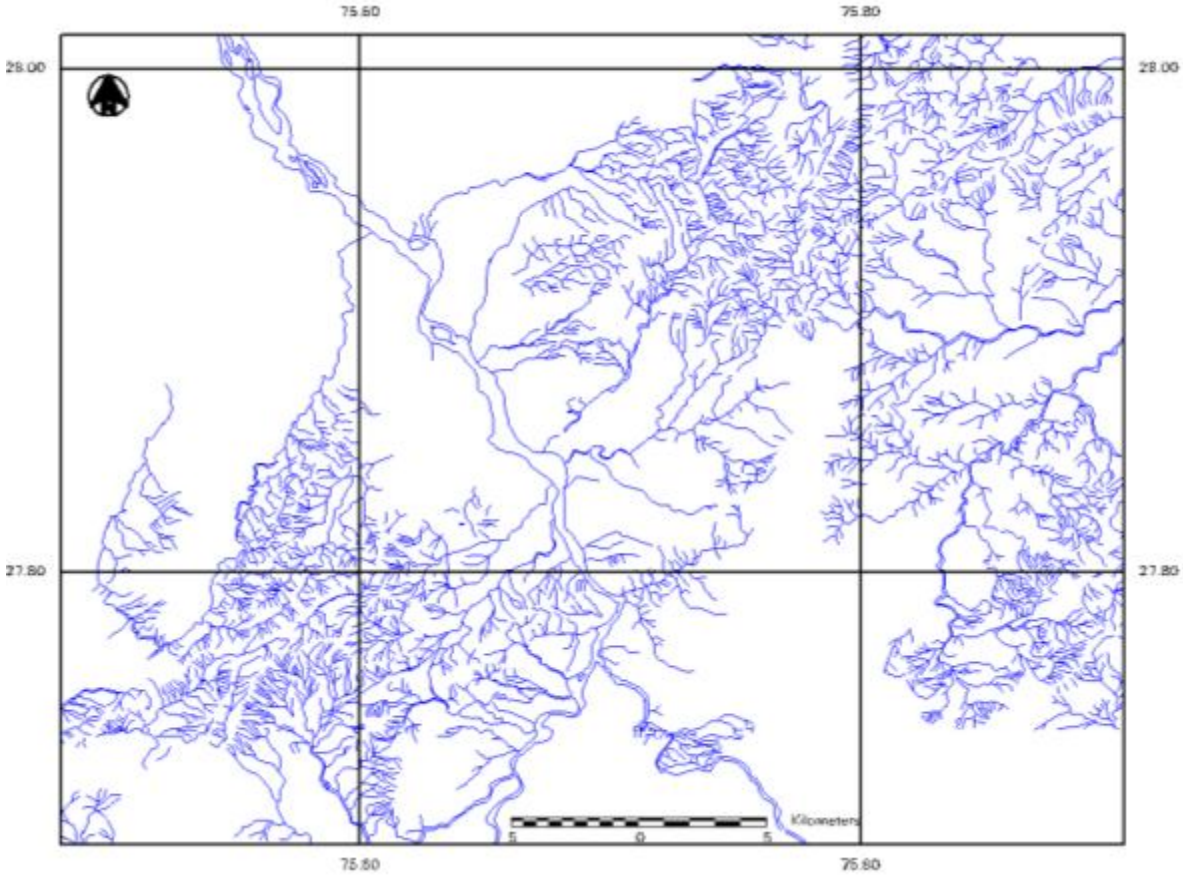

Fig. 3.2: Drainage Map of the study area

3.2.3 Contour Map: Contour lines are the lines drawn on the map connecting points of equal elevation. Contours at a contour interval of 20 m are digitized from the SOI toposheet. The study area includes both dense contours and sparse contour area. Dense contours are seen in north and south KCB areas and remaining part shows sparse contours. The minimum elevation in the area is 380 m and the maximum elevation is 762 m. Fig. 3.3 shows the contour map of the study area.

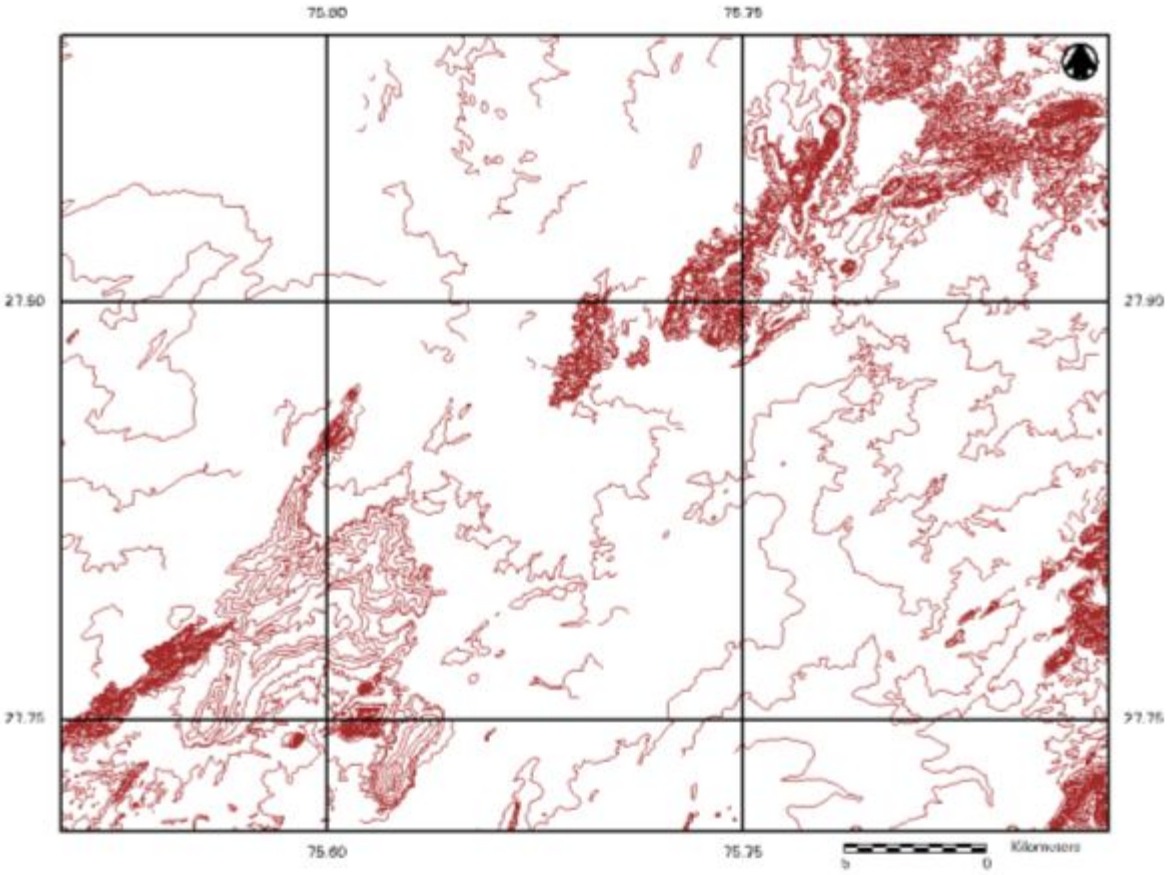

Fig. 3.3: Contour Map of the study area

3.2.4 Geology map: The area represents a regionally metamorphosed terrain with low to medium grade metasedimentary rocks, such as various kinds of quartzites (banded feldspathic quartzites. micaceous quartzites, amphibole bearing banded quartzites, arkosic and banded arkosic quartzites, and pure quartzites) and metapelites (schists and phyllites), and has witnessed a history of polyphase intrusions of intracratonic felsics and mafics (granites, granodiorites and pegmatites, and amphiholites, respectively). Geologic map published by GSI in 1997 was taken for basic lithlogical units. A detailed geologic map of the area is shown in Fig. 2.2 b.

3.2.5 Lineament Map: Lineament map is interpreted from ASTER data and digital surface model (DSM) of Cartosat-1 data (Fig. 6.2).

3.3 FIELD AND LABORATORY DATA

Field visit during December, 2010 has been carried out to collect field data and samples for subsequent laboratory investigations. The details of the sampling and analysis techniques and results obtained have been provided in Chapter 4. The albitite zone already reported in literature is used as a reference for collecting rock samples. The samples are collected throughout the width of the albitite zone so as to cover different stages of albitisation. A few adjoining locations were also visited to identify the host rock and understand the process of albitite emplacement. The rock samples collected during the fieldwork have been subsequently analyzed through petrographic microscopy and spectoradiometry.

3.4 SOFTWARE TOOLS

A variety of GIS and image processing software tools have been used to process the remote sensing and ancillary geodata. Image analysis for Landsat and ASTER data is carried out using ENVI, ERDAS Imagine (version 9.1) software. Customized application for Directed Principle Component Analysis (DPCA) was developed using IDL. Data classification and comparison was done in ENVI (version 3.3). Ancillary data is generated using vector module of Erdas Imagine. Standard digital image processing and vector graphics software have been used for creation and editing of the manuscript and figures shown in this thesis.

3.5 METHODOLOGY OVERVIEW

The broad conceptual framework and methodology adopted in this research has been shown in Fig. 3.4.

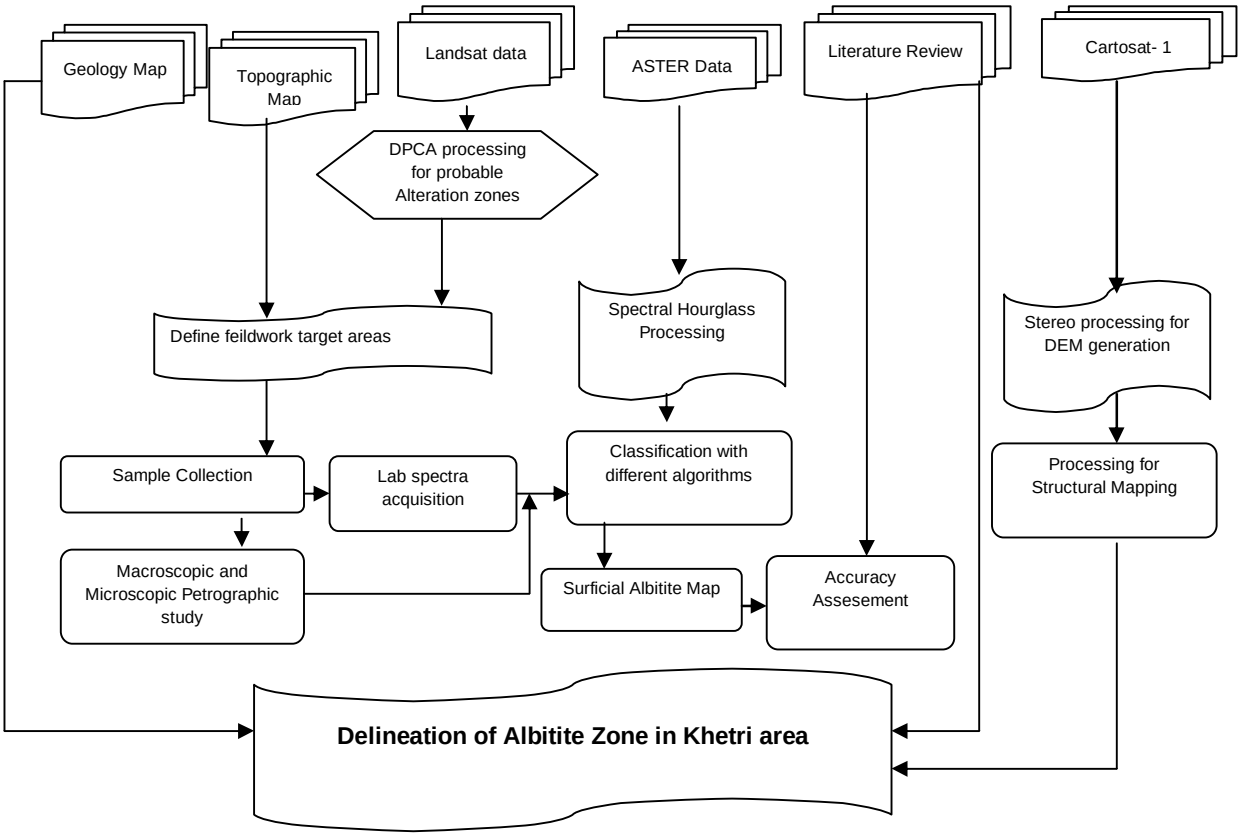

Fig. 3.4: Procedural flowchart of the methodology

3.5.1 Sample Collection and Preparation

The primary objective of field and laboratory studies is to locate the different rock types and to generate the spectral response curves since the combined response of surface materials within a pixel controls the spectral response recorded by the remote sensor. The sample sites are carefully selected based on existing geology map, results of DPCA analysis of Landsat and ASTER data and other ancillary information generated from toposheet. A total of 20 field samples are collected from the study area. These samples represented various stages of albitisation and also various rock types exposed in the study area. The field samples are subjected to detailed petrographic study. The samples are examined in the hand specimen and also thin sections are studied under the microscope. The exercise is carried out to determine the mineral constitution of the rocks. Emphasis has been laid upon identification of the primary and alteration mineralogy. Further spectral response curves pertaining to VNIR-SWIR region of the electromagnetic

spectrum are generated using ASD spectroradiometer. Reflectance curves pertaining to TIR region of electromagnetic spectrum are taken from the ASTER image at the sample sites. The image spectra from the spatial location of the sampled sites are used as reference spectra in TIR region of electromagnetic spectrum. Sample data collection and reflectance spectra generation is explained in detail in Chapter 4.

3.5.2 Preprocessing of the data

Mineral identification from remote sensing data is a challenging task. A number of preprocessing steps have to be applied before the data can be used for classification. When the emitted or reflected energy signal of an object is recorded at a short distance, it generally does not coincide with the measurements of the same object by a satellite sensor. This is because of atmospheric conditions, sun's azimuth and elevation. Apart from these atmospheric conditions, the response of the sensor also influences the observed energy. Thus, to obtain the actual reflectance which can be compared to ground measurements, these radiometric errors creeping in, because of atmosphere and sensor itself must be corrected. The raw ASTER image consisted of 14 bands. The first nine bands correspond to VNIR and SWIR wavelengths and the last five bands are for TIR wavelengths. Atmospheric correction of VNIR-SWIR bands has been carried out using Fast Line-of-sight Atmospheric analysis of Spectral Hypercubes (FLAASH) and Atmospheric and Topographic Correction (ATCOR) algorithms. The five thermal bands are atmospherically corrected using 'Thermal Atmospheric Correction' program in ENVI. The radiometrically corrected image is subjected to geometric correction using GCP from Landsat image. Preprocessing of the satellite data is explained in Chapter 5.

3.5.3 Data Processing

Data processing is carried out in various steps.

A) DPCA Processing of Landsat and ASTER data

Crosta technique, also known as feature oriented principal components (PC's) selection aims at calculation of principal component images from the raw image. These PC's are analyzed so as to identify principal components which contain the spectra information about the specific mineral. The contribution of each of original

bands to the components is also calculated as the loading factor. This is done in relation with spectral response of the specific mineral of interest. The magnitude and sign of the eigenvectors loadings is analyzed to indicate whether the materials will be represented as bright or dark pixels in the principal components (Crosta and Moore, 1989; Rutz-Armenta and Prol-Ledesma, 1998). ETM+ data of Khetri area (acquisition date 23/6/2001) is used for this study. The image is cloud free. The image is geometrically and radiometrically corrected. The spectral reflectance curve of the individual minerals are analyzed and the dips and peaks are correlated with the dataset bands. These selected bands are then utilized for principal component analysis. To calculate the loading of individual bands onto the principle components, formula used is:

$$R_{KP} = (a_{kp} * \sqrt{\lambda_p}) / \sqrt{Var_k} \text{----------3.1}$$

Where:

R_{KP} = loading of band k on component p

$a_{k,p}$ = eigenvector for band k and component p

λ_p = p^{th} eigenvalue

Var_k = variance of band k in the covariance matrix

DPCA processing of Landsat and ASTER data is dealt in detail in section 6.1.

B) Cartosat - 1 Data Processing

In order to analyse the correlation between the tectonic activity and albitite emplacement in the study area, through investigation of the albitite zone should be carried out along with the lineaments. Thus a 3D model is generated using Cartosat-1 data to demarcate the lineaments in the area. Cartosat -1 stereo data for the area is acquired. Even though Cartosat -1 data contains rational polynomial coefficients which are capable of establishing a relationship between image and ground coordinates, still some ground control points are required for proper orientation of the stereo model. The ground control points are collected using single frequency geodetic Global Positioning System (GPS). Since the study area is not covered in one scene thus adjoining stereopairs in latitudinal direction are processed and surface models are merged to obtain a seamless elevation information over the area. The derived

surface model was examined visually and digitally to enhance the lineaments in the area. Stereo processing of Cartosat -1 data is explained in section 6.2.

C) Spectral Processing of ASTER VNIR SWIR and TIR data

Various classification techniques are applied on atmospherically and geometrically corrected ASTER image. Spectral Angle Mapper (SAM), Mixture Tuned Matched Filtering (MTMF) and Spectral Feature Fitting (SFF) are used for classifying albitite rich areas. For VNIR-SWIR bands the reference spectra collected from the ground samples is used as end member. For thermal bands the end members are collected from the ASTER image at the ground surveyed locations. The SAM algorithm calculates the spectral angle between the reference and unknown spectra and uses it as a measure of similarity and discrimination. SAM algorithm is utilized for albitite end member in the study area. The output from SAM is a classified image and a set of rule images. The rule images indicate the spectral angle in radian between the reference and the unknown spectra. Lower values represent better match with the endmember spectra, thus higher probability of target of interest. MTMF algorithm was carried out on all the 14 components derived from Minimum Noise Fraction (MNF)transformation. MTMF algorithm finds out abundances of user defined end members and thereby carries out a partial unmixing of the endmembers. Output of MTMF algorithm is a score and infeasibility image. Both the score and infeasibility images are integrated to generate a final classified output. Score and infeasibility images for albitite are generated and analyzed. SFF algorithm works on continuum removed reference and image spectra. SFF matches the reference endmember with the unknown spectra based on absorption features. A least square fit is calculated band by band between the image spectra and reference endmember. An RMS image is created for each endmember from the total root mean square error in matching. A scale image can also be calculated which is a measure of similarity between the reference and the image spectra on pixel by pixel basis. Spectral processing of ASTER data for albitite mapping is dealt in detail in section 6.3.

CHAPTER 4

FIELD AND LABORATORY STUDIES

The main objective of the field and laboratory exercises has been to generate reference data to be used for further classification. The field work is carried out to identify locations with prominent albitite emplacement. In order to collect the rock samples from the location, a detailed field survey is required. Thus after proper planning a field visit has been carried out in December, 2010.

The field work is aimed at collecting samples representing various stages of albitisation. These samples are analyzed petrographically and to understand the extent and characteristics of albitite emplacement in the area. The rock samples are collected from the reported albitite zone. The adjoining areas are also sampled to identify the host rock for the process. The analyses have involved field data collection (field photographs, GPS locations of type-rock areas and albitised areas, and their field sampling); petrography of rock thin-sections to understand the bulk mineral constitution, especially albitite in the rock samples. The rock samples are studied with spectroradiometer to generate the reference spectra and to establish interrelationship between the nature of geologic information recorded by remote sensing (ASTER images) and its real-world occurrence.

4.1 AREA SELECTION AND DEFINITION OF ANALYTICAL OBJECTIVES FOR FIELD AND LABORATORY STUDIES

The literature review indicated a narrow zone of albitisation in the KCB area. Ray (1987) studied the ore mineralization and albitite occurrences in KCB area. He is among the first author to trace the regional extent and age of the albitite present in the study area. The total longitudinal extent of the reported albitite zone is divided into three parts: Sakhun, Khandela-Guhala and Maonda Babai Sior (Ray, 1990). The study area selected in the present work covers two of these three sectors namely: Khandela-Guhala and Maonda Babai Sior.

Preliminary study based on Landsat ETM data of the study area have indicated the existence of some clay minerals and chlorite in the amphibolites, banded amphibole quartzite and pegmetites constituting the anomalous zone. Few sites are identified based

on the reported albitite occurrences and accessibility. A total of 20 field samples were collected from different locations representing the various rock types exposed in the study area. The details of the results obtained from the studies have been explained in subsequent sections.

4.2 FIELD STUDIES AND SAMPLE COLLECTION

Small treks are carried out near Kushwali ki Dhani, Mewara Gujarwas Jaturwas junction towards Jaturwas and Dabla areas. Several locations were studied on the way and the samples were collected (Fig. 4.1, 4.2 and 4.3). Table 4.1 comprises of geographical location of all the sites visited along with the rock type.

Table 4.1: Description of Field Measurement Locations

Location	Lat/Long	Rock Type	Sample/Photo
1	27° 49.329′N, 75° 46.902′E	Phyllite (country rock) with pegmatite veins	
2	27° 49.186′N, 75° 46.800′E	High angle dipping country rock. Striking north south. Dip 75-80° west	Sample 1
3	27° 49.213′N, 75° 46.772′E	Country rock exposure striking north south. High angle dip. Dipping west 70°	Photo 2
4	27° 49.202′N, 75° 46.747′E	Country rock striking NS	
5	27° 49.181′N, 75° 46.740′E	Country rock	
6	27° 49.293′N, 75° 46.673′E	Country rock	
7	27° 49.293′N, 75° 46.673′E	Country rock strike EW	
8	27° 49.275′N, 75° 46.636′E	Pegmatite veins in country rock	Photo 1
9	27° 49.254′N, 75° 46.609′E	Pegmatite veins in country rock. Partially albitized typical bonding nature	
10	27° 49.301′N, 75° 46.324′E	Partially and some places totally albitized. Striking SW-NE high clip 75°-80°	

11	27° 49.308′N, 75° 46.621′E	Large no. of veins. Typical bonding calc silicate rock	Sample 2 & 3
12	27° 49.487′N, 75° 46.710′E	Albitite /Country rock weathered scattered patches small mounds of albitite red coloured.	Sample 4 & 6 Photo 3
13	27° 49.556′N, 75° 46.764′E	Pegmatite vein	
14	27° 49.582′N, 75° 46.714′E	Pegmatite vein striking EW	
15	27° 49.600′N, 75° 46.658′E	Albitite might be continuation of pegmatite white coloured	
16	27° 49.621′N, 75° 46.683′E	Phyllite (country rock) intruded with pegmatite	
17	27° 49.685′N, 75° 46.800′E	Pegmatite vein in country rock	Photo 4
18	27° 49.709′N, 75° 46.836′E	Pegmatite vein in country rock	
19	27° 49.556′N, 75° 46.897′E	Loose material	Photo 5
20	27° 49.556′N, 75° 46.897′E	Calcium silicate rock with vein	Photo 6
21	27° 49.399′N, 75° 46.957′E	Small outcrops (5-6). Mica schist quartzite/amphibole quartzite with pegmatite veins	Sample 7
22	27° 49.438′N, 75° 46.984′E	Pegmatite veins	Sample 8
23	27° 55.358′N, 75° 48.799′E	Calcium silicate rocks. Amphibolite rock cutting country rock	
24	28° 2.252′N, 75° 56.872′E	Sand stone + iron ore, quartz vein with felspar	Sample 11 & 12 Photo 7
25	28° 1.768′N, 75° 57.069′E	Felspathic quartzite but appear like granite	Sample 13, Photo 8
26	28° 1.130′N, 75° 56.915′E	Felspatic rich sandstone	Sample 14, Photo 9
27	28° 1.084′N, 75° 56.893′E	May be partially albitised , flesh red coloured minerals (plagio clase) visible	Sample15, Photo 10 & 11
28	28° 0.704′N, 75° 55.801′E	Banded calcium silicate carbonate rich part remains inside and SiO_2 rich in outside, so rock very hard.	Sample 16, Photo 11

29	28° 0.529′N, 75° 55.423′E	Thick calcite vein altered into red soil. Vein activity is soft , top is banded and hard, carbonate vein + altered product of country rock	Sample 17, Photo 12
30	28° 0.358′N, 75° 55.634′E	Brecciated appearance , limonitic, calcite, Fe ore , mica , etc in brecciated appearance.	Sample 18 & 19, Photo 13
31	28° 0.007′N, 75° 55.244′E	Fe ore rock	Sample 20, Photo 14
32	27° 58.842′N, 75° 55.626′E	Amphibole quartzite with pegmatite vein.	Sample21
33	27° 58.874′N, 75° 55.546′E	Partially albitised, banding visible.	Sample 22, Photo 15
34	27° 58.872′N, 75° 55.525′E	Fully albitised, typical felspar flakes	Sample23, Photo 16
35	27° 53.902′N, 75° 56.151′E	Granite-typical weathering pattern of granite	Photo 17 & 18

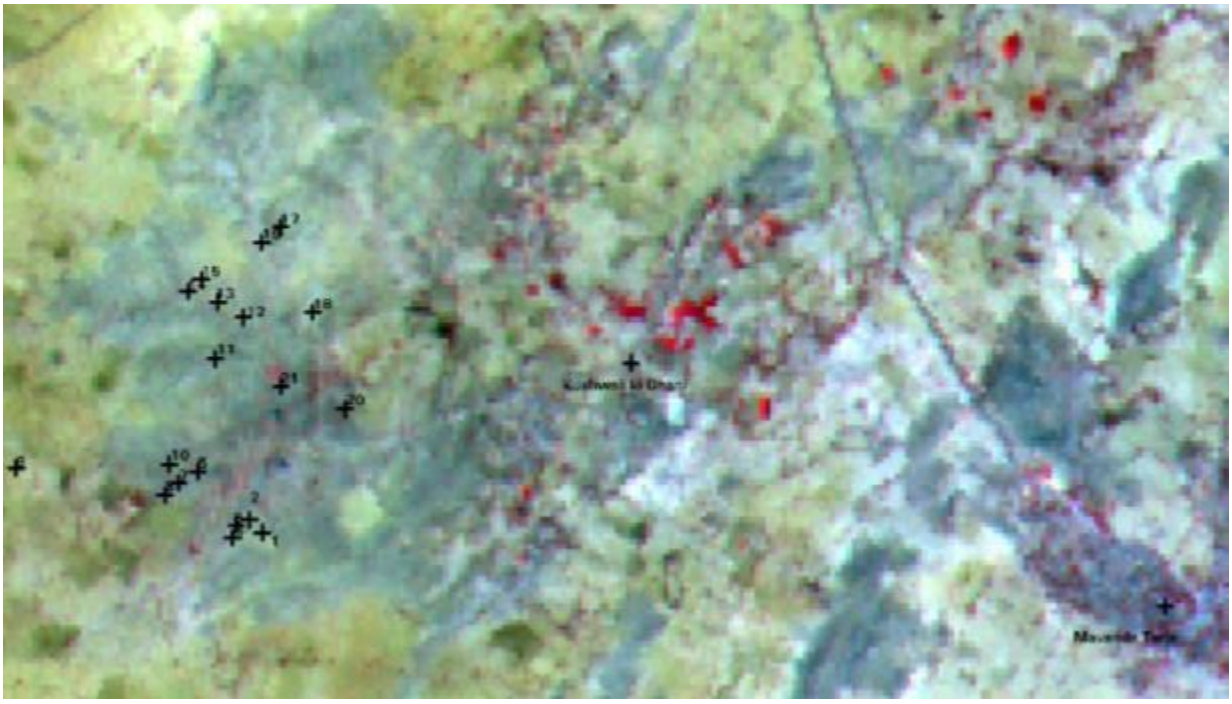

Fig. 4.1: Field Locations at Kushwali ki Dhani near Mavanda Tarla

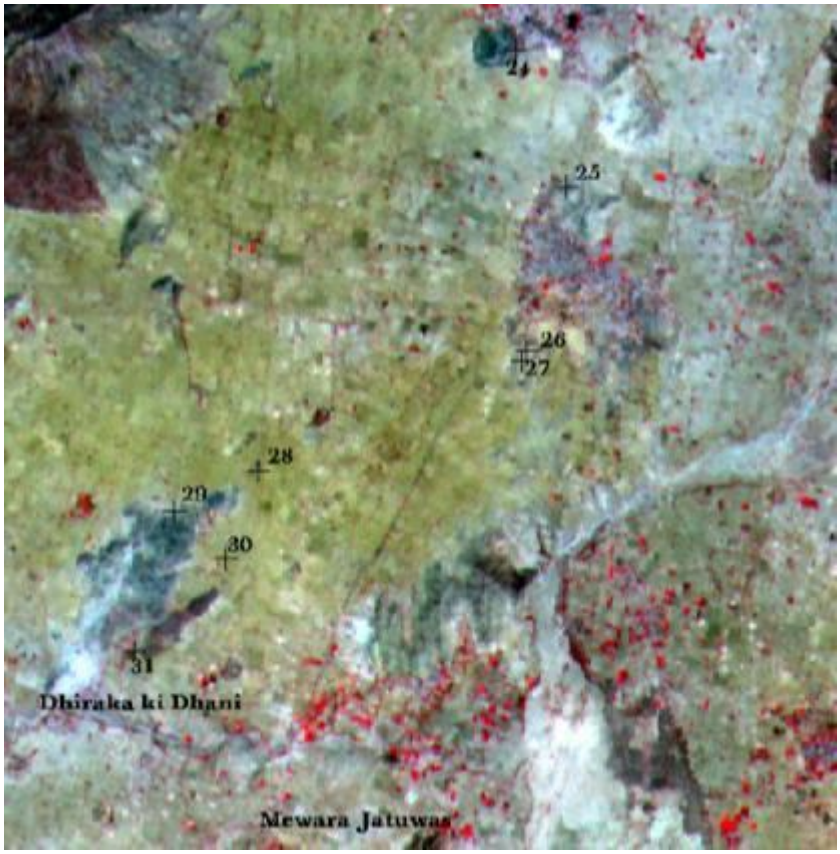

Fig. 4.2: Field Locations near Mevara Jatuwas

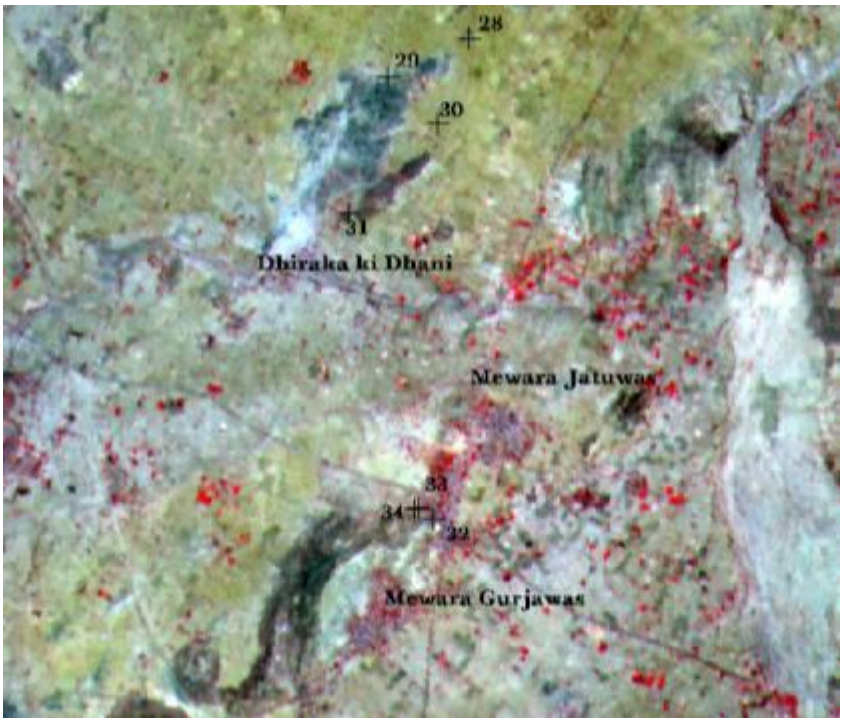

Fig 4.3: Field Locations near Mevara Gurjawas and Mevara Jatuwas

Photo1: Pegmatite Vein in Country Rock

Photo2: Country Rock striking N-S

Photo3: Small Mounds of albitite

Photo4: Pegmatite vein in country rock

Photo5: Loose material

Photo6: Calc silicate banded rock

Photo 7: Sandstone and Iron Ore

Photo 8: Felspathic quartzite

Photo 9: Felspathic rich sandstone

Photo 10: Banding in partially albitized country rock

Photo11: Pegmatite vein in partially albitized rock

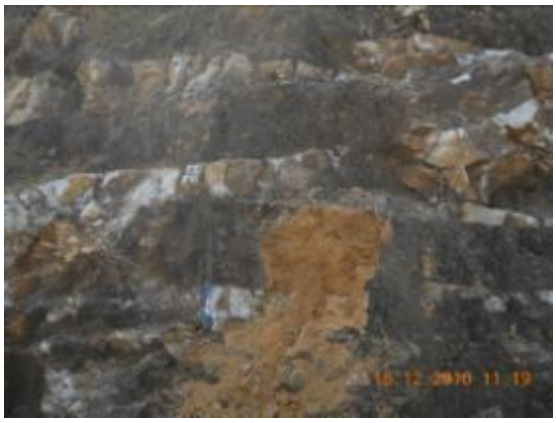

Photo 12: Thick calcite vein

Photo13: Iron Ore Copper Gold

Photo14: Iron Ore Rock

Photo 15: Partially albitized banded rock

Photo 16: Fully albitized rock

Photo17: Dabla Granite

Photo 18: Dabla Granite

4.3 PETROGRAPHIC STUDY OF THE COLLECTED ROCK SAMPLES

The rock samples are collected from the albitite zone, various rock types exposed in the study area and also from the areas depicting altered mineralogy. Macro and Micro petrographic analysis of the samples is carried out. These rock samples are examined under the microscope to ascertain the mineral composition of the rocks and also to find out about their alteration. Primary and alteration mineralogy are identified in the rock samples. Effects of secondary weathering and the role of rock texture has been studied in greater detail as they have direct impact on the reflected electromagnetic radiation reaching the remote sensor. The characteristics of individual samples are described in following sub sections.

Sample 1

Sample collected from the banks of lake at Kushwali ki Dhani near Mavanda Tarla at latitude longitude 27° 49.186′N, 75° 46.800′E. Fine grained rock exhibits banding. Amphibole bearing felspathic quartzite. Insepient banding visible. Feldspar include K feldspar mainly microcline and minor plagioclase. Some grains showing yellow pleochroism might be epidote or staurolite (Fig. 4.4).

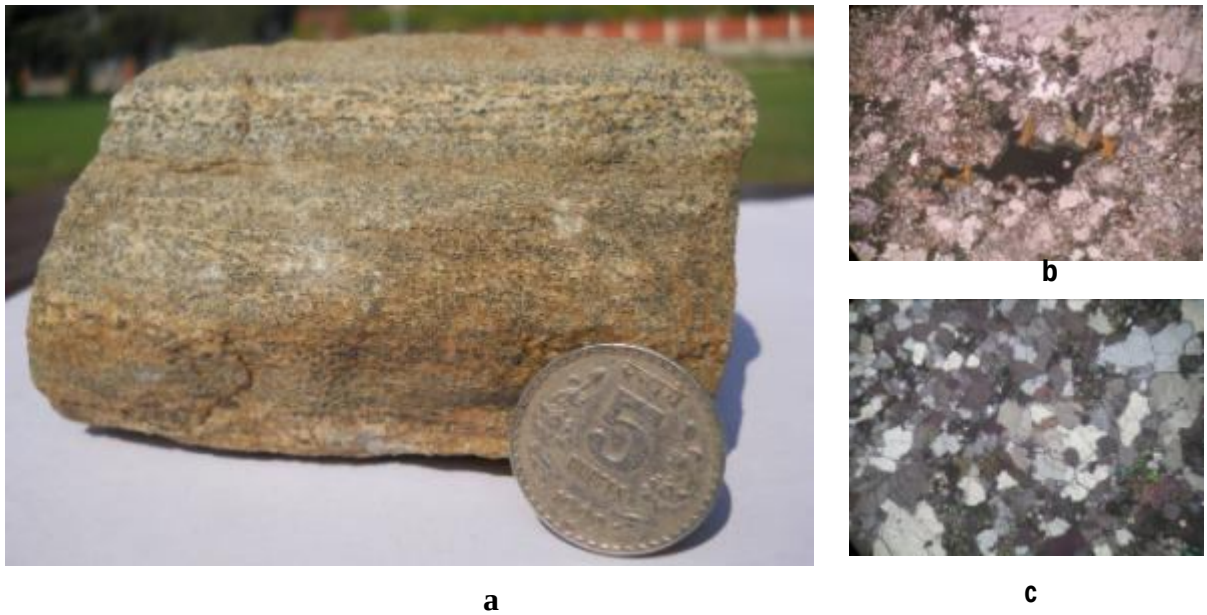

a **b** **c**

Fig. 4.4: Sample 1 a) Hand specimen b) Thin section 40x ppl c) Thin section 40x c

Sample 2

Sample is collected from the banks of lake at Kushwali ki Dhani near Mavanda Tarla at latitude longitude 27° 49.308′N, 75° 46.621′E. Fine to medium grained rock exhibits a clear banding between ferro magnesium and quartz. Within thick quartz vein some black ferro magnesium minerals are present. More feldspar and opaques with some micaceous minerals present. Some weathering also seen. Bands with large mica content mainly biotite. Feldspar include plagioclase and more K feldspar. Interlocking texture is visible. Grain boundaries are irregular (Fig. 4.5).

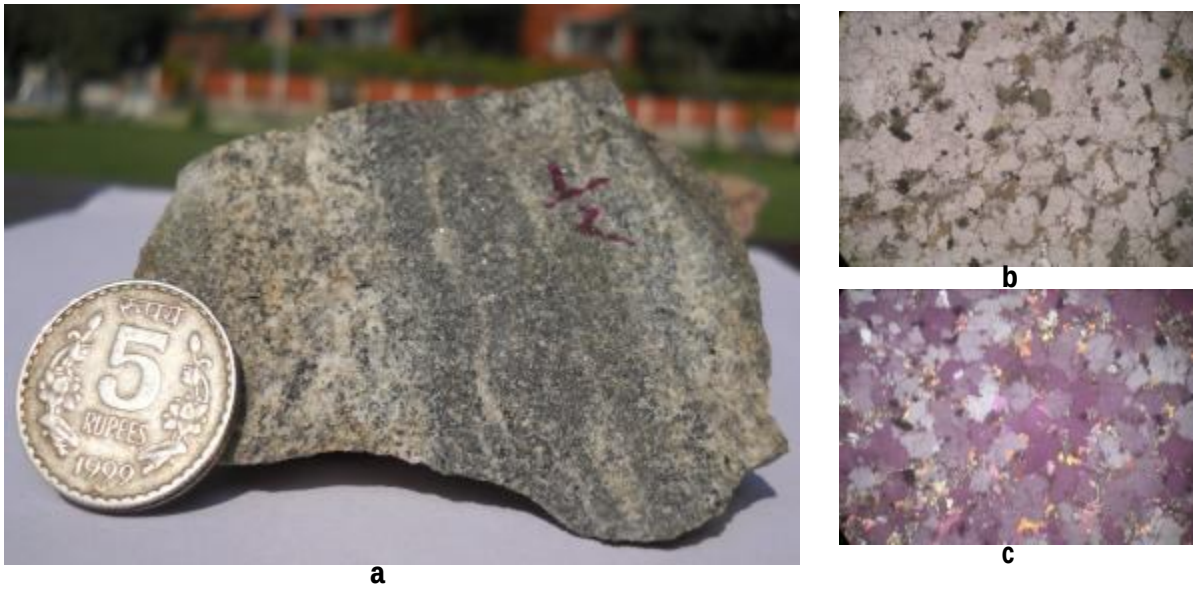

Fig. 4.5: Sample 2 a) Hand specimen b) Thin section 40x ppl c) Thin section 40x c

Sample 3

Sample collected from the banks of lake at Kushwali ki Dhani near Mavanda Tarla at latitude longitude 27° 49.308′N, 75° 46.621′E. Overall massive, fine grained, quartz vein. Colour – dark grey. Feldspar, ferro magnesium, disseminated mica present. Some banding visible, partially weathered. Mineralogy similar to sample 2. It is more mafic rich. Some grains of amphibole visible (Fig. 4.6).

Fig. 4.6: Sample 3 a) Hand secimen b) Thin section 40x ppl c) Thin section 40x c

Sample 4

Sample collected from the banks of lake at Kushwali ki Dhani near Mavanda Tarla at latitude longitude 27° 49.487′N, 75° 46.710′E. Medium to Coarse grained massive igneous rock, pink in colour. Dominant plagioclase with ferro magnesium mineral and some dark red spots. Mineralogy includes feldspars, amphibole, Fe ore, epidote and many opaques. Amphibole has altered into chlorite. Albitite injection clearly seen in thin crack veins (Fig. 4.7).

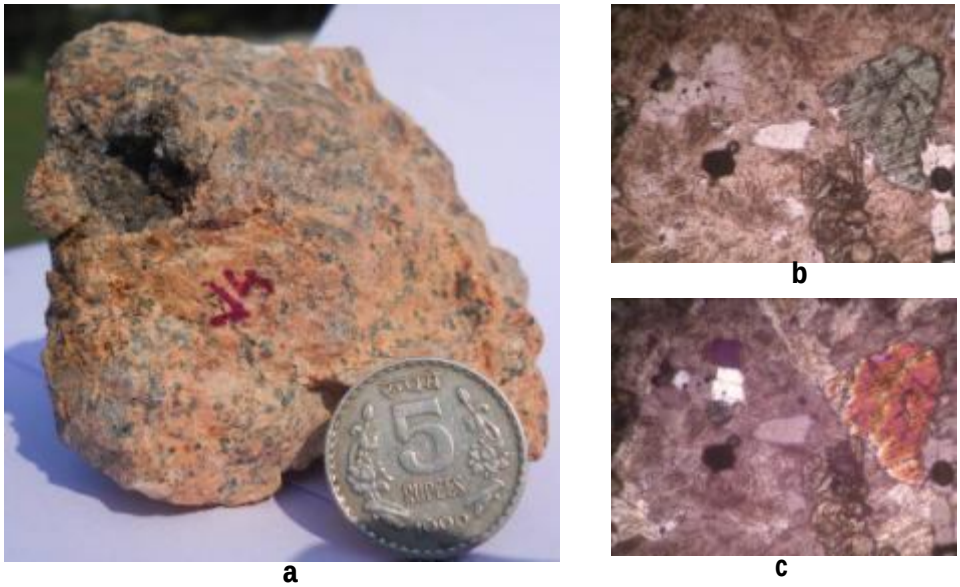

Fig. 4.7: Sample 4 a) Hand specimen b) Thin section 40x ppl c) Thin section 40x c

Sample 7

Sample collected from the banks of lake at Kushwali ki Dhani near Mavanda Tarla at latitude longitude 27° 49.399′E, 75° 46.957′N. Fine to medium grained massive rock. Dark grey in colour. Pure quartzite. Pegmatite veins present. Quartz vein with eye shape structure (Fig. 4.8).

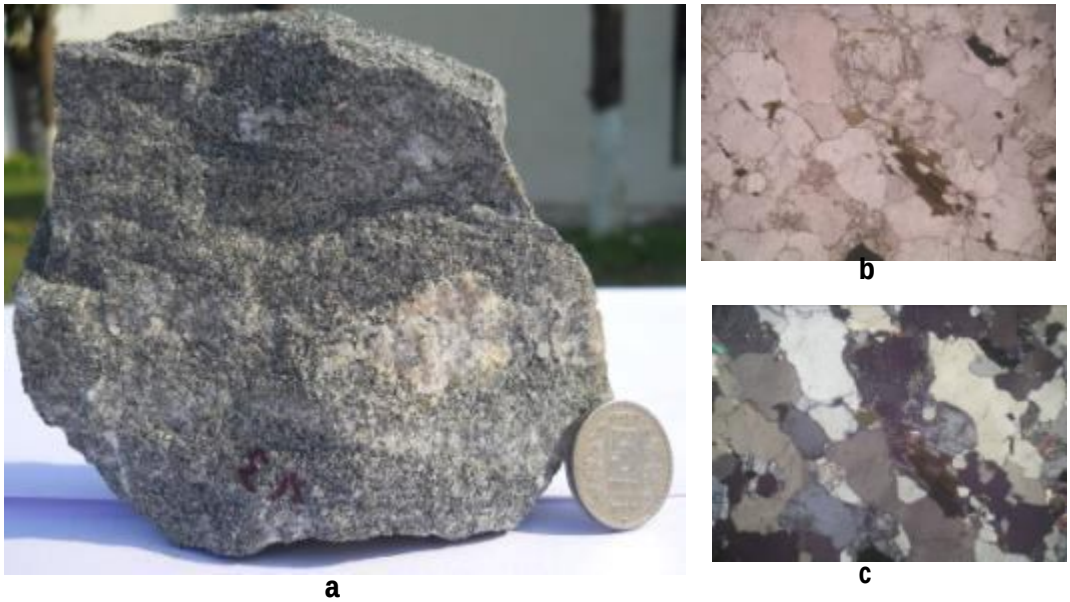

Fig. 4.8: Sample 7 a) Hand specimen b) Thin section 40x ppl c) Thin section 40x c

Sample 8

Sample collected from the banks of lake at Kushwali ki Dhani near Mavanda Tarla at latitude longitude 27° 49.438′N, 75° 46.984′E. Fine to medium grained rock, dark grey in colour. Granite with large content of mica, especially biotite. Typical granitic texture and some gneissic structure seen. Dominent minerals include anhedral quartz, albitic plagioclase and microcline (Fig. 4.9).

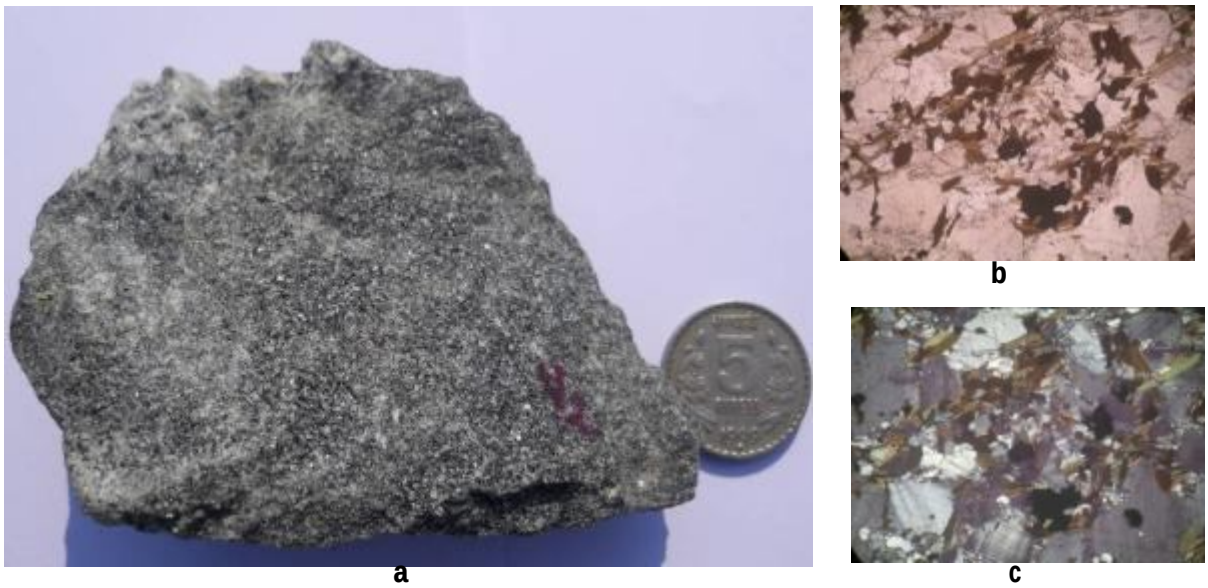

Fig. 4.9: Sample 8 a) Hand specimen b) Thin section 40x ppl c) Thin section 40x c

Sample 9

Sample collected from the banks of lake at Kushwali ki Dhani near Mavanda Tarla at latitude longitude 27° 49.487′N, 75° 46.710′E. Medium to coarse grained Massive igneous rock, pink in colour . Felspathic Quartzite. Dominant plagio clase with ferro magnesium mineral and yellow colour clayey materials, some dark red spots. Well developed crystals of ferro magnesium, narrow veins filled with pink material (Fig. 4.10).

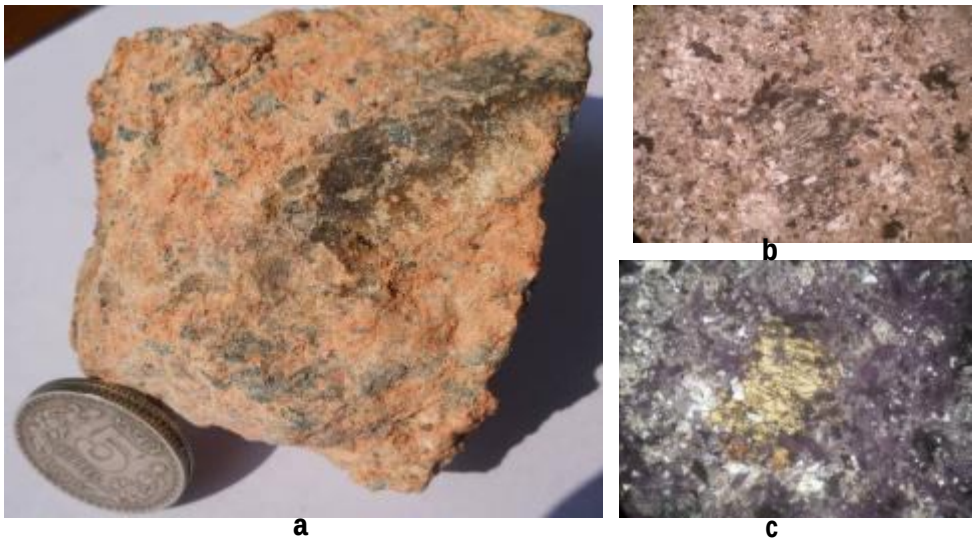

Fig. 4.10: Sample 9 a) Hand specimen b) Thin section 40x ppl c) Thin section 40x c

Sample11

Sample collected at 5 km from Mewara Gujarwas at latitude longitude 28° 2.252′N, 75° 56.872′E. Massive igneous rock, dark grey in colour, fine grained, weathered (Fig. 4.11). Ferromagnesian with large quantity of epidote, opaques, quartz and feldspar (mainly plagioclase and orthoclase).

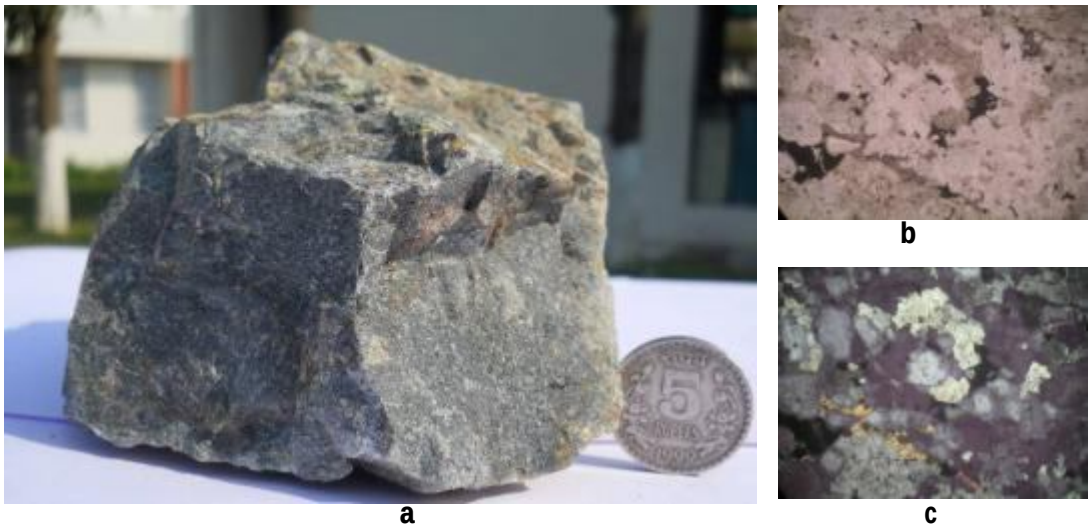

a b c

Fig. 4.11: Sample 11 a) Hand specimen b) Thin section 40x ppl c) Thin section 40x c

Sample12

Sample collected at location 5 km from Mewara Gujarwas at latitude longitude 28° 2.252′N, 75° 56.872′E. Fe ore, Massive sample, high opacity, gravity, fine to medium grained, Brownish black colour (Fig. 4.12).

a b

Fig. 4.12: Sample 12 a) Hand specimen b) Thin section 40x ppl

Sample13

Sample collected at location 4.2 km from Mewara Gujarwas at latitude longitude 28° 1.768′N, 75° 57.069′E. Fine to medium grained, pink colored massive igneous rock. Quartzite with feldspar grains. Grains are crushed. Might be because of the proximity to shear zone. Undulose extinction of quartz seen. Evidences of some water action also found (Fig. 4.13).

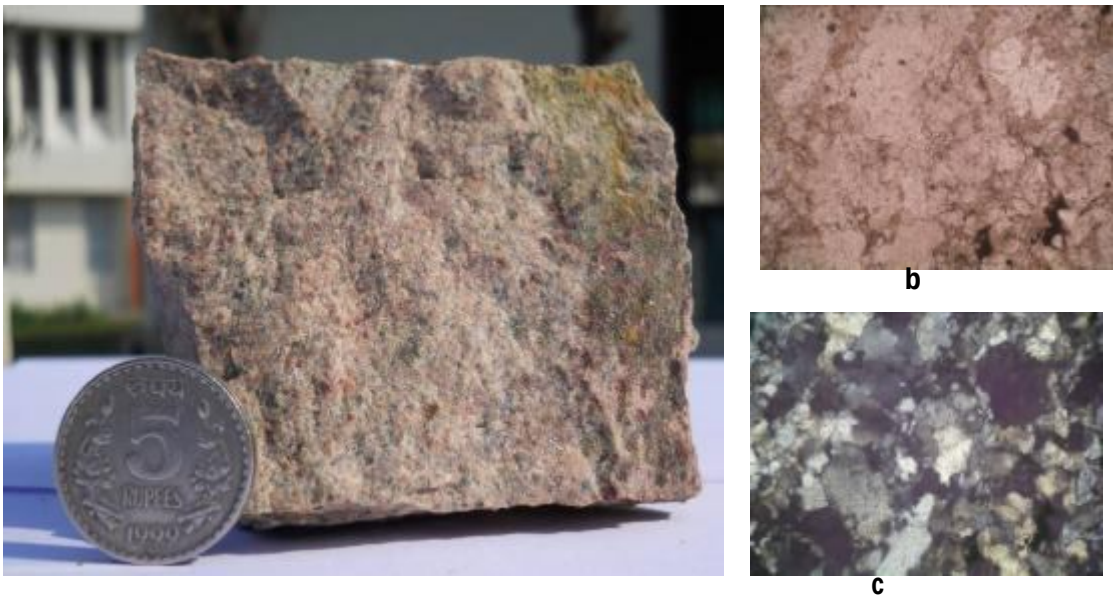

Fig. 4.13: Sample 13 a) Hand specimen b) Thin section 40x ppl c) Thin section 40x c

Sample14

Sample collected at location 4.0 km from Mewara Gujarwas at latitude longitude 28° 1.130′N, 75° 56.915′E. Very fine grained, light pink colored massive rock. Fine grained quartzite. Chlorite rich. Arenaceous grains mixed. Feldspar detretial grains. Might be from the late stage of albitization (Fig. 4.14).

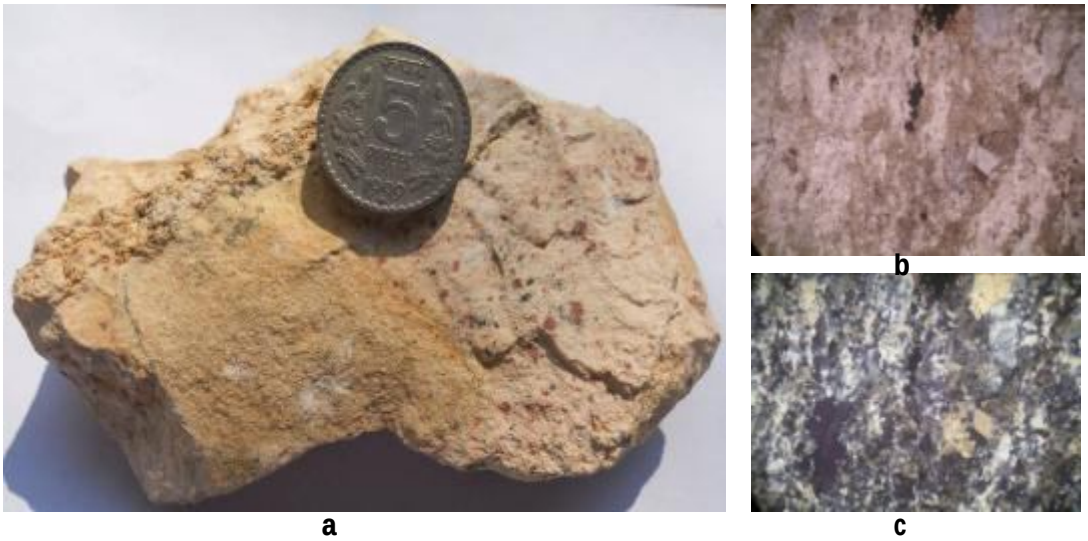

Fig. 4.14: Sample 14 a) Hand specimen b) Thin section 40x ppl c) Thin section 40x c

Sample 15

Collected near Jatuwas at latitude longitude 28° 1.084′N, 75° 56.893′E. Partially albitized quartzo feldspathic rock. Main minerals include plagioclase, quartz, mica and opaques. It has two parts: fine grained and coarse grained. Grain boundary cemented with material (Fig. 4.15).

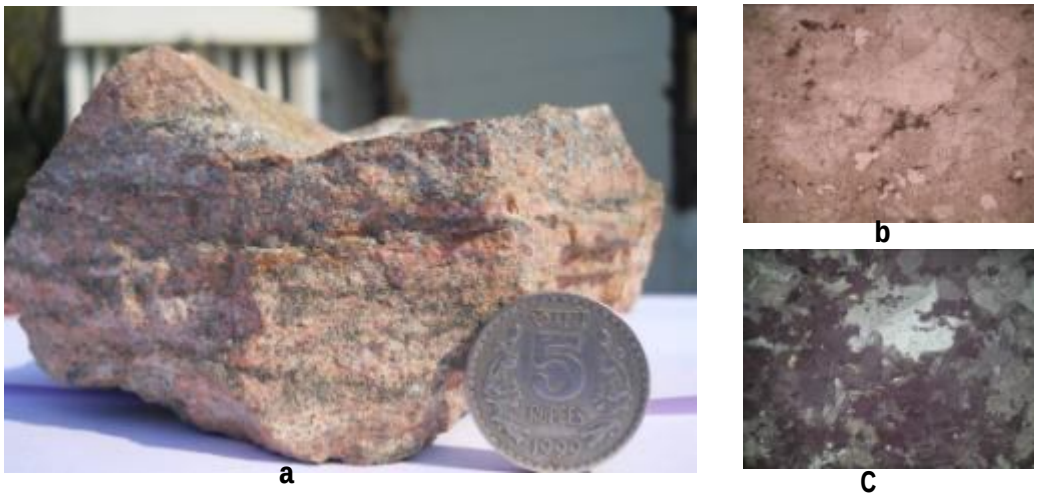

Fig. 4.15: Sample 15 a) Hand specimen b) Thin section 40x ppl c) Thin section 40x c

Sample 16

Sample collected near Mewara Gujarwas at latitude longitude 28° 0.529′N, 75° 55.423′E. Medium to coarse grained massive igneous rock. Calcium silicate with carbonate vein. Some amphibole and scapolite also visible. Some feldspar (orthoclase) also seen (Fig. 4.16).

a b

Fig. 4.16: Sample 16 a) Hand specimen b) Thin section 40x ppl

Sample 17

Sample collected near Mewara Gujarwas at latitude longitude 28° 0.529′N, 75° 55.423′E. Calcite, amphibole and some epidote seen (Fig. 4.17).

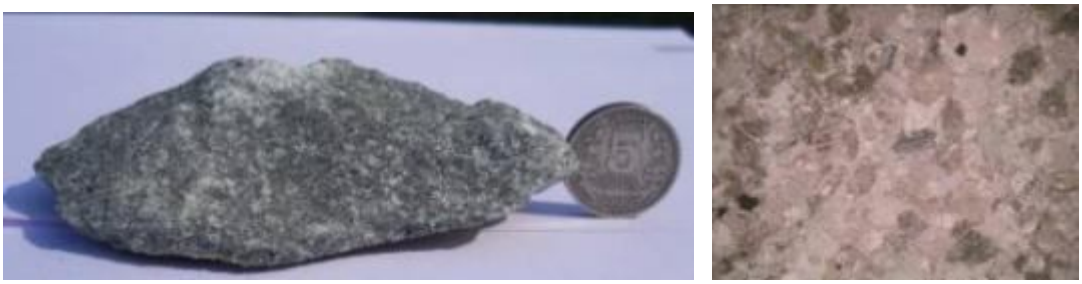

a b

Fig. 4.17: Sample 17 a) Hand specimen b) Thin section 40x ppl

Sample 18 and 19

Sample collected near Mewara Gujarwas at latitude longitude 28° 0.358′N, 75° 55.634′E. Coarse Grained massive igneous rock, colour – pink and white, black. Minerology- quartz, albite, K feldspar, mica, amphibole, opaques. Partially weathered, weathering has affected felspar. Narrow quartz vein present (Fig. 4.18).

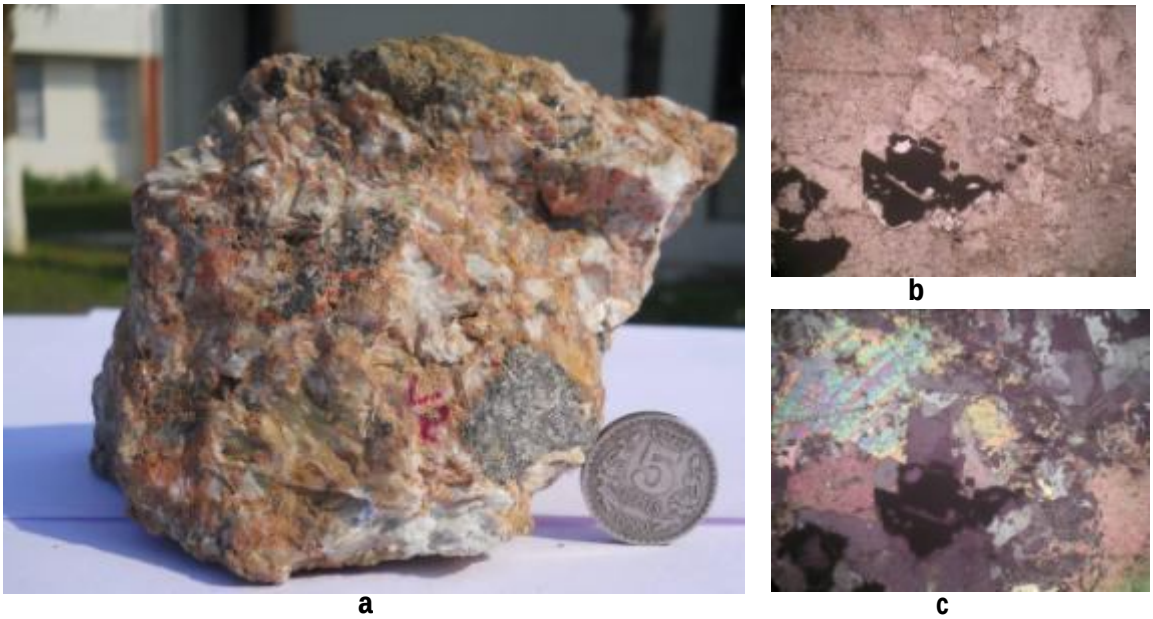

Fig. 4.18: Sample 18 & 19 a) Hand specimen b) Thin section 40x ppl c) Thin section 40x c

Sample 20

Sample collected near Mewara Gurjawas at latitude longitude 28° 0.007′N, 75° 55.244′E. Fine to medium grained massive igneous rock. Colour – brownish black. Minerals – Fe ore, with some quartz. Banding between Fe ore and quartz. May be banded magnetite quartzite. Quartz and Fe ore content varying in bands. Some pores are also seen (Fig. 4.19).

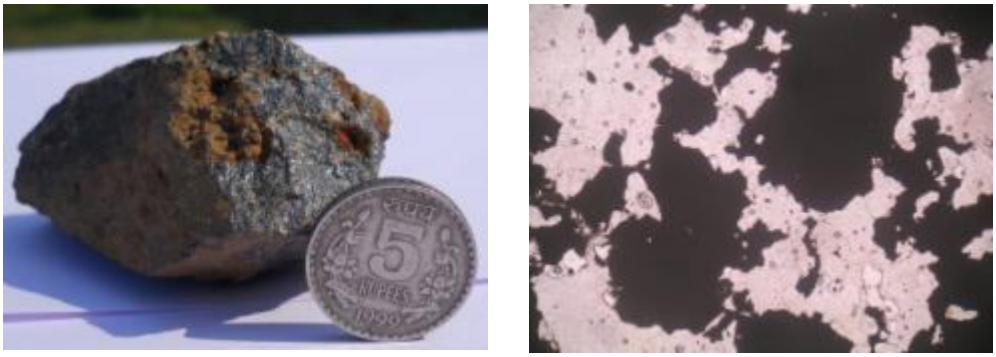

Fig. 4.19: Sample 20 a) Hand specimen b) Thin section 40x ppl

Sample 21

Sample collected near Mewara Gurjawas at latitude longitude 27° 58.842′N, 75° 55.626′E. Coarse grained massive igneous rock, colour – pink and white. Minerology- felspar and quartz, some mica. Purely albitite. Original rock was granitic and after alteration changed into albitite. Partially weathered, after weathering felspar changed to clay (Fig. 4.20).

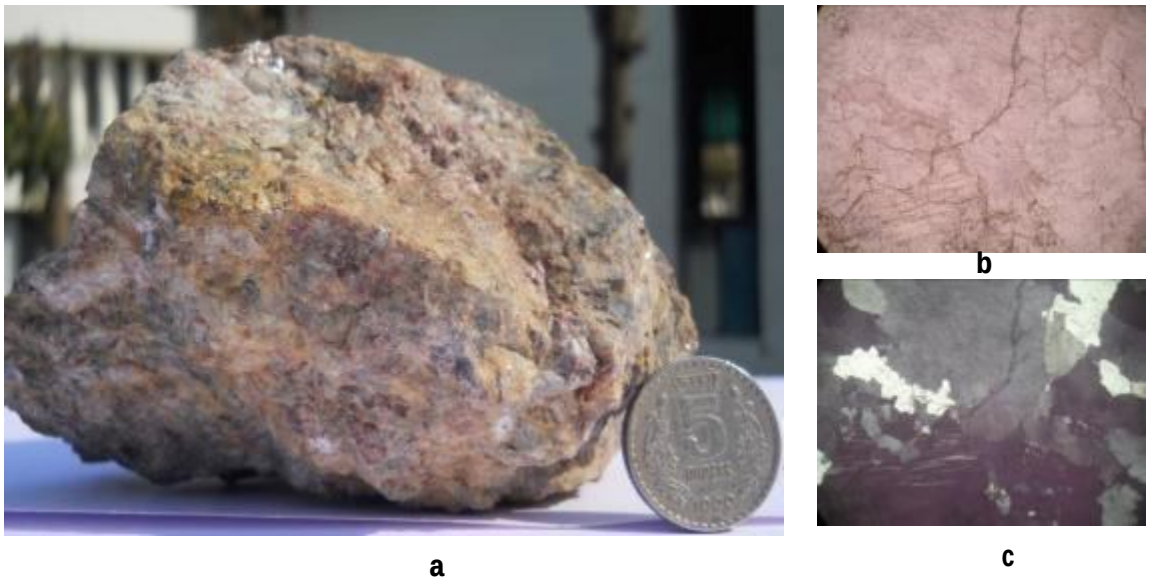

Fig. 4.20: Sample 21 a) Hand specimen b) Thin section 40x ppl c) Thin section 40x c

Sample 22

Sample collected near Mewara Gurjawas at latitude longitude 27° 58.874′N, 75° 55.546′E. Coarse grained massive igneous rock, colour – pinkish white. Minerology- alkali felspar and quartz with some red patches. Albitite is prominent. Appears cloudy but fresh after crossing (Fig. 4.21).

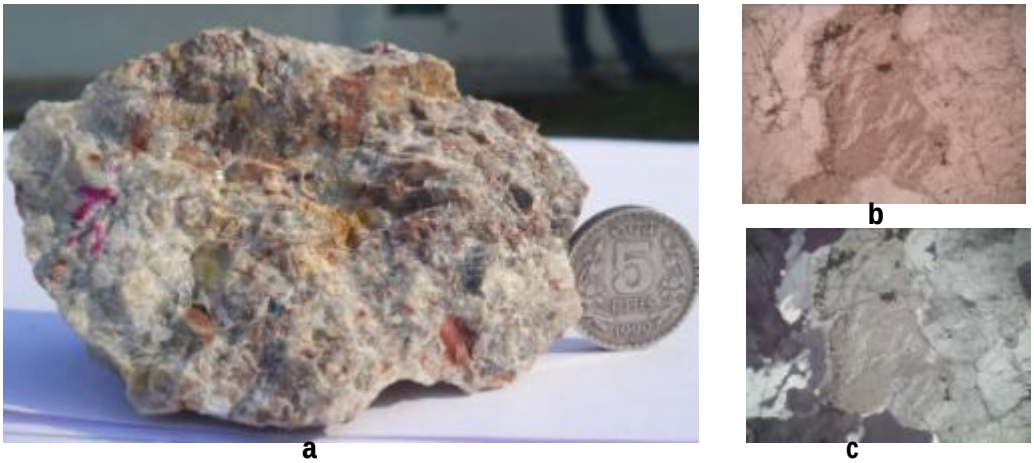

Fig. 4.21: Sample 22 a) Hand specimen b) Thin section 40x ppl c) Thin section 40x

Sample 23

Sample collected near Mewara Gurjawas at latitude longitude 27° 58.872′N, 75° 55.525′E. Coarse grained massive igneous rock, colour – yellowish white. Minerology- alkali felspar and quartz. Some K feldspar also seen. Borderline between granite and pegmatite (Fig. 4.22).

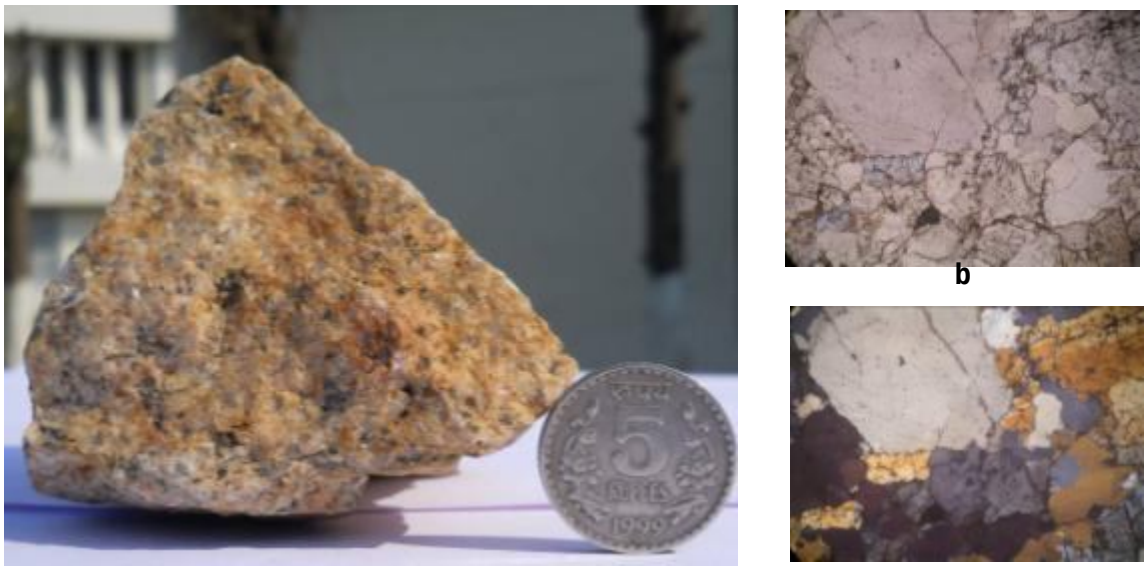

Fig. 4.22: Sample 23 a) Hand specimen b) Thin section 40x ppl c) Thin section 40x c

4.4 FIELD SPECTRA COLLECTION

The validation of the reflectance spectra plays a very important role in this study. The laboratory spectra of the collected field samples are generated using spectro radiometer FieldSpec Pro. Proper care is taken while spectra collection to ensure similar illumination conditions between the satellite data collection and field spectra collection. To ensure this, the field spectra was collected between 10:00 hrs and 14:00 hrs. The instrument and procedure for collection of field spectra is discussed in succeeding sections.

4.4.1 Instrument

In order to make measurements of surface reflectance of geological samples, FieldSpec-Pro spectroradiometer, is used. It is a handy and portable array-based device consisting of three main parts, viz, spectrometer unit, fiber optic cable and a computer interface. The instrument consists of two radiometers which are integrated together and cover the spectral range from 350 to 2500 nm. It collects the spectra in 2151 bands. The reflectance spectra of the rock samples are collected with 5° full field- of-view (FFOV) so as to ensure the readings from sample only and avoiding the background effect. A laptop connected with the instrument helps in real time viewing of the recorded rock spectra. The spectral range and spectral resolution of the instrument used meet the requirements of the present study on ASTER and Landsat datasets. Table 4.2 shows the characteristics of the instrument used.

Table 4.2 Analytical Spectral Device FieldSpec-FR specifications (source: FieldSpec Pro User Guide)

Spectral Range	350 - 2500 nm
Spectral Resolution	Full Width at Half Maximum(FWHM) 3 nm for 350-1000 nm FWHM 10 nm for 1400 -2100 nm
Sampling Interval	1.4 nm for 350 - 1050 nm 2 nm for 1000 - 2500 nm
Scanning Time	100 milliseconds

4.4.2 Instrument calibration

During collection of reflectance spectra using spectroradiometer, thermal electrons within the instrument generate some amount of electrical current, which gets added to the incoming reflected energy. This anomaly needs to be quantified and corrected for proper spectra collection. The process of correction of the error is known as 'Dark Current Correction'. Prior to spectral data collection the instrument should be calibrated using a reference panel. This reference panel is also called as 'White reference or Spectralon'. This white reference provided with the instrument allows the user to check the performance of the instrument. White reference collection also includes dark current correction and is carried out every 15 minutes during the collection of rock sample spectra. This ensures minimizing the effect of the changing lighting conditions on the recorded spectra.

4.4.3 Creation of ASD spectral library

To have a proper correlation between the ground measured spectra collected from spectroradiometer and image spectra from the atmospherically corrected ASTER image, the ground collected spectra ae re-sampled to match the approximate spectral bandwidth and signal-to-noise ratio of ASTER. Several measurements are taken per sample in order to have full information about minerals present. A spectral library of resampled ASD spectra is created. These spectra are used as reference spectra for further classification. Fig. 4.23 (a & b) shows the spectra collected using FeildSpec Pro. The spectra is resampled to ASTER wavelengths for further processing. Fig. 4.24 (a & b) represents the resampled spectral library.

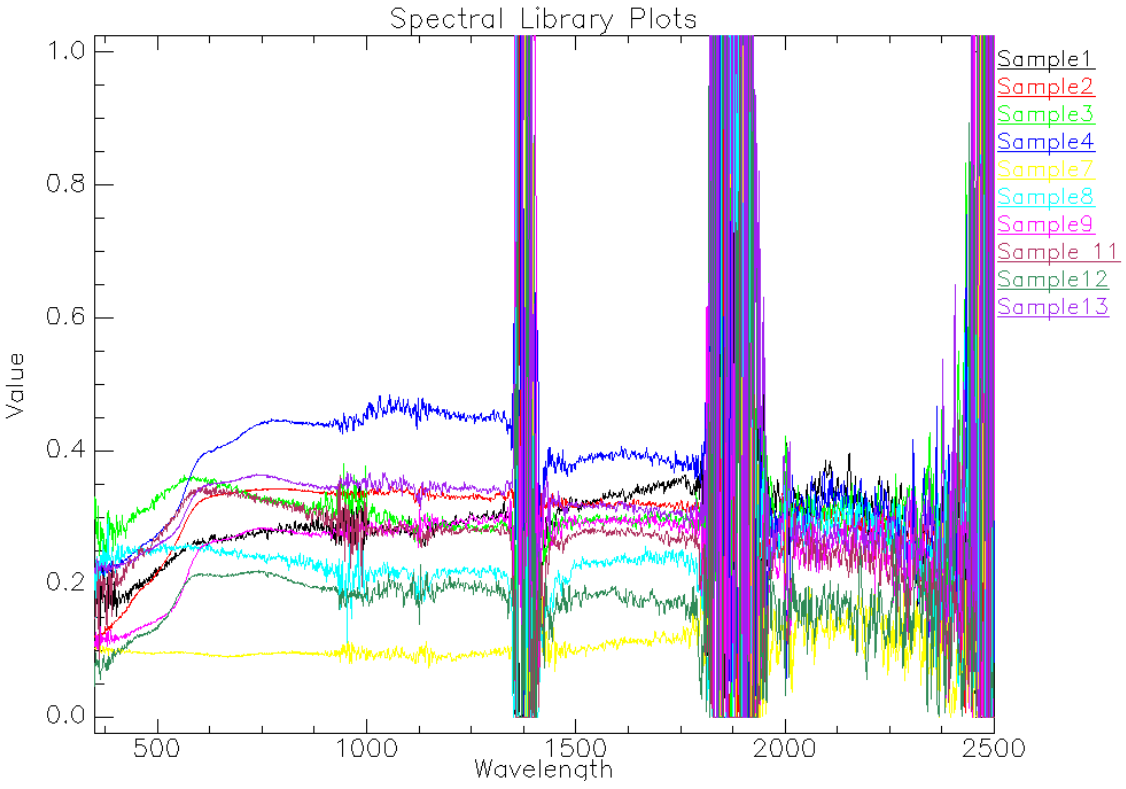

a

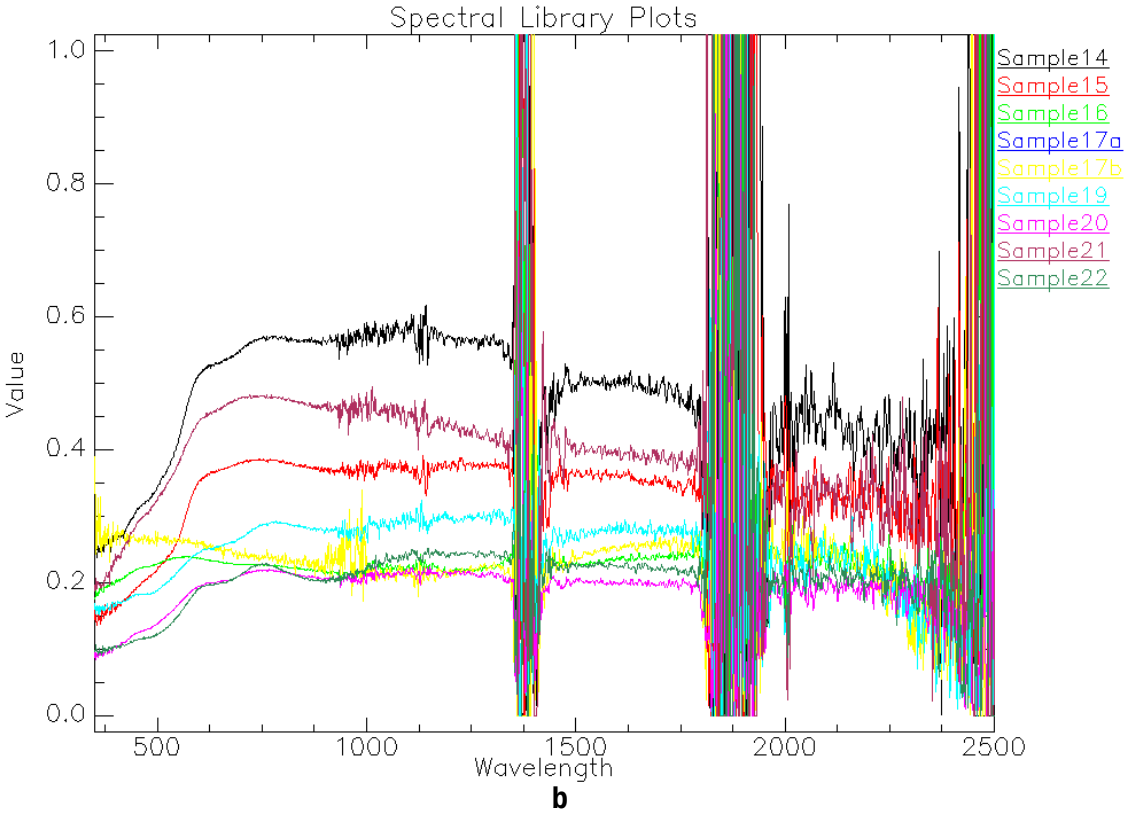

b

Fig. 4.23 a & b: Lab Spectra from ASD FieldSpec-Pro spectroradiometer

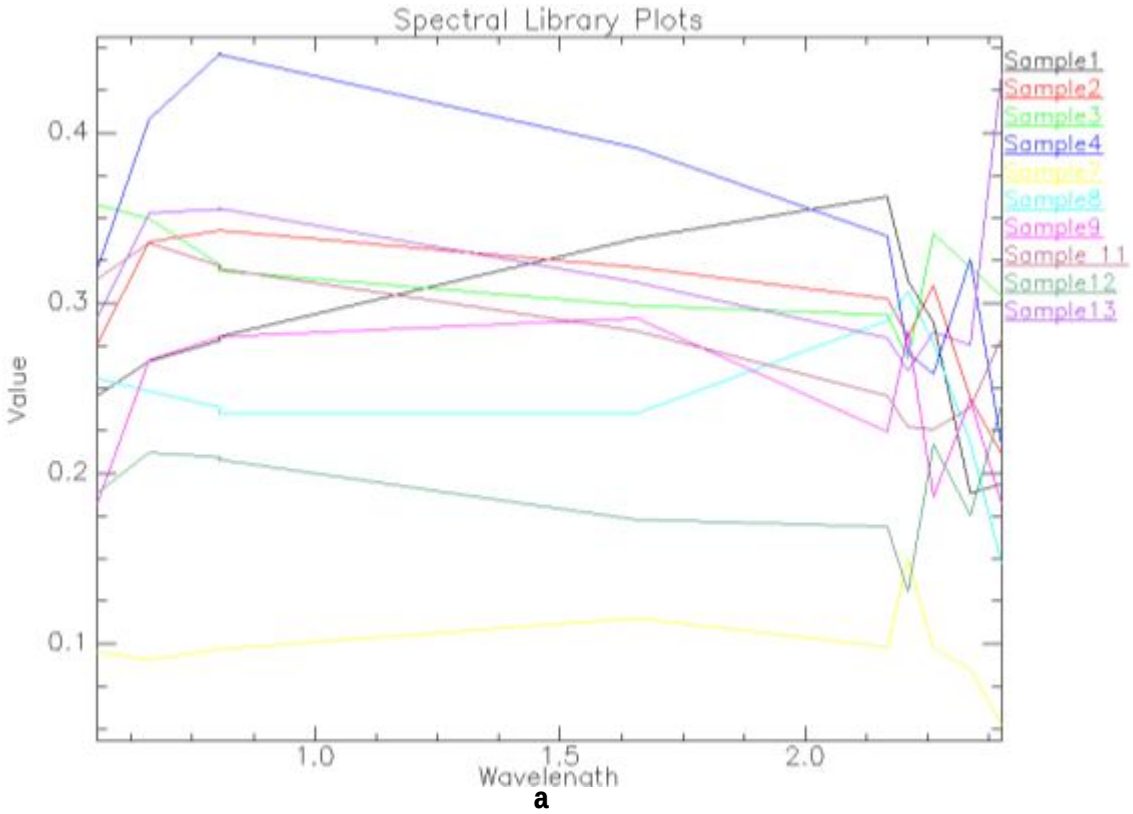

a

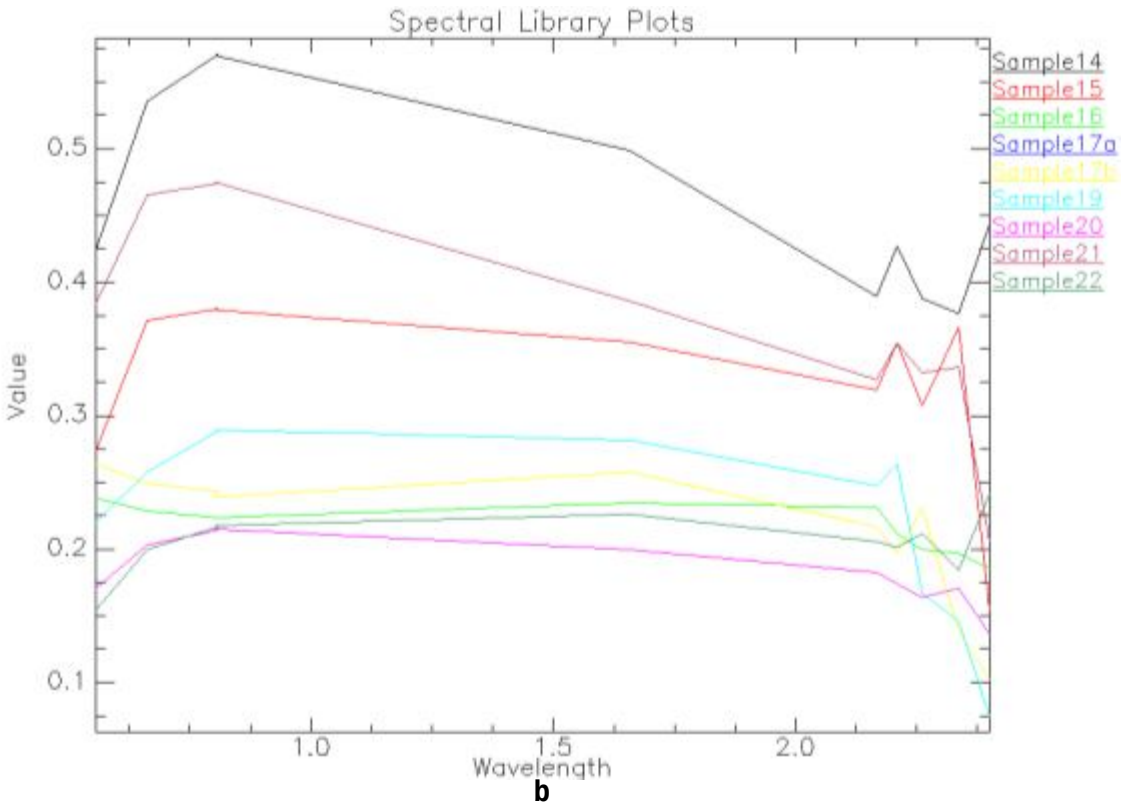

b

Fig. 4.24 a & b: Resample Lab Spectra according to ASTER data

CHAPTER 5

PREPROCESSING OF DATA

For remote sensing observations the electromagnetic radiation (EMR) has to pass twice through the atmosphere prior to being collected and recorded by the instrument. Hence, data observed at the sensor is the combined effect of atmosphere as well as the surface features. Thus removal of effects created by the atmosphere and the topography on the reflected or emitted energy being recorded by the remote sensor becomes one of the main challenges in the use of satellite remote sensing so that the surface physical parameters can be retrieved accurately. On its two-way journey through the atmosphere, the energy received at the sensor is affected by atmosphere, which severely affects the physical interpretability of the remote sensing image. The atmosphere affects mainly by scattering and absorption. Also variation in topography leads to directional effects on the reflected and emitted radiation and also introduces terrain adjacency effects (diffuse irradiance) on the signal reaching the remote sensor, thus changing the true nature of the target radiance. It is crucial to remove these atmospheric and topographic effects from the image data before subjecting the image to further processing, so that meaningful interpretation about the targets of interest can be made from remotely sensed data (Kumar *et al*., 2006).

To compensate for atmospheric effects, the atmospheric parameters of the area should be known. These atmospheric parameters include the amount of water vapor in the area, aerosol optical depth and few other parameters. Since it is very difficult to measure these atmospheric parameters directly, one can have an estimate of these parameters from the radiance image. Then these estimated atmospheric parameters can be used in accurate atmospheric models to model actual surface reflectance. Since for such methods there is an independent measurement of atmospheric properties for each pixel, thus such type of atmospheric corrections can be applied on a pixel-by-pixel basis.

This chapter deals with the atmospheric correction of the ASTER dataset used in this study. Existing techniques of atmospheric correction have been explored and applied to these data and a comparative evaluation has been made to produce the final surface

reflectance and surface emissivity image data, to be used in further detailed image analysis.

5.1 ATMOSPHERIC CORRECTION

Atmospheric correction is an important preprocessing step required before the remote sensing image can be utilized for further application. Most of the remote sensing analyses require that the digital number (DN) values in remote sensing data be converted into percentage reflectance so as to make them comparable to the on-ground or in-laboratory reflectance values collected (Teillet and Fedosejevs, 1995). In cases where surface material has sufficiently different reflectance and the atmospheric effects do not hamper their spectral discrimination, the further analysis can be carried out on uncorrected data. However, for utilizing remotely sensed data in mineral identification, atmospheric effects need to be compensated.

5.1.1 Background and Methods

Radiation from the Earth's surface interacts with the atmosphere before it is recorded by the satellite sensor. For analyzing the remotely sensed data, the effects of the atmosphere on the radiances should be understood in detail. Composition of atmospheric constituents is not constant spatially and temporally, thus effect of atmosphere also varies accordingly. The atmosphere alters the incoming radiation either by scattering or absorption. The effect of scattering and absorption is dependent on the wavelength used. Absorption occurs when a part of the EMR passing through the atmosphere is absorbed by the atmospheric constituents. This energy can be later on reemitted at different wavelengths (Kumar *et al*., 2006). Scattering occurs when the direction of the energy passing through the atmosphere gets changed because of the diffusion of radiation by small particles present in the atmosphere. Scattering could be of various types depending on the relative size of the scattering particle and the wavelength of the incoming energy. At the shorter wavelengths, scattering due to clouds and other atmospheric constituents is the main source of attenuation while the longer wavelengths are mainly absorbed by ozone and water vapour particles of the atmosphere. Thus for shorter wavelengths absorption can be ignored and for longer wavelengths scattering effects would be

negligible (Liang *et al.*, 1997). The main effects of the atmospheric scattering on remotely sensed data are upwelling atmospheric radiance or path radiance (Slater, 1980). Infrared bands are mainly affected by scattering from air molecules and aerosol particles. This has an additive effect on the measured radiance and result in image haze. Usually the amount of atmospheric gases like carbon dioxide, methane etc. does not vary much over time, however the amount of water vapour varies consistently both spatially and temporally. The air molecules remain consistent in their properties and follow Rayleigh's scattering rule, while the aerosols are quite variable and rather unpredictable. An effective atmospheric correction algorithm is expected to model the influences caused by scattering and absorption due to atmospheric constituents.

The atmospheric correction of remote sensing data is quite complicated and difficult because of non availability of precise inputs required for simulation by atmospheric models. The atmosphere alters the incoming reflected or emitted radiation by reducing the original energy and also by contributing its own energy. For remotely sensed images covering large water bodies, the atmospheric radiation make up over 90% of the satellite recorded energy. Though our study area does not include large water body, still proper atmospheric correction needs to be carried out since even smaller effects of the atmosphere would degrade the quantitative use of remotely sensed data. Thus accurate correction of atmospheric effects is essential for further analysis (Schott *et al.*, 1988).

Atmospheric calibration methods can be grouped into two different groups, namely, the *absolute radiometric correction* and *relative correction method*. Relative atmospheric correction methods normalize the radiation variations within an image and between images of same area collected on different dates. There are many methods for relative correction such as dark-pixel subtraction, Log Residual, Internal average relative reflectance etc.

The absolute correction method removes the effect of atmospheric attenuation, topography and solar conditions and thus converts the digital number of the remotely sensed data into surface reflectance (Song *et al.*, 2001). These methods are essential if one needs to establish relationship between image based measurements and ground based measurements and also if one wants to focus on the extraction of subtle differences in

reflectance to estimate spectral properties of the material. Common atmospheric correction programs are 6S (Second Simulation of the Satellite Signal in the Solar Spectrum), MODTRAN (Moderate Resolution Atmospheric Radiance and Transmittance Model), LOWTRAN etc.

5. 2 ATMOSPHERIC CORRECTION OF ASTER L1B DATA

ASTER L1B data was procured for the study area. The atmospheric correction aims at finding out a relationship between the top-of-atmosphere (TOA) radiance and surface radiance/reflectance based on the scattering and absorption characteristics of the atmosphere. Once this relationship is established, it can be used to convert the at-sensor radiance values to on-ground reflectance values.

"Crosstalk" or energy "overspill" is a phenomenon encountered in ASTER data which affects the DN values recorded at the sensor. Energy from ASTER band 4 "leaks" and affects the energy being recorded in other bands, most commonly bands 5 and 9 (Fig. 5.1). According to ASTER mineral index processing manual, the problem occurs because the solar output of the band 4 is considerably higher than any other SWIR bands. Thus if there is a small leakage of photons of band 4, they can affect largely on the other bands. Bands 5 and 9 suffer most and the effect is largest since physically the detectors of these bands are close to band 4 detector (Tonooka and Palluconi, 2002). Though there are software packages that provide corrections for this phenomenon, these packages operate on a scene or sub scene average whereas the problem is proportional to albedo contrast across pixels in adjacent lines and needs to be addressed on a line-by-line, pixel-by-pixel basis.

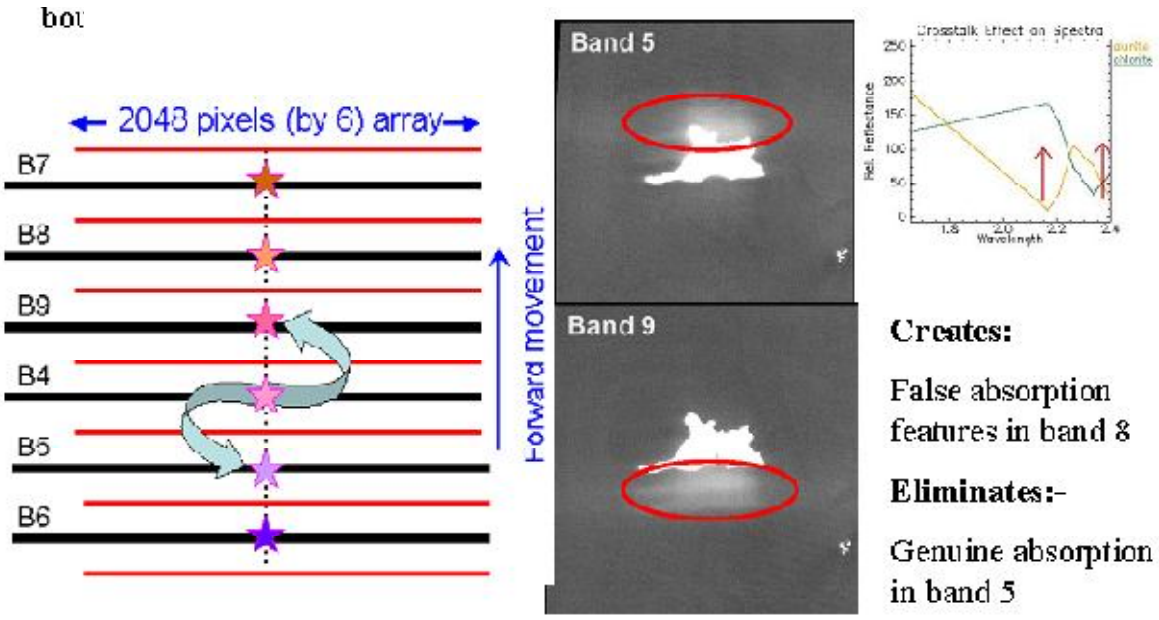

Fig. 5.1: Schematic representation of crosstalk in ASTER SWIR bands (Tonooka and Palluconi, 2002)

If uncorrected, the cross-talk problem can create artificial absorption in bands 6 and 8 that may lead to the false mapping of AlOH hydroxyl minerals such as kaolinite and illite (band 6) and chlorite, epidote or calcite. In some cases this can create an artificial low in bands 5 and 9, creating false argillic (alunite, pyrophyllite) and probably might lose identification of propylitic and carbonate mineral. On the contrary, if the problem is overcorrected it would result in creating artificial absorptions in bands 5 and 8, generating false argillic and carbonate/propylitic mineral zones respectively. For this reason, the data is left uncorrected and the mineral zones as mapped are interpreted with the crosstalk in mind.

The primary LIB data has been put to rigorous radiometric, atmospheric and topographic corrections by applying existing methods and used.

5.2.1 Atmospheric correction of ASTER VNIR-SWIR data and reflectance retrieval

In the following sections, the atmospheric correction and calibration of ASTER VNIR-SWIR data using available atmospheric correction techniques are explained. The corrections are carried out to obtain the final surface reflectance image data. Both relative and absolute atmospheric correction methods have been applied on the dataset and analyzed. The results of different methods of atmospheric correction have been evaluated based on reflectance spectrum of a common pixel in all the outputs, referred to as the test pixel spectrum. The reference spectrum pixel represents a homogeneous area, representing urban settlement. Spectral reflectance curve from Johns Hopkins University (JHU) spectral library available in ENVI has been taken as reference spectrum. The reference spectrum has been resampled to ASTER wavelength for comparison. ENVI and ERDAS software packages have been used conjunctively for atmospheric correction of the image data.

5.2.2 Methods of relative atmospheric correction

i. Relative reflectance using Log Residuals

Log Residuals calibration is applied on the radiance data to correct for atmospheric transmittance, instrument gain, solar irradiance, topographic effect, and albedo effects (Green and Craig, 1985). This transform results in a pseudo reflectance image which can further be used for detecting absorption features for specific minerals. The logarithmic residual of the dataset is calculated by dividing the input spectrum by the spectral and spatial geometric mean. The spectral mean is the mean value for each pixel in all the bands. It is used to remove topographic effects. The spatial mean is the mean of all pixels for each band and helps in removing solar irradiance and atmospheric transmittance. Fig. 5.2a shows the Log Residuals-corrected image and 5.2 b shows spectrum of the test pixel with reference spectrum.

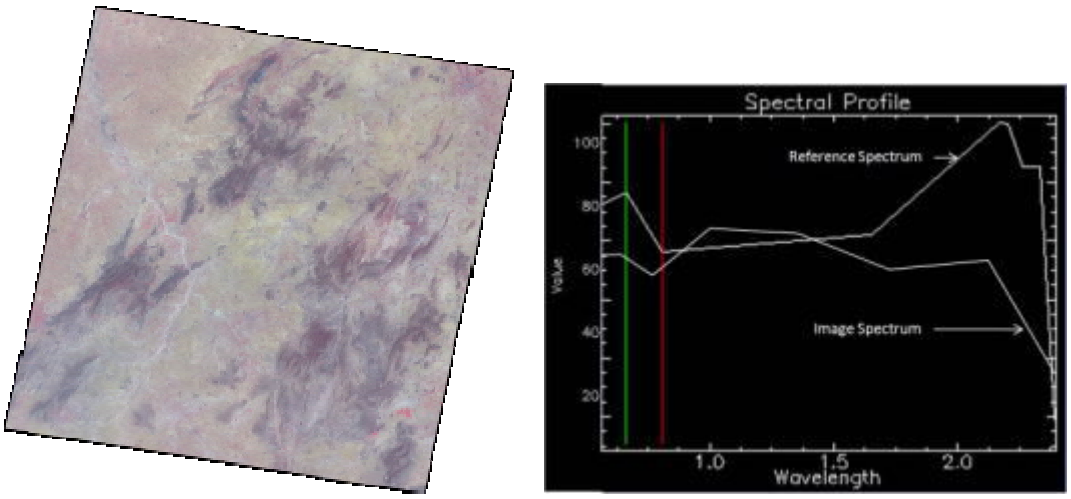

a b

Fig. 5.2: Log Residual Correction a) Corrected image b) Image spectra Vs Reference spectra

ii. Relative reflectance using IARR method

In areas where there are no ground measurements and scene details are also not known, the radiance values can be reduced to relative reflectance by normalizing to a scene average spectrum. This happens in Internal Average Relative Reflectance (IARR) calibration method (Green and Craig, 1985). This method is particularly effective for arid areas with no vegetation, and hence is suitable for the data used in this study. The entire scene is used to calculate an average spectrum which can be used as the reference spectrum. This is now divided into the spectrum for individual image pixel. Fig. 5.3 shows the IARR-corrected relative reflectance spectrum of the test pixel.

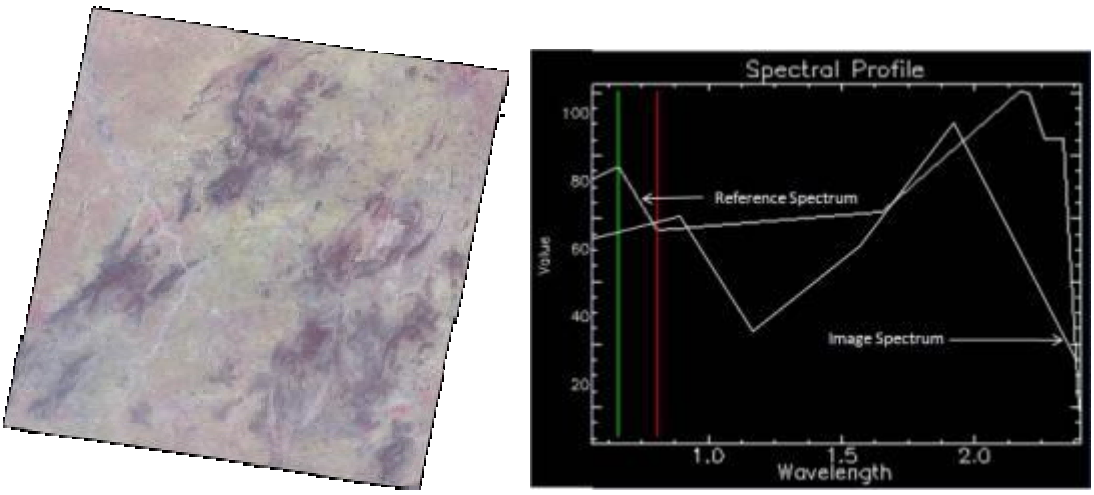

a b

Fig. 5.3: IARR Correction a) Corrected image b) Image spectra Vs Reference spectra

iii. Relative reflectance using the Flat Field and the Modified Flat Field techniques

The Flat Field (FF) calibration method is used to normalize the input data to the spectrum of a known spectrally neutral flat field in the scene. The FF selected is usually a spectrally uniform and bland site within the scene (Clark *et al.*, 2002). The Modified Flat Field (MFF) method (Green, 1990), implemented in ERDAS Imagine software, requires that the analyst knows the material of the flat field and has a laboratory spectrum of that material. In MFF, each input pixel spectrum is divided by the flat field and then multiplied by the spectrum. For the study area, 13 pixels representing spectrally and spatially homogeneous area are used as a flat field. JHU library spectrum of this material available in the ASTER spectral library was used with the MFF procedure to calibrate the data to relative reflectance. The results of MFF calibration for the test pixel have been shown in Fig. 5.4 a and b.

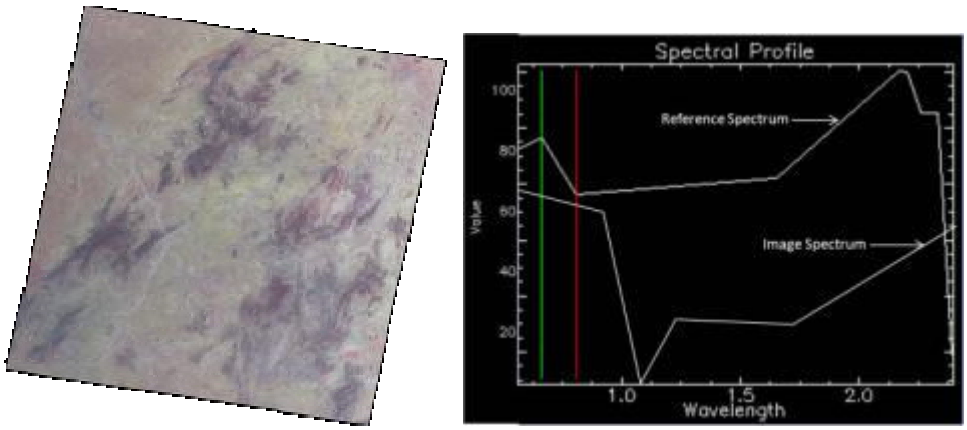

a b

Fig. 5.4: Modified Flat Field Correction a) Corrected image b) Image spectra Vs Reference spectra

5.2.3 Methods of absolute atmospheric correction

i) *Surface reflectance retrieval using FLAASH*

FLAASH is an atmospheric calibration method based on radiative transfer model and is developed by Spectral Sciences, Inc. It uses an updated MODTRAN-based radiation transfer model and also includes corrections for adjacency effect.

FLAASH differs from other radiative transfer models in using a better version of MODTRAN which has an updated recent spectral database. To retrieve visibility, the algorithm uses a ratio based reflectance method. It supports off-nadir geometries and all MODTRAN aerosol types and does all the MODTRAN calculations on-the-fly. It also compensates for the adjacency effect and does the wavelength calibration automatically. The results from FLAASH and other radiative transfer model tend to be similar in dry, clear atmospheres but significantly differ under moist and hazy conditions.

Description of FLAASH parameters used

Sensor type: The option of selecting sensor type is provided to the user for wide range of sensors. Sensor type, for the present study is selected as ASTER.

Pixel size: In the Pixel Size (m) field 15.0 is entered as the VNIR bands used in the study has 15 m spatial resolution.

Ground elevation: Ground elevation input required by FLAASH is an average elevation of the imaged terrain. For Khetri, the average elevation of the imaged terrain is taken as 0.6 km above MSL.

Solar zenith angle/ Flight date and time: Solar zenith angle at the time of the satellite pass is provided in the product description. For Khetri the solar zenith angle is 37.214824 degrees. Flight date and time are selected as per the data description of ASTER. The data is captured on October 5, 2002.

Scene centre latitude and longitude: The scene centre latitude and longitude is provided in the header file of the dataset. These have been provided as input in the software.

Visibility: The visibility selected for Khetri is inferred as "clear" in the range of 40 km.

Atmospheric model: The user has to make a choice, based on the geographic location of the scene to atmospherically correct the image. FLAASH supports six atmosphere types based on a seasonal-latitude surface temperature MODTRAN modelled atmospheres as given in Table 5.1.

Table 5.1 Column water vapor amounts and surface temperatures for the MODTRAN model atmospheres (source: FLAASH user guide)

Model Atmosphere	Water vapour (std atm-cm)	Water vapour (g/cm^2)	Surface air temperature
Sub Arctic Winter (SAW)	518	0.42	-16° C or 3° F
Mid latitude Winter (MLW)	1060	0.85	-1° C or 30° F

U.S. Standard (U.S.)	1762	1.42	15° C or 59° F
Sub Arctic Summer (SAS)	2589	2.08	14° C or 57° F
Mid Latitude Summer(MLS)	3636	2.92	21° C or 70° F
Tropical (T)	5119	4.11	27° C or 80° F

Modtran model atmosphere is selected based on the latitude of the area and also season of the image acquisition. Based on the location of Khetri 27º 55' N latitude for an October scene "Tropical" model is selected.

Aerosol model/ atmospheric file: The user has to make a choice, based on the geographic location. Rural is recommended for areas with visibility greater than 40 km. Thus rural model is selected for the area.

Water vapor retrieval: FLAASH includes a method for retrieving the amount of water vapour for each pixel. The wavelength at which water retrieval is to be carried out is selected based on the input band wavelengths. As ASTER VNIR-SWIR has bands in 0.52 – 2.43 μm range, the recommended wavelength of 1.13 μm is used for water retrieval for Khetri dataset.

Adjacency range and zone: In order to accommodate for the adjacency effect, the 'adjacency correction' is toggled to 'yes' in advanced setting parameters of FLAASH. Three multiscatter models are available in FLAASH: Isaacs, Scaled DISORT and DISORT. The recommended Scaled DISORT with 8 streams (signifying 8 directional adjacency) is selected for the present study.

Reflectance scale factor: The output reflectance image needs to be scaled from floating-point into 2-byte integer data space. Thus the recommended scale factor of 10,000 is used as input to FLAASH.

Wavelength calibration: The wavelength calibration is applied as available in FLAASH.

The FLAASH input parameters for the ASTER VNIR-SWIR image data of the study area have been summarized in Table 5.2, 5.3, 5.4 and 5.5. The FLAASH corrected image is shown in Fig. 5.5a and the spectra of reference pixel in Fig. 5.5 b

Table-5.2: ENVI FLAASH input parameters for the ASTER scene used

Parameter		**Value**
General	Scene Center, deg	27.833723 75.750792
	Sensor and Sensor Type	ASTER; Multispectral
	Sensor Altitude (km)	705
	Ground Elevation (km)	0.5 (default 0.0)
	Pixel size (m)	15
	Flight date and time	Oct. 5, 2002; 05:43:51 UTC(Z)
Atmospheric model		Tropical
Aerosol Model		Rural
Water Retrieval		No
Water Column Multiplier		1.000
Aerosol Retrieval		2 Band (K-T)
Initial Visibility (km)		25
Kaufman-Tanre (K-T) Aerosol Retrieval	K-T Upper Channel	Band5 (2.167 µm)
	K-T lower Channel	Band2 (0.661 µm)
	Max. Upper Channel	0.10

	Reflectance	
	Reflectance Ratio	0.45
Advanced settings	Aerosol scale Height (km)	2.00
	CO_2 Mixing Ratio (ppm)	390.00
	Adjacency Correction (Yes/No)	Yes
	MODTRAN Resolution (cm^{-1})	15
	MODTRAN Multiscatter Model	Scaled Disort
	Number of DISORT Streams	8
	Scale Factor for Radiance Image	10.0
	Output Reflectance scale Factor	10000

Table 5.3: Acquisition parameters for the ASTER LIB dataset used

Parameter	Value
Solar direction (azimuth and elevation), deg	153.210649, 54.309521
Solar zenith angle (90° - solar elevation angle), deg	35.690479
Date and time of scene acquisition	Oct. 5, 2002; 05:43;51 UTC(Z)
Julian day for the acquisition date and time	2452552.738785
Earth-sun distance (d), AU	1.0000594926008028

Table 5.4: Solar exo-atmospheric irradiance values for the nine reflective bands of ASTER (VNIR+SWIR) (Thome *et at.*, 2001):

ASTER band (band center in µm)	$E_{SUN}\lambda$ (W/m²/sr/ µm)
AST_1 (0.556)	1847.00
AST_2 (0.661)	1553.00
AST_3 (0.807)	1118.00
AST_4 (1.656)	232.50
AST_5 (2.167)	80.32
AST_6 (2.209)	74.92
AST_7 (2.262)	69.20
AST_8 (2.336)	59.82
AST_9 (2.400)	57.32

Table 5.5: Haze value computation for ASTER VNIR+SWIR bands using the image-based DOS technique COST method (Chavez, 1996)

ASTER Band Number	Minimum scaled Digital Number (DN_{min})	Minimum Band-specific Radiance-at-sensor (L_{min})	Band-specific Solar Irradiance ($E_{SUN}\lambda$)	Radiance for a 1% reflecting surface (Lp=1%) $=(\rho E_{SUN}\lambda \cos\theta z \tau d \tau u)/\pi d^2$	Haze value for each band (L_{haze}) $= L_{min} - L_p = 1\%$
AST_1	53	35.152	1847	3.878358569	31.27364
AST_2	36	24.78	1553	3.261012917	21.51899
AST_3	31	25.86	1118	2.34759333	23.51241
AST_4	36	7.609	232.5	0.488207021	7.120793
AST_5	37	2.5056	80.32	0.168657152	2.336943

AST_6	35	2.125	74.92	0.157318151	1.967682
AST_7	35	2.0298	69.2	0.145307208	1.884493
AST_8	30	1.2093	59.82	0.125610942	1.083689
AST_9	35	1.0812	57.32	0.120361404	0.960839

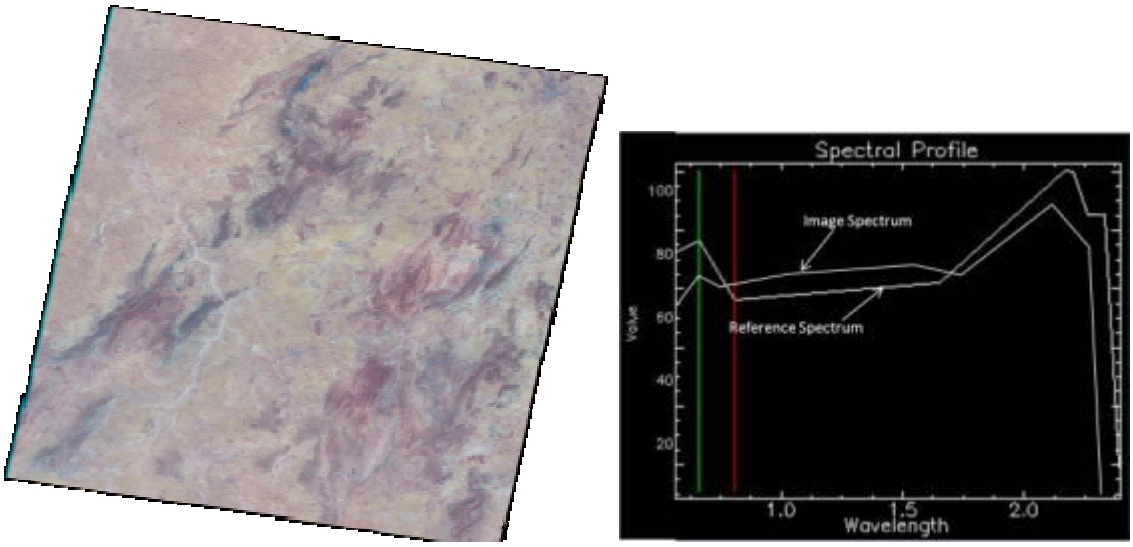

a **b**

Fig. 5.5: FLAASH Correction a) Corrected image b) Image spectra Vs Reference spectra

ii. *Surface reflectance retrieval using ATCOR*

ATCOR software developed by DLR (German Aerospace Center) is useful for processing bands in the EMR region from 0.4 – 2.5 μm. The satellite sensors having a small field-of-view (FOV) have approximately constant solar and view geometry, thus in such cases the atmospheric transmittance and radiance functions can be treated as independent of scan angle. The algorithm houses a large database of atmospheric correction functions valid for a wide range of image acquisition and area conditions. The algorithm has separate codes for flat and rugged terrain. ATCOR-2 mostly used for flat terrain, considers two geometric degrees of freedom (DOF) of the flat plane, where as

ATCOR-3 has three degree of freedom. It takes into consideration terrain height and is useful for mountainous terrain. ATCOR can be used to estimate the atmospheric conditions (water vapor content, aerosol type, visibility) for an image scene. The total signal at the sensor is made up of four parts: radiance reflected from the ground pixel, radiation added from the neighboring area, terrain radiation which gets reflected to the pixel and path radiance. The surface reflectance spectrum of an object in the scene is a function of the object and the atmospheric parameters. Once the atmospheric effects are removed, it can be compared to typical library spectra. The following parameters required by the program (ATCOR-2) are keyed in according to the sensor and study area:

Aerosol type: Aerosol type is selected as rural.

Visibility: The visibility selected for Khetri is inferred as "clear" in the range of 40 km.

Ground elevation: Ground elevation is taken as 0.5 km based on the topomap of the area.

Solar zenith angles: Solar zenith angle is keyed in as 35.69° as given in the header file.

Tilt geometry: Tilt angle is taken as zero.

The corrected image and reflectance spectra is shown in Fig. 5.6.

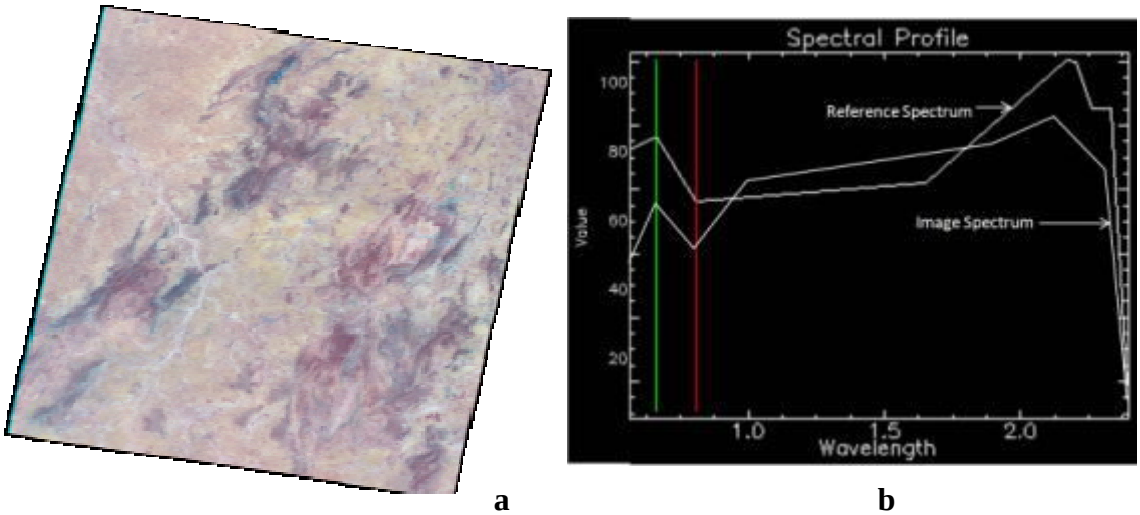

a **b**

Fig. 5.6: ATCOR Correction a) Corrected image b) Image spectra Vs Reference spectra

5.3 ATMOSPHERIC CORRECTION OF ASTER TIR DATA

Like VNIR-SWIR wavelengths, the data in TIR spectral range is also affected by the atmospheric interference. The influence of atmosphere for thermal infrared bands is mainly due to multiplicative absorption, and the effect of atmospheric scattering is quite negligible. Atmospheric water is the main constituent attenuating the radiances in the TIR region. To approximate and remove the atmospheric contributions to the thermal infrared data and to retrieve the reflectance values, ENVI's Thermal Atmospheric Correction tool is applied.

The thermal atmospheric correction algorithm used in ENVI is similar to the In-Scene Atmospheric Compensation (ISAC) algorithm. The algorithm assumes a uniform atmosphere over the entire scene and also assumes that there is a surface with characteristics of perfectly black body within the scene, though the spatial location of blackbody is not required in the algorithm. Also the reflected down welling radiance is not assumed. To start with, the algorithm searches for maximum brightness temperature and determines the wavelength band exhibiting the same. This wavelength which exhibits the maximum brightness temperature is then taken as the reference wavelength. The feature spectra with brightest temperature at this atmospheric component in the radiance is calculated using the spectra that the brightest temperature at this wavelength. For this location, a graph between the reference blackbody radiance and the measured radiance is plotted according to wavelength and a line is fitted for the plotted dataset. The slope and the offset are calculated for this linear regression data and the atmospheric component for the band is calculated. The compensation calculated is then applied to the other bands also. The five thermal bands of ASTER data are subjected to the thermal atmospheric tool in ENVI. Fig. 5.7 shows the corrected image with the corrected spectra.

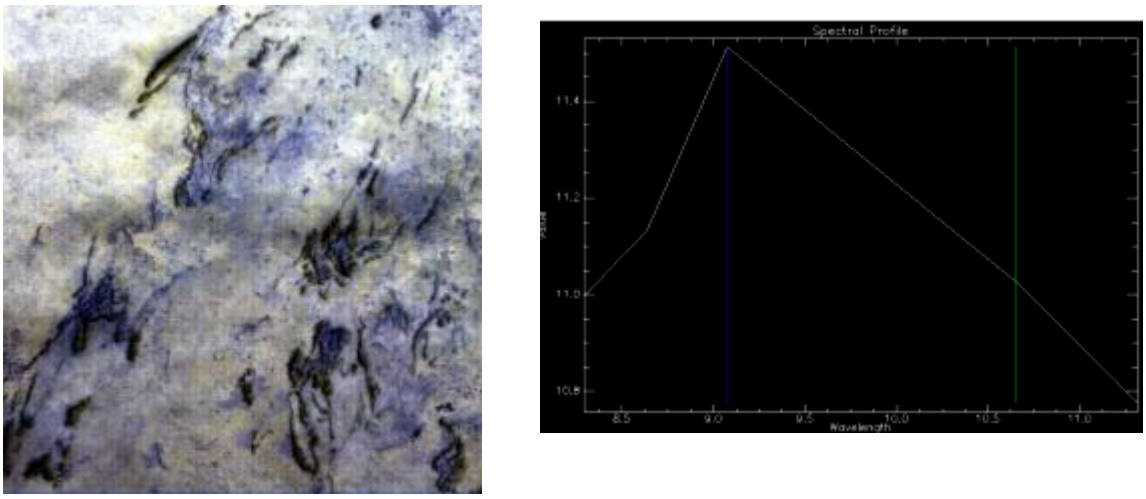

Fig. 5.7: Thermal Atmospheric Correction a) Corrected image b) Corrected Spectra for albitite

5.4: DISCUSSION ON ATMOSPHERIC CORRECTION RESULTS

Atmospheric corrections can be applied by using relative and absolute physical methods. The relative methods are computationally fast since they avoid the evaluation of atmospheric components. These methods derive the input information from the image itself. But these methods only result in a statistical normalization of the image. The atmospheric correction methods based on atmospheric physics use the sun-sensor geometry, atmospheric parameters and elevation information to remove the contribution of atmospheric constituents for the image. The technique converts the DN to at sensor radiance using sensor gain and offset values. The sensor radiance values are then converted to top-of-atmosphere reflectance and ultimately to reflectance at surface of earth utilizing parameters like solar elevation, sun azimuth, Julian day. Physics based ATCOR and FLAASH both use MODTRAN4 radiative transfer code. The radiative transfer algoritms simulate the reflectance image by taking into account sun-sensor geometry at the time of imaging, temperature, water vapour and gases concentration profiles, aerosol type and concentration, spectral variation of ground reflectance and availability of bands in absorption regions. The reflectance extracted for the atmospheric correction models can directly be compared to spectra extracted from image and field measured spectra. For the study reflectance images are derived from the ATCOR-2 and FLAASH atmospheric correction models. The reflectance spectra extracted from the two

atmospheric correction models are compared visually for known absorption features of atmospheric gases and other known materials.

The output of the ATCOR-2 and FLAASH corrected sample pixel spectrum matches closely with the reference spectra taken from library throughout the spectral range expecting for band 1, 2 and 4. In these bands, ATCOR-2 corrected image exhibits low reflectance values while the values are slightly higher in other bands.

FLAASH extracted spectra follow the same trend as ATCOR-2 spectra. It also matches closely with the library spectra, since the difference between the library values and FLAASH values is less. The outputs of both the correction models display high reflectance values in SWIR region.

The thermal atmospheric correction tool of ENVI corrects the atmospheric errors of thermal bands of EMR. The output VNIR-SWIR data from FLAASH algorithm and corrected thermal bands are used for further classification of albitite areas.

CHAPTER 6

DATA PROCESSING

Detailed studies of igneous activity and associated alteration across the globe have shown beyond doubts that the majority of such activity are closely related to their structural setting, host and source rocks, and the types of alteration (hydrothermal or supergene). Most of these factors can be evaluated with remote sensing owing to its synoptic view. The discussion of structural and lithological characteristics of the study area in Chapter 2 and ground-truth based on field and laboratory data in Chapter 4, suggest a close genetic relationship between the stratigraphy, structure and tectonic events in KCB and accompanying alteration. The study area is structurally complex and climatically semi arid, which gives a great opportunity for remote investigation of the area.

One of the main goals of this research is to investigate the utility and capability of spaceborne remote sensing data (Landsat and ASTER) to characterize the spectral features of albitite zones and host rocks. The main emphasis of this chapter is on investigating satellite dataset's unique spectral coverage in the VNIR-SWIR region in conjunction with TIR channels, for mapping of albitite. The work presented here is an outcome of exhaustive evaluation of the processing techniques — both simple and advanced, to differentiate, identify and map the albitite zone in the study area.

The reliability of ASTER scene processing for albitite mapping is largely unknown due to the non-unique spectral response of the range of mineral mixtures that can be expected within a particular lithologic background setting. Although widely applied in the remote sensing literature using routine mineral mapping techniques, it is not possible to assess the validity and quality of the results.

The test area is composed of metamorphic rocks ranging from pure silicates (quartzites), impure carbonates (actinolite-diopside marbles and other calc-silicates) and mafic rocks (amphibolites). The intrusives in the area range from granites and granodiorites, to melanocratic amphibolites. The rocks are variously weathered. Scant to nil vegetation cover for most rocky surfaces and a semi-arid climate makes the study area favorable for remote lithologic mapping.

The complexity of the problem demanded that the processing be attempted in several independent series of steps. The broad methodology of the entire workflow is shown in Fig. 3.4

The data processing is majorly divided into three broad categories:

1. DPCA processing of ASTER and Landsat data
2. Stereo processing of Cartosat -1 data
3. Spectral processing of ASTER data

6.1 DPCA PROCESSING OF LANDSAT AND ASTER DATA:

Landsat data has been utilized for locating hydrothermal alteration zones by identifying iron oxides and hydrous minerals (Abrams *et al.*, 1983; Kaufman, 1988; Tangestani and Moore, 2001). The result of the hydrothermal fluid which alters the chemical and mineralogical composition of the rock is evident in the country rock consisting of ore deposits associated with hydrothermal activity (Rutz-Armenta and Prol-Ledesma, 1998).

The principal component analysis is a multivariate statistical transformation. The technique calculates the uncorrelated linear combinations (eigenvector loadings) of variables in a manner so that each successive linear combination (principal component) has a smaller variance than its predecessor. The principal component analysis is widely used to map alteration areas (Abrams *et al.*, 1983; Kaufman, 1988; Loughlin, 1991; Bennett *et al.*, 1993; Tangestani and Moore, 2001).

Crosta technique is also called as feature oriented principal components selection (Tiwari *et al.*, 2011). The technique focuses on determining the principal components containing spectral diagnostic features of specific minerals. It also focuses on calculating the contribution of each of the original bands to the principal components by analyzing the eigenvector and value. This technique also indicates whether the corresponding mineral will be represented in bright or dark tones in the principal components based on the magnitude and sign of the eigenvectors loadings. This technique can be applied on four

and six selected bands of TM data (Crosta and Moore, 1989; Rutz-Armenta and Prol-Ledesma, 1998).

Loughlin (1991) tested FPCS on TM image subscene of Roberts Mountains area, Nevada. He used Landsat TM band sets to derive spectral information about hydroxides, iron oxides+hydroxides and iron oxides. He termed this technique as Crosta Technique. Ruiz-Armenta and Prol-Ledesma (1998) detected rocks altered because of hydrothermal fluids in the western section of the Transmexican volcanic belt. They compared various methods for spectral enhancement of the and applied selective principle component analysis, crosta technique on six and four bands of Landsat data, DPCA, decorrelation stretch and HSI transformation on Landsat TM image of the area. The method that proved to be the most efficient is found to be crosta technique using four TM bands combined with the HSI transformation.

Carranza and Hale (2002) processed Landsat TM image and integrated it with ground information in the Baguio district of the Philippines to map hydrothermally altered areas in terrain with dense vegetation. They applied crosta technique and software defoliant technique on the Landsat TM image for identification of limonitic and clay alteration areas. However, they found that these two techniques are not adequate to map hydrothermally altered areas using remotely sensed images. They developed new methodology for mineral imaging using Landsat TM data. Tangestani and Moore (2001) mapped the porphyry copper alteration in the Meiduk area, Iran by using crosta technique and stretched-unstretched principal component transformations on Landsat TM bands.

Crosta *et al.* (2003) applied the crosta technique to map the occurrence of mineral end members related to epithermal gold deposits. The study was carried out on ASTER (Advanced Spaceborne Thermal Emission and Reflection Radiometer) SWIR bands of Patagonia, Argentina.

For the study Landsat ETM+ and ASTER images are used. Preprocessing of the used data was explained in Chapter 5. The detailed steps of the crosta processing are given in Fig. 6.1.

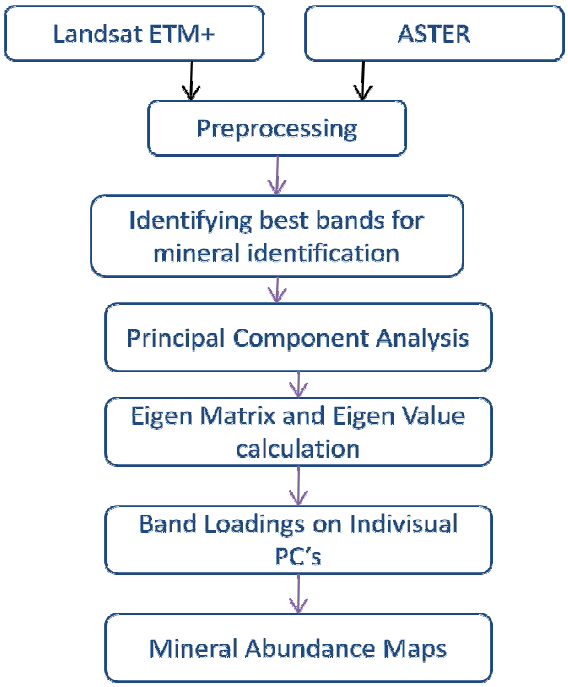

Fig. 6.1: Methodology for Crosta Processing

The study area mainly consists of felspathic quartzite. Among feldspar, K-feldspar is dominant in the study area. Few samples show presence of amphibole and biotite also. The main altered minerals in the study area include albite, epidote, chlorite, calcite and kaolinite.

The analysis has been carried out for five minerals. These are albite, calcite, chlorite, epidote and kaolinite. The reason for the selection of these minerals is that these minerals are alteration products in the study area. They can be utilized in this technique because the crosta Technique is widely used for mineral mapping. This technique is very successful to enhance some target minerals which has a smaller variance. The spectral reflectance curves for the minerals are analysed for selecting bands with maximum information about the minerals. Corresponding bands of both the satellites (Fig. 6.2) are selected for crosta processing. The reflectance curve of these minerals resampled to ASTER wavelengths is shown in Fig. 6.3

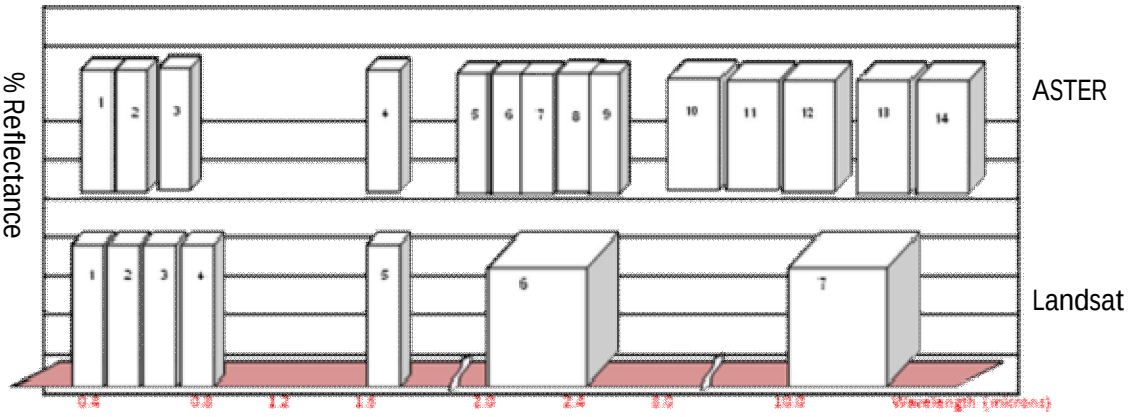

Fig. 6.2: ASTER and Landsat 7 spectral bands in electromagnetic spectrum (modified after Abrahams and Hook, 2002)

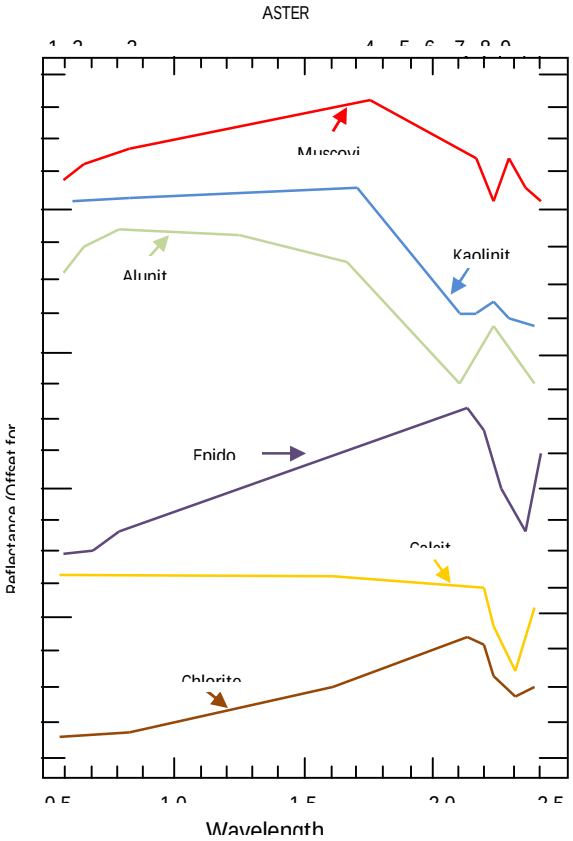

Fig. 6.3: Laboratory spectra of muscovite, kaolinite, alunite,epidote, calcite and chlorite resampled to ASTER band passes. Spectra include muscovite, typical in phyllic alteration zone, with a 2.20µm absorption feature; kaolinite and alunite, which are common in argillic iteration zone, have 2.17µm secondary absorption features and epidote, calcite and chlorite which are typically associated with propylitic alteration zone and display 2.35µm absorption features (modified after Mars and Rowan, 2006)

6.1.1 Albite

The USGS and JHU spectral library reflectance curve for albite (Fig. 6.4 a & b) shows a small dip at 1.4 µm and another at 2.18 µm. There is a characteristicdip at 8.5 µm. Thus the corresponding bands of ASTER and ETM+ data are chosen. For recognition of albite which is the index mineral of albitite, bands 4, 5, 7 and 10 of ASTER data have been chosen to take part in principal component analysis. For Landsat ETM+ data bands 2, 4, 5 and 7 are utilized for principal component analysis.

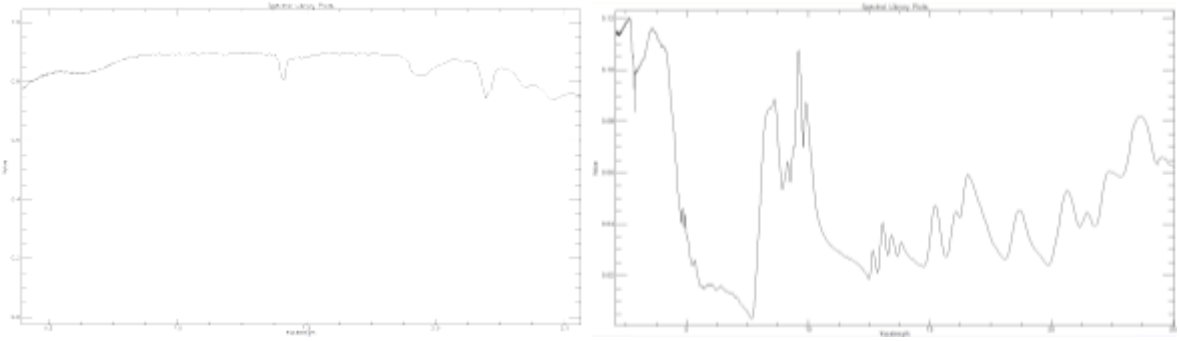

a b

Fig. 6.4: Spectral Reflectance Curve for Albite (Source: USGS and JHU Spectral Library)

Table 6.1a shows loadings of various bands on the principal components of ASTER data set.

Table 6.1: Loading of bands on principal components for albite a) ASTER b) ETM+

	Band4	Band6	Band7	Band10
pc1	0.77	-0.63	-0.001	0.011
pc2	0.63	0.76	-0.08	0.02
pc3	0.05	0.03	0.4	-0.89
pc4	0.04	0.04	0.89	0.44

a

	Band5	Band6	band 7
pc1	-0.12687	-0.87631	-0.50695
pc2	0.090245	-0.15642	0.100472
pc3	-0.00135	0.130606	0.050333
pc4	-0.13827	-0.07193	0.01743

b

The reflectance curve of albite shows absorption dips at 2.2 µm and 8.5 µm, which corresponds to band 7 and 10 of ASTER and Landsat. Analyzing the loading matrix it was concluded that for ASTER data band 7 has highest loading in PC4 with a positive sign and band 10 has highest loading in PC3 and is negative, thus the corresponding feature would be seen in dark color in PC3. For Landsat data band 7 has highest loading in PC 1 which is also negative. So the feature should be dark in colour. Fig. 6.5 shows PC3 and PC 1 for ASTER and Landsat data with albite rich areas in red colour.

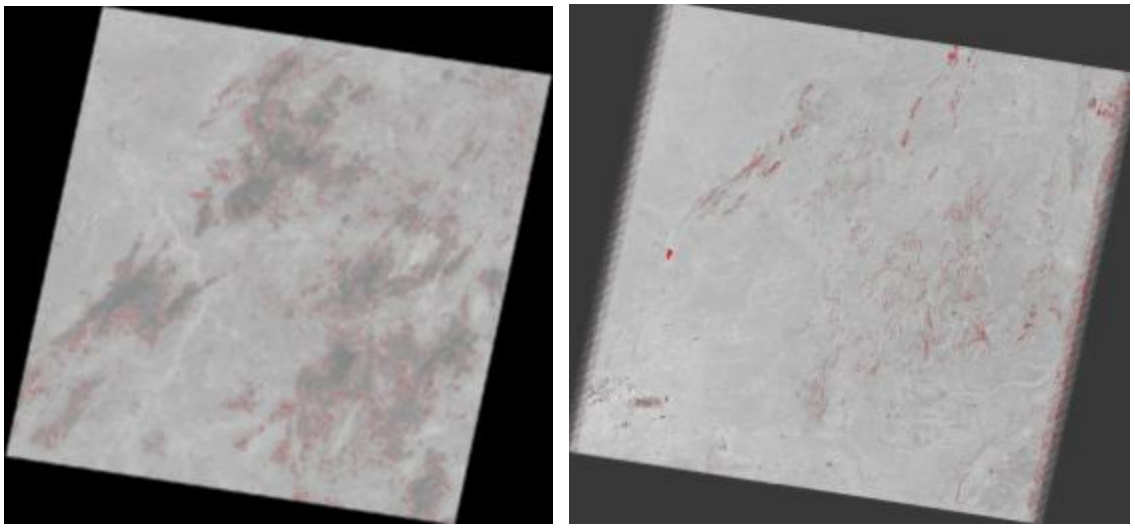

a **b**

Fig. 6.5 Albite rich areas a) PC 3 of ASTER data b) PC 1 of Landsat data

6.1.2 Epidote

The USGS and JHU spectral library reflectance curve for epidote (Fig. 6.6 a & b) shows a small dip at 0.5 µm and 1 µm and another strong absorption dip at 2.3 µm. A small high reflectance is seen at 0.6 µm and another one at 2.2 µm. Thus the corresponding bands of ASTER and ETM+ data are chosen. For recognition of epidote, bands 2, 7, 8 and 10 of ASTER data have been chosen as input for principal component analysis. For Landsat ETM+ data bands 2, 3 and 6 are utilized for principal component analysis.

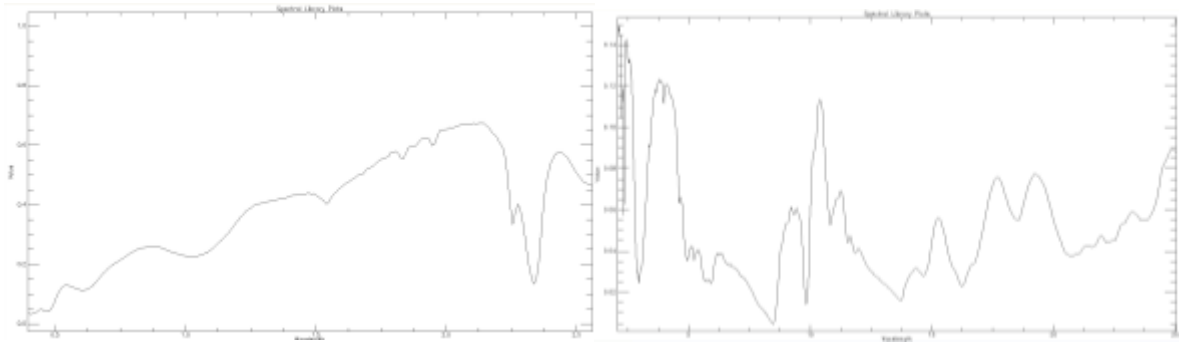

a b

Fig. 6.6: Spectral Reflectance Curve for Epidote (Source: USGS and JHU Spectral Library)

Table 6.2: Loading of bands on principal components for epidote a) ASTER b) ETM+

	band 2	band 3	band 6
pc1	0.973749	0.289943	0.432453
pc2	0.383762	0.216428	-0.09497
pc3	-0.09883	0.137828	0.007166

a

	band 2	Band7	band 8	band 10
pc1	6.299285	4.44733	0.791852	0.412086
pc2	0.262459	0.219972	-0.35947	-0.04989
pc3	0.005535	0.005322	1.349244	-1.12345
pc4	0.000601	0.019127	0.175725	0.406438

b

The reflectance curve of epidote shows a dip at 2.3 µm, which corresponds to band 8 of ASTER and band 6 of Landsat. Analyzing the loading matrix it is concluded that for ASTER data band 7 has highest loading (4.44) in PC1 and the corresponding feature would be seen in bright color. For Landsat data band 6 has highest loading in PC 1 (0.43) and the feature should be bright in colour. Fig. 6.7 shows PC1 for ASTER and Landsat data with epidote rich areas in red colour.

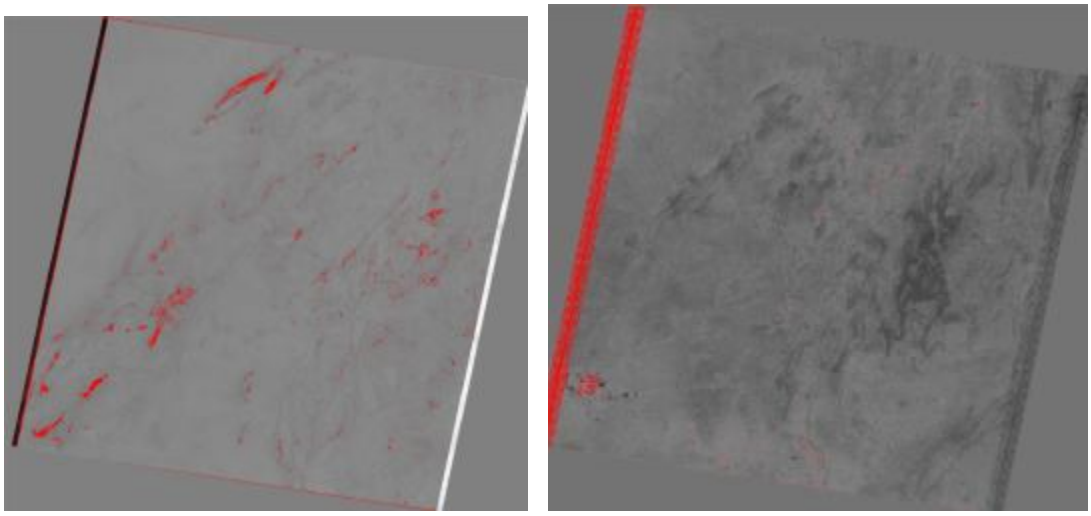

a **b**

Fig. 6.7 Epidote rich areas a) PC 1 of ASTER data b) PC 1 of Landsat data

6.1.3 Calcite

The USGS and JHU spectral library reflectance curve for calcite (Fig. 6.8 a & b) shows two small dips before 2.0 µm and another strong absorption dip at 2.28 µm. A strong absorption dip is also observed at 6 µm. Thus the corresponding bands of ASTER and ETM+ data are chosen. For recognition of calcite, bands 6, 7, 8 and 10 of ASTER data have been chosen as input for principal component analysis. For Landsat ETM+ data bands 3, 5 and 6 are utilized for principal component analysis.

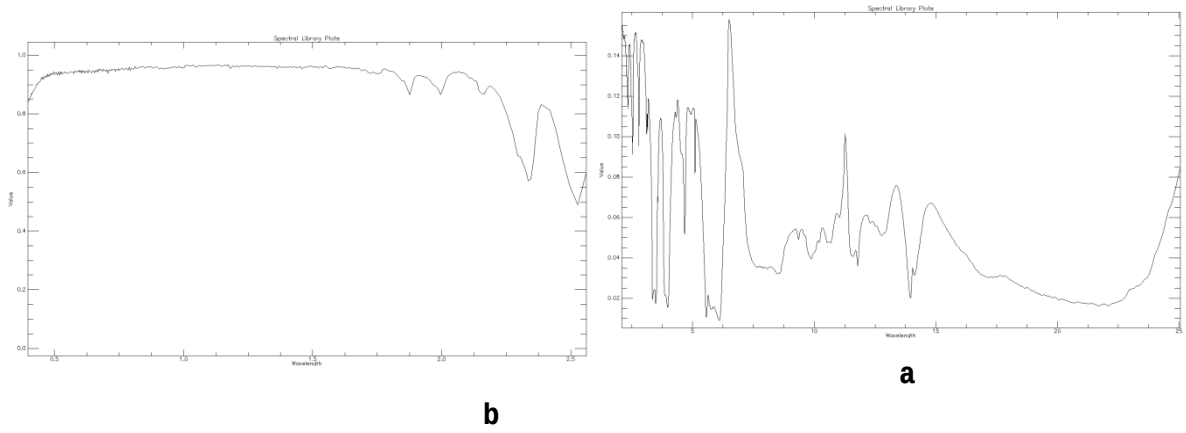

a

b

Fig. 6.8: Spectral Reflectance Curve for Calcite (Source: USGS and JHU Spectral Library)

Table 6.3: Loading of bands on principal components for calcite a) ASTER b) ETM+

	band 3	band 5	band 6
pc1	0.954897	-0.66082	0.42839
pc2	0.325478	-0.04301	0.111541
pc3	-0.12821	-0.21325	0.032246

a

	band 6	band 7	band 8	band 10
pc1	5.268868	-5.63476	0.181117	1.864443
pc2	0.076435	1.144406	-1.01595	0.540948
pc3	0.006031	0.054429	0.056859	-0.95601
pc4	0.003357	0.057446	0.584723	0.069696

b

The reflectance curve of calcite shows a strong absorption at 2.28 µm, which corresponds to band 8 of ASTER and band 6 of Landsat. Analyzing the loading matrix it is concluded that for ASTER data band 8 has highest loading (0.58) in PC1 and the corresponding feature would be seen in bright color. For Landsat data band 6 has highest loading in PC 1 (0.42) and the feature should be bright in colour. Fig. 6.9 shows PC 4 for ASTER and PC 1 for Landsat data with calcite rich areas in red colour.

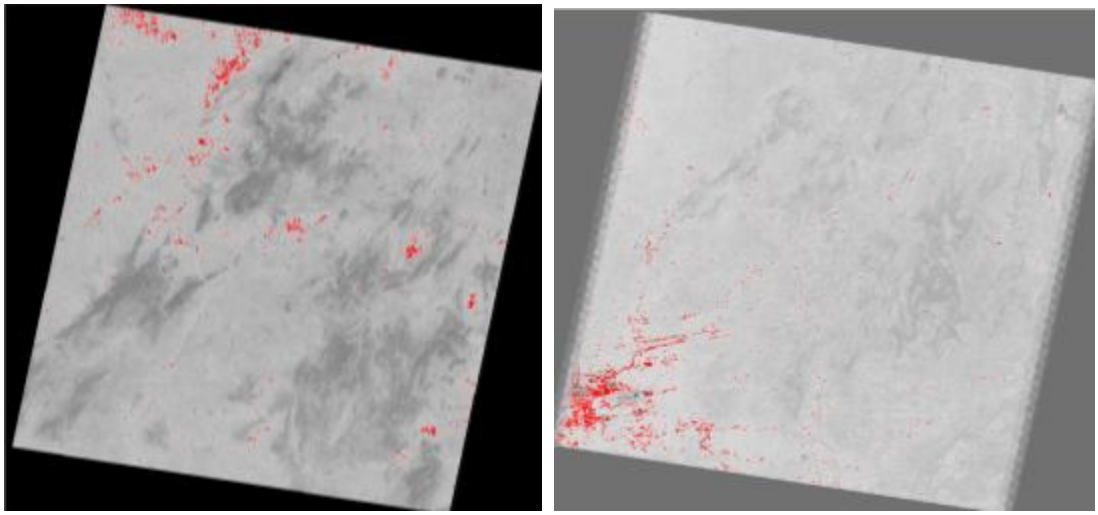

a **b**

Fig 6.9 Calcite rich areas a) PC 4 of ASTER data b) PC 1 of Landsat data

6.1.4 Chlorite

The USGS and JHU spectral library reflectance curve for calcite (Fig. 6.10 a & b) shows a small dip at 0.64 µm and a high reflectance at 1.64 µm. A strong high reflectance is seen at 2.1 µm and a corresponding low at 2.3 µm. Thus the corresponding bands of ASTER and ETM+ data are chosen. For recognition of chlorite, bands 2, 5, 6 and 9 of ASTER data have been chosen as input for principal component analysis. For Landsat ETM+ data bands 3, 5 and 7 are utilized for principal component analysis.

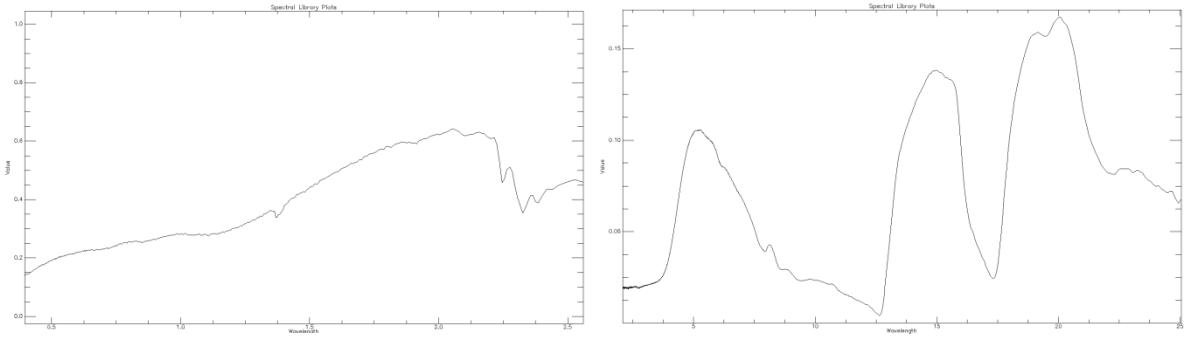

a **b**

Fig. 6.10: Spectral Reflectance Curve for Chlorite (Source: USGS and JHU Spectral Library)

Table 6.4: Loading of bands on principal components for chlorite a) ASTER b) ETM+

	band 2	band 5	band 6	band 9
pc1	4.463786	-5.87828	-1.28789	-0.17585
pc2	0.005132	0.860254	-0.37695	-1.22952
pc3	0.001877	0.208404	0.388604	0.158568
pc4	0.000481	0.114952	-0.10646	0.825297

a

	band 3	band 5	band 7
pc1	0.954897	-0.66082	-0.42839
pc2	0.325478	-0.04301	0.111541
pc3	-0.12821	-0.21325	0.032246

b

The reflectance curve of chlorite shows a high at 2.1µm, which corresponds to band 6 of ASTER and 5 of Landsat. Analyzing the loading matrix it is concluded that for ASTER data band 6 has highest loading (-1.2) in PC1 and the corresponding feature would be seen in dark color. For Landsat data band 5 has highest loading in PC 1 (-0.66) and the feature should be dark in colour. Fig. 6.11 shows PC 1 for ASTER and Landsat data with chlorite rich areas in red colour.

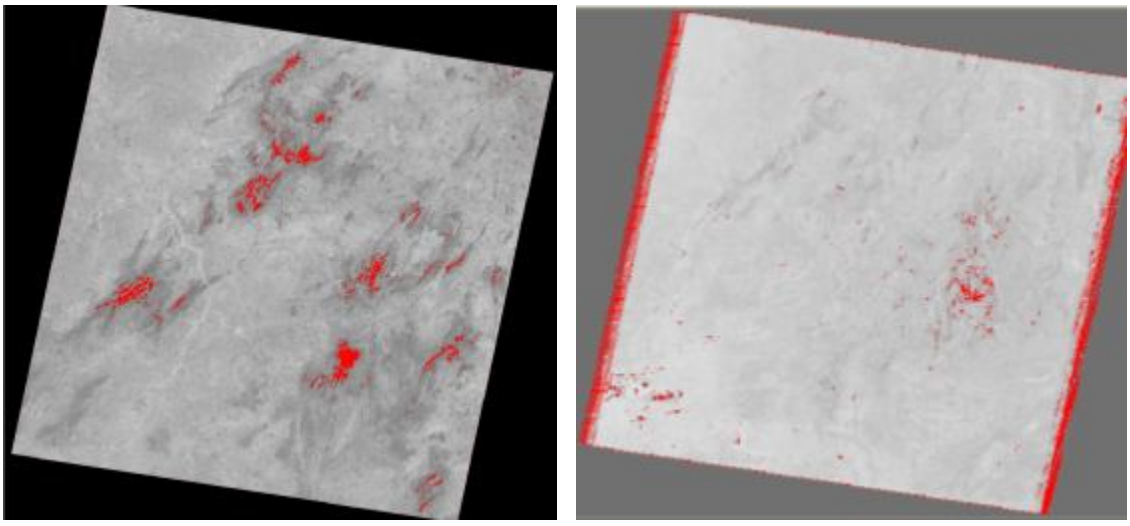

a **b**

Fig. 6.11 Chlorite rich areas a) PC 1 of ASTER data b) PC 1 of Landsat data

6.1.5 Kaolinite

The USGS and JHU spectral library reflectance curve for kaolinite (Fig. 6.12 a & b) shows a dip at 1.4 µm and a high reflectance at 1.5 µm. A strong high reflectance is seen at 2.0 µm and a corresponding low at 2.1 µm. Thus the corresponding bands of ASTER and ETM+ data are selected. For recognition of kaolinite, bands 4, 5 and 7 of ASTER data have been chosen to take part in principal component analysis. For Landsat ETM+ data bands 3, 5 and 7 are utilized for principal component analysis.

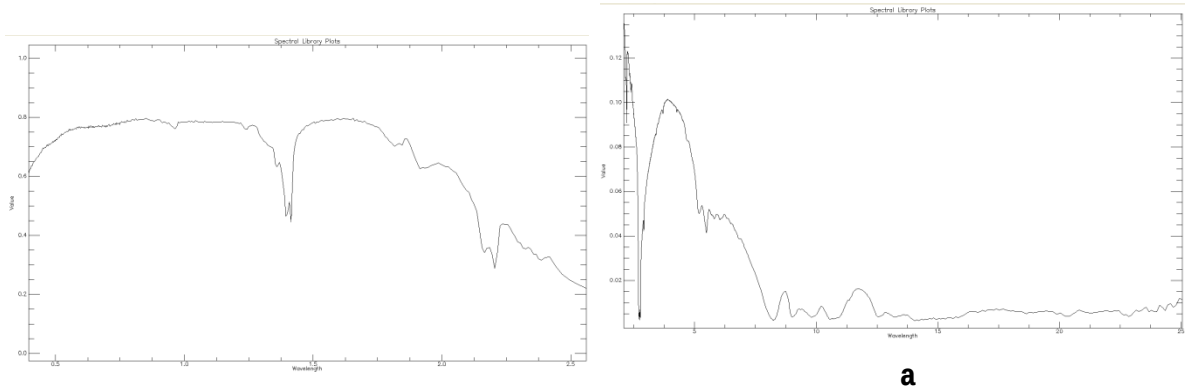

b a

Fig. 6.12: Spectral Reflectance Curve for Kaolinite (Source: USGS and JHU Spectral Library)

Table 6.5: Loading of bands on principal components for kaolinite a) ASTER b) ETM+

	Band4	band5	band7
pc1	5.266916	-5.26692	2.4097
pc2	0.010651	0.644368	-1.34172
pc3	0.003744	0.61084	0.31087

a

	band 3	band 5	band 7
pc1	0.954897	-0.66082	-0.42839
pc2	0.325478	-0.04301	0.111541
pc3	-0.12821	-0.21325	0.032246

b

The reflectance curve of kaolinite shows a high at 1.5μm, which corresponds to band 4 of ASTER and 5 of Landsat. Analyzing the loading matrix it is concluded that for ASTER data band 4 has highest loading (5.2) in PC1 and the corresponding feature would be seen in bright color. For Landsat data band 5 has highest loading in PC 1 (-0.66) and the feature should be dark in colour. Fig. 6.13 shows PC 1 for ASTER and Landsat data with kaolinite rich areas in red colour.

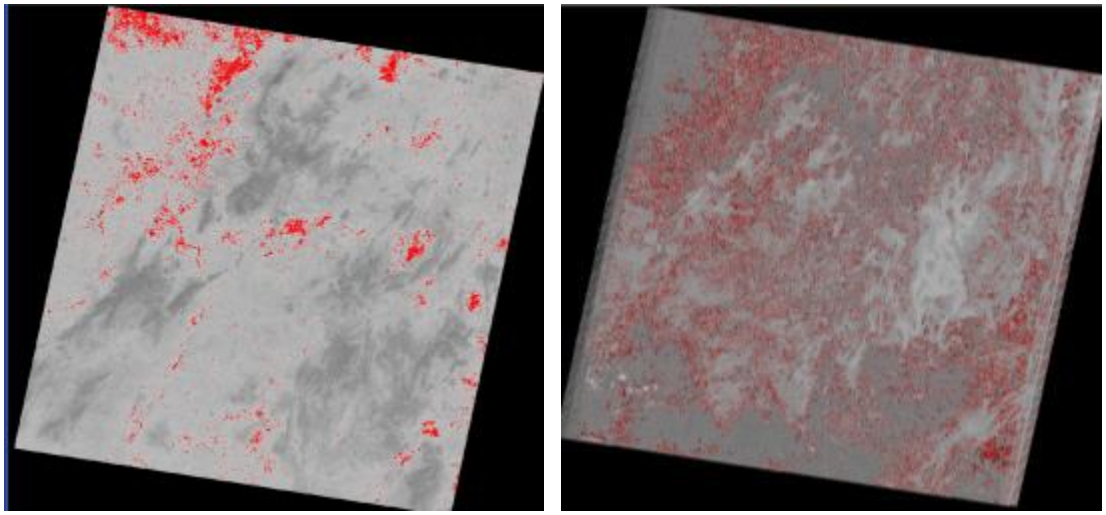

a **b**

Fig 6.13 Kaolinite rich areas a) PC 1 of ASTER data b) PC 1 of Landsat data

6.2 STEREO PROCESSING FOR DEM GENERATION

In order to have more insights into the characteristics of albitite emplacement in the study area and also to investigate the control of structure on the process, a 3D model was generated using Cartosat -1 Data. Digital surface models (DSMs) are elevation models of the surface of the earth which provides a geometrically correct reference frame for measurements and visualization.

The elevation models used for final analysis are generated using stereo images procured from space based sensor. The capabilities of ERDAS IMAGINE v 9.1 are utilized for processing and final analysis of the data. Photogrammetric module (Leica Photogrammetric Suite) of the software is exploited to automatically extract elevation information from Cartosat -1 stereo data product. The overall methodology adopted in the study can be presented as given below and in Fig. 6.14:

- Image data looking in fore and aft direction along with metadata information is procured. This information can be used for obtaining interior orientation parameters required for further processing.
- Combine data collected from topomap, GPS measured control points for exterior orientation of image pair.
- Automatic extraction of DEM after 3-D modeling process, interpolation, proper modification and accuracy assessment.

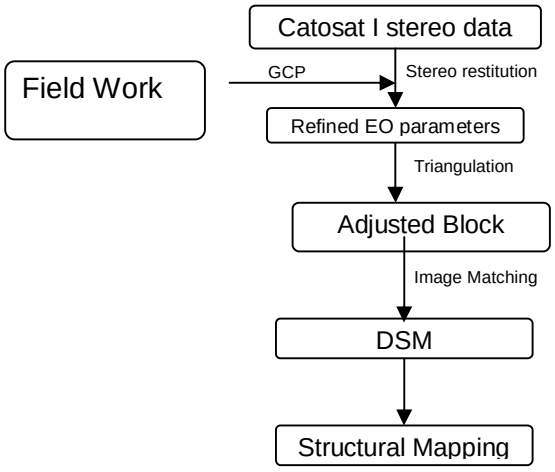

Fig 6.14: Methodology adopted for DSM generation

6.2.1 Ground Control Point Collection

Ground Control Points (GCP's) are collected in Khetri area using instrument Leica GPS 500 (Geodetic Single Frequency Receiver). To achieve suitable accuracy, the single frequency geodetic GPS receiver (Fig. 6.15) was used in differential mode. The following criteria are followed in acquiring GCPs (Gupta, 2005):

1.) GCP as a point, which are clearly identified and positioned on the image data as well as corresponding map.

2.) The point should be preferably permanent in nature.

3.) The surroundings regions of GCPs should have good contrast helping to precisely position the point.

Fig. 6.15: Leica GPS 500 system

A total of 11 GCPS are collected in differential mode (Fig. 6.16)

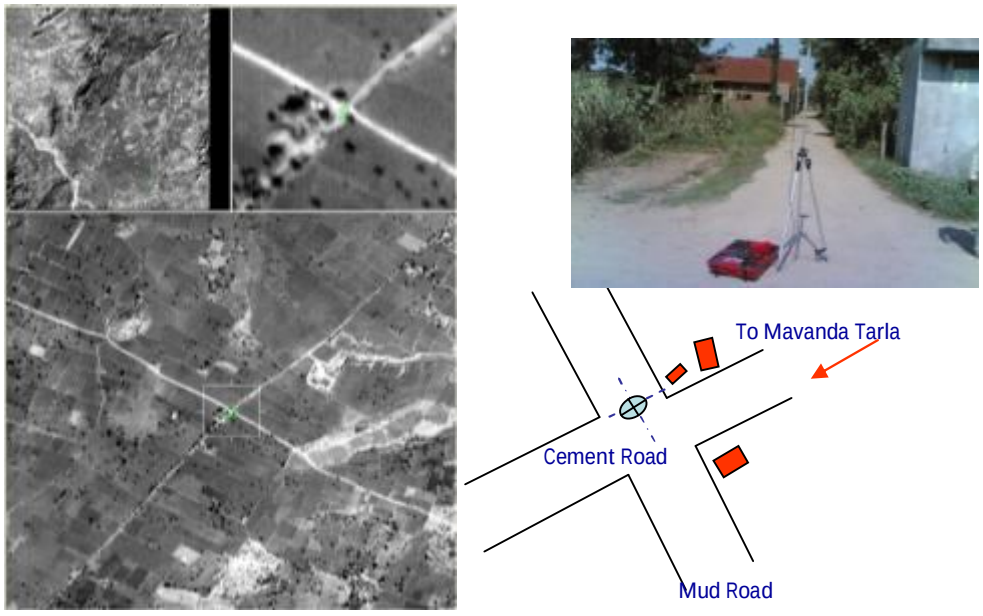

Fig. 6.16: GCP Collection in the field

6.2.2 Stereo restitution

The stereo pair is oriented using rational polynomials supplied along with the dataset. A rational function is a function that can be represented as the quotient of two polynomials. The rational function formulates the relationship between a ground point and the corresponding image point as ratios of polynomials (Kumar and Gupta, 2005):

$$r_i = p1(X_i,Y_i,Z_i)/p2(X_i,Y_i,Z_i)$$

$$c_i = p3(Xi,Yi,Z_i)/p4(X_i,Y_i,Z_i)$$

Where r_i and c_i are the normalized row and column index of pixels in image respectively, p1, p2, p3 and p4 are the polynomial coefficients. X_n, Y_n and Z_n are normalized coordinate values of a point in ground coordinate system. To avoid the complexity in the

calculation, the maximum power of each ground coordinate and also the total power of all ground coordinates is also limited to 3.

The stereopair is oriented and DSM is extracted. The rational polynomial coefficients are refined using ground control points (8 in number for one scene and 7 for the other scene). Ground control information for this area is collected from the field using single frequency GPS in differential mode (Fig. 6.17).

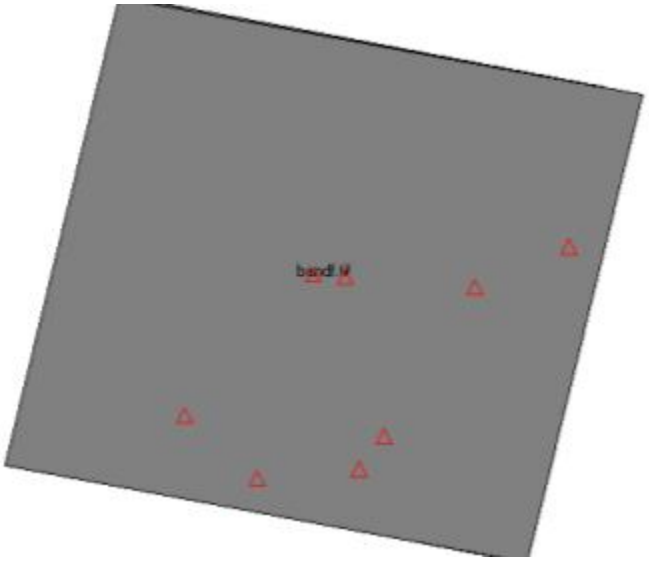

Fig. 6.17: GCP distributions in area

The tie points are generated automatically using point matching technique. The stereopair was again oriented using GCP's and tie points. The adjusted block (GCP's + tie points) exhibited an orientation error of 0.23 pixels. The average planimetric error was 3.7 m whereas vertical error ranged between 0.1 to 6 m. Some points exhibited large residuals which might be attributed to placement uncertainty in fore image as the image was radiometrically smoother and geometrically distorted. The topography of the area, even small residual hills and minor streams are clearly seen in the refined elevation model (Fig. 6.18).

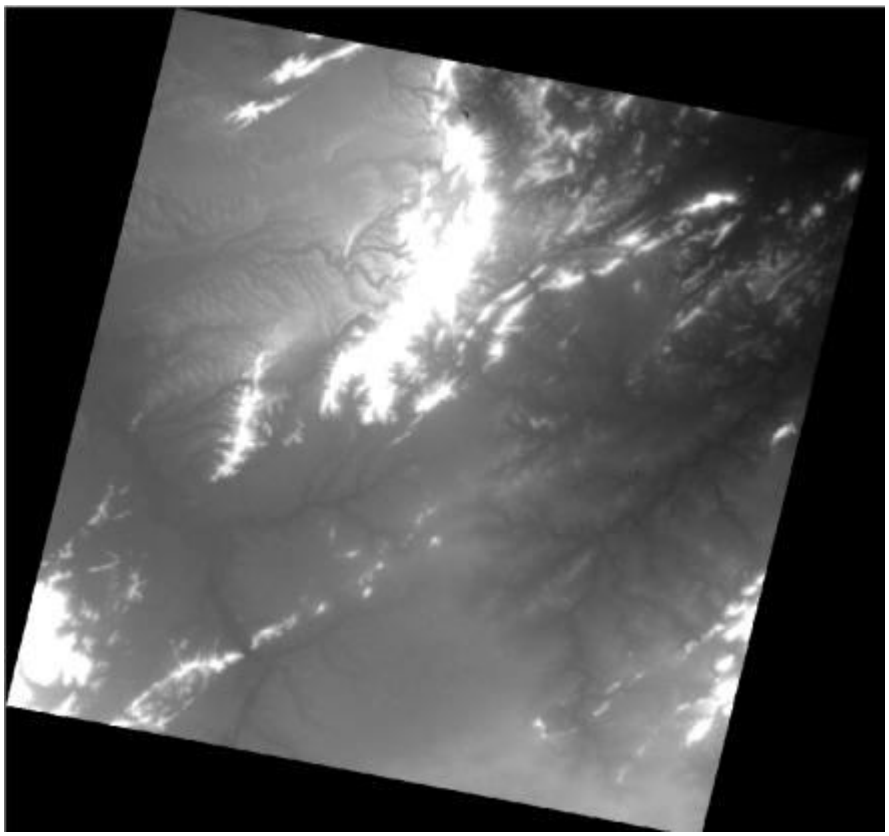

Fig. 6.18: DSM of the study area

6.2.3 DEM Data: Structural Analysis

Since the geological lineaments are directional in nature, thus directional filtering is needed in geological remote sensing (Tripathi, 1988). Though many directional edge filters are available, whether or not they can be used effectively for natural surface features has not been well studied (Tripathi *et al.*, 1997). Morphological image processing has been used extensively for lineament extraction (Sanjeevi and Bhaskar, 2008). The morphological processing can be used efficiently for digital enhancement of lineaments. A proper choice of structuring elements without the involvement complex mathematical and statistical operations results in preservation of the basic morphology and homotopy of the image (Tripathi *et al.*, 2000).

DSM data was analyzed in order to map out the structure in the study area. Digital elevation model (DEM) reveals the surface expression of the earth geomorphology and is useful in delineating structural information of the earth surface. Bretar and Chehata

(2010) described digital elevation model as representation of the earth topography. Cartosat -1 surface model was used in conjunction with ASTER and Landsat data to identify lineaments (faults and fractures) and other interesting features in the study area in order to understand the interrelationship between the structure in area and albitite zone (Fig. 6.19 a & b). The Cartosat -1 DSM is high resolution data and does not require much processing. However, some enhancement was carried out for better interpretation. The dataset was stretched with different elevation values to highlight differences in the topography and structural features in the study area. Combination of the hill-shaded image and the DEM data assisted in identifying the structural features in the area.

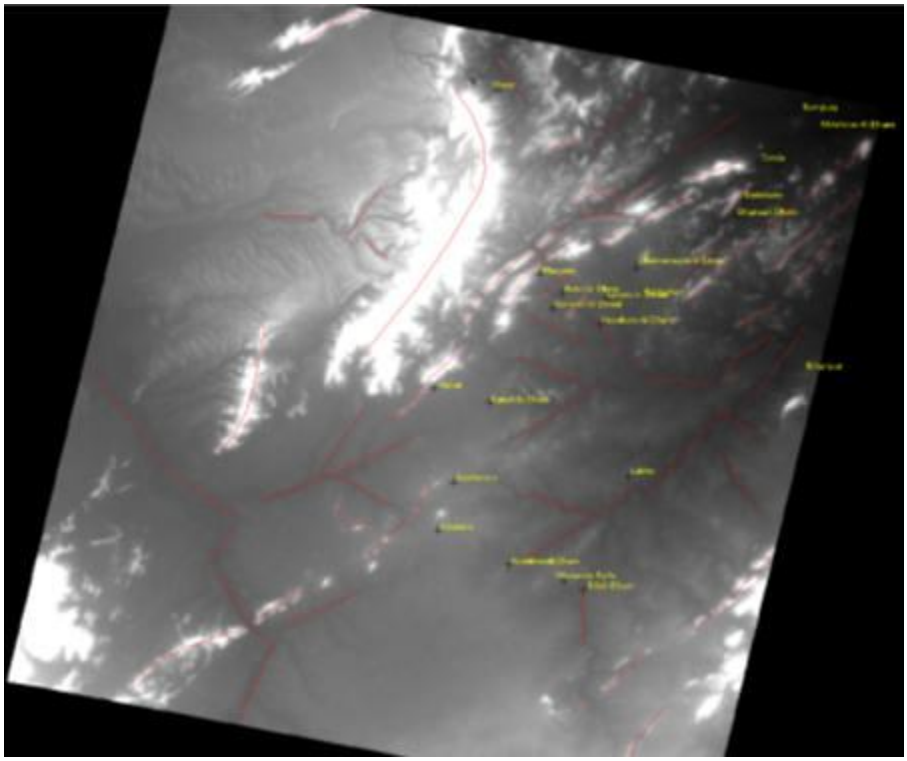

Fig. 6.19 a: Lineaments in part of the study area interpreted from Cartosat -1 DSM

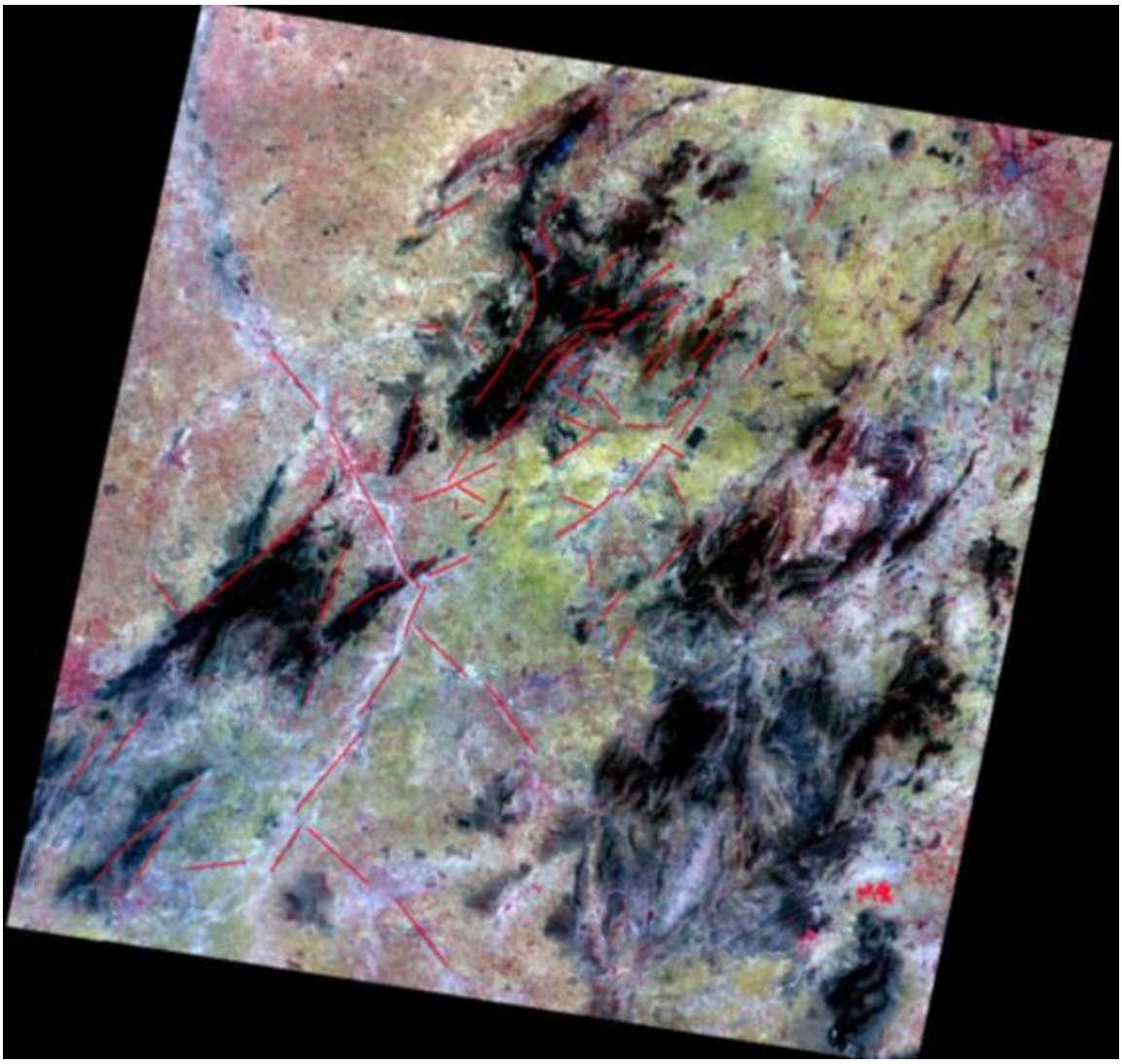

Fig. 6.19 b: Lineaments extracted from Cartosat -1 DSM overlayed on ASTER image

The major lineaments in the study area are trending in NE-SW direction coinciding with the reported trend of albitite line. Some cross cutting lineaments are also seen indicating multiple episode of faulting. The reported occurrence of albitite is mainly falling in the line of the interpreted lineaments. Previous studies have also shown that structures such as faults, shear zones or fracture have some form of control on formation of many types of igneous activity and mineralization associated with hydrothermal system (Forde and Bell, 1994).

6.3 SPECTRAL PROCESSING OF ASTER DATA

The atmospherically and topographically corrected ASTER surface reflectance data have been digitally processed to highlight the zones of alteration, and to identify albite rich areas in the study area. The workflow of spectral processing of ASTER data was designed in a manner that the level of complexity increases gradually. It starts with color display of 3-band composites, to band ratioing and spectral indices, and finally to spectral processing and image classification methods. These techniques and the results derived hence have been described in the following sections. Band composites, band ratios and spectral indices are carried out for nine bands pertaining to VNIR-SWIR part of the EMR. Since TIR bands have low spatial resolution, thus this data was subjected to only digital image classification.

6.3.1 Band composites

Multispectral remote sensing image analysis begin with displaying images in color by assigning individual bands to the red, green and blue color in creating 3-band color composite images. This allows rapid preliminary image interpretation before having to analyze the complete spectral dimensionality of the dataset.

There can be 84 number of possible distinct 3-band RGB combinations which can be made out of the 9 VNIR-SWIR band. Though the bands best suited for indentifying a particular mineral can be found using the spectral reflectance curve, for an area without any ancillary information the wide range of spectral diversity makes this approach unrealistic. To overcome this difficulty, a statistical band selection technique called the Optimum Index Factor (OIF; Chavez *et al.*, 1982) method has been used. The OIF ranks all possible RGB color combinations that can be generated using a multispectral remote sensing data based on the total variance within the bands and the band to band correlations (Chavez *et al.*, 1982; Chavez *et al.*, 1984). Higher OIF values indicate greater spectral contrast in the band-composite and thus greater amount of information. Mathematically, the OIF is expressed as follows:

$$OIF = \sigma_K + \sigma_L + \sigma_M / r_{KL} + r_{KM} + r_{LM} \quad \text{--------6.1}$$

Where: $\sigma_{K,L,M}$ are the standard deviations for the three bands K,L,M; and r_{KL}, r_{KM}, r_{LM} are the absolute values of the correlation coefficients between bands K&L, K&M and L&M respectively.

The optimum index factor was calculated for the 20 distinct combinations of the SWIR bands, and also on 84 distinct combinations of the VNIR-SWIR dataset. It was observed that the best OIF values are found for 4-6-8 (for SWIR bands) and 6-3-1 (for VNIR-SWIR bands). Fig. 6.20 shows these two band composites. The images have been linearly stretched to bring about the full color contrast. The results are in line with the reviewed literature which suggests that band 1 highlights Fe-O bearing areas as these surfaces absorb strongly in this region. Healthy vegetation has strong reflectance in band 3. The hydroxyl bearing rocks absorb heavily in band 6 and carbonates and chlorite has a strong absorption feature in band 8. The above said factors and the overall high rock reflectance in band 4 form the spectral bases behind the distinct litho/mineralogic information content of these band composites.

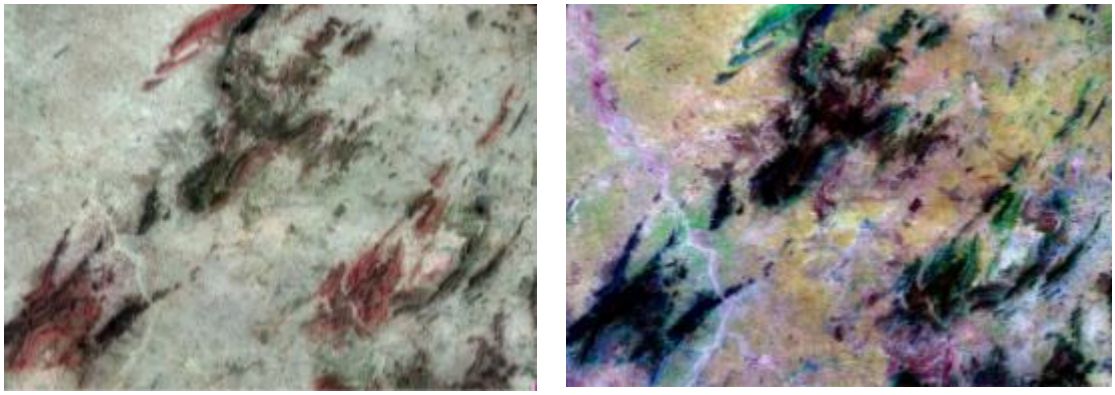

a **b**

Fig. 6.20: False Color Composites with maximum variance. a) 4-6-8 (for SWIR data alone) b) 6-3-1 (for VNIR-SW1R combined data)

In the SWIR band-composite (4-6-8), light red and pink hues indicate clay and micaceous areas which have strong OH absorption, the green hues indicate presence of carbonates and chlorite. The overall dark tones represent phyllite and schist bearing regions since they have low albedo and absorption for both OH and chlorite. The quartzites and alluvium appear in bright shades because of high albedo and absence of OH and chlorite. Vegetation appears in dark shades.

In band combination 6-3-1 many smaller bodies of rocks are shown more clearly than on the 4-6-8 composite, because of the higher spatial resolution (15m) of VNIR bands. Because of the high spatial resolution the structural complexity of the area is also highlighted. In this band composite the iron-bearing area have been shown in deep shades of red, OH-bearing surfaces have been displayed in shades of blue and the healthy vegetation in bright green colors. Bright mustard colors represent sandy soils, desert sands and quartzites. The main shear zone on this image appears in light blue-cyan colors whereas the amphibolites chloritic surfaces and carbonates appear in bright magenta shades. The intermediate colors represent mixtures of these categories.

6.3.2 Decorrelation stretch images

In SWIR data the bands are highly correlated to each other which result in similar spectral information in the bands. Decorrelation stretch (DCS) procedure was applied on the dataset to select RGB combinations of the 6 SWIR bands to highlight zones of specific spectral absorption features corresponding to various mineral assemblages. In the DCS colour composite image the subtle color contrasts appear prominently and more features can be identified. Two DCS band composites, viz: 4-6-8 and 5-7-9, have been found to display the most useful and explicit spectral information.

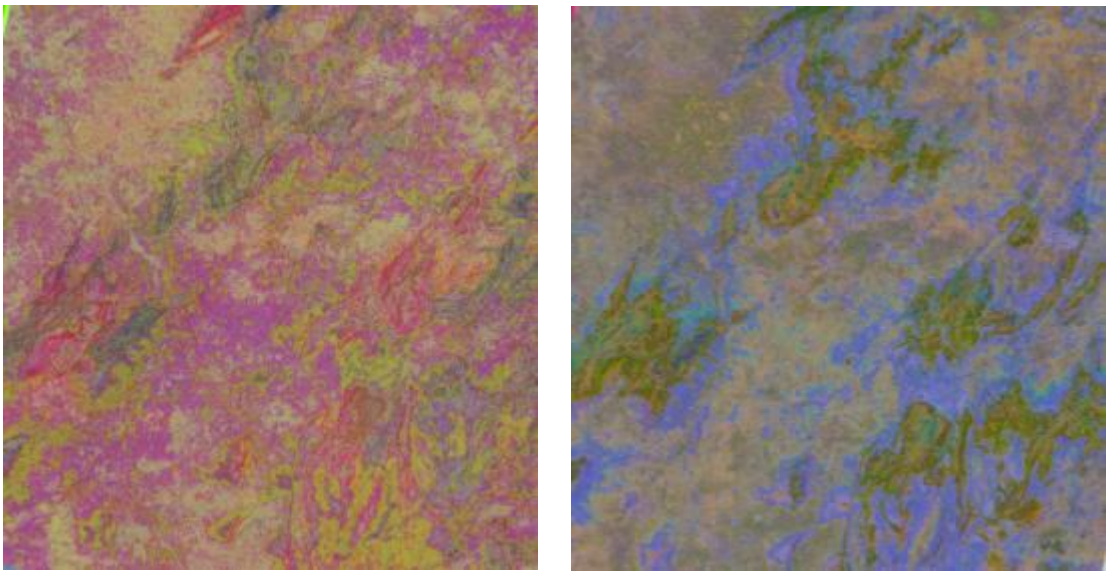

a **b**

Fig. 6.21: Decorrelation Stretch Image. a) 4-6-8 b) 5-7-9

Fig. 6.21 a shows the DCS composite 4-6-8 and fig 6.22 b shows composite 5-7-9. To emphasize on the utility of DCS, we can compare the normal FCC 4-6-8 in Fig. 6.20a with DCS 4-6-8 in Fig. 6.21 a. From the above images it is clear that on DCS 4-6-8 further distinction between surfaces with similar spectral signatures can be made. In a DCS image carbonate rocks appear in light green to yellow colour because of the lack of Fe-O absorption in band 4, whereas amphibolites with chlorite-rich surfaces appear in dark green shade. The main shear zone comes out prominently in magenta color in 4-6-8 composite.

6.3.3 Band ratios, RBD images, and Ratio Composites

Band ratio stands for division of pixel values in one band by those in another, pixel by pixel. It is one of the oldest and the most widely used method of discriminating surface cover types in a multispectral image. Band ratios suppress proportionally constant radiance values in the band and enhances the differences. Rowan *et al.* (1974) used the band ratios for the very first time. They demonstrated with Landsat- I MSS data of Silver Bell porphyry copper deposit area that a composite of ratios MSS1/MSS2, MSS2/MSS3 and MSS3/MSS4 in BGR provides a powerful means for discriminating hydrothermally

altered areas from regional rock and soil units. The above approach has been adapted for various subsequent types of passive remote sensing data in solar reflective region, including ASTER.

Relative absorption Band Depth (RBD) images are a modification of the normal band ratios, as they have a three-point ratio formulation. These images are calculated for individual absorption features. In these calculations the central band is taken at the absorption feature and its neighboring bands are added together to determine the numerator for the ratio. The central band is taken as the denominator. The underlying concept for RBD is the removal of the continuum to improve the intensity of the absorption feature (Crowley *et al.*, 1989). However, spectrally uncalibrated data can lead to results that are difficult to interpret (Crippen, 1988). Also, the terrain illumination differences due to topography can produce color variations in unadjusted ratio images for spectrally identical surface materials (Crippen, 1988).

A number of band ratios and RBD indices have been proposed for ASTER (Rowan and Mars, 2003). Ratio images can be generated from ASTER VNIR-SWIR and used together in a large number of combinations to suit a particular application and highlight particular feature (Fig. 6.22, 6.23, 6.24 and 6.25). To map altered mineral assemblages some of the most useful band ratios have been compiled along with their references and shown in Table-6.6.

Table 6.6 a: ASTER Band Ratios for Mineral Identification

Feature	Band or Ratio	Comments
Iron		
Ferric iron, Fe^3	2/1	
Ferrous iron, Fe^2	5/3 + 1/2	
Laterite	4/5	
Gossan	4/2	
Ferrous silicates (biot, chl, amph)	5/4	Fe oxide Cu-Au alteration
Ferric oxides	4/3	Can be ambiguous*
Carbonates / Mafic Minerals		
Carbonate / Chlorite / epidote	(7+9)/8	
Epidote / Chlorite / amphibole	(6+9)/(7+8)	Endoskarn
Amphibole / MgOH	(6+9)/8	Can be either MgOH or carbonate*
Amphibole	6/8	
Dolomite	(6+8)/7	
Carbonate	13/14	Exoskarn (cal/dolom)
Silicates		
Sericite / muscovite / illite / smectite	(5+7)/6	Phyllic alteration
Alunite / kaolinite/ pyrophyllite	(4+6)/5	
Phengitic	5/6	
Muscovite	7/6	
Kaolinite	7/5	Approximate only*
Clay	$(5\times7)/6^2$	
Alteration	4/5	
Host rock	5/6	
Silica		
Quartz rich rocks	14/12	
Silica	(11×11)/10/12	
Basic degree index (gnt, cpx, epi, chl)	12/13	Exoskrn (gnt, px)

SiO2	13/12, 12/13	Same as 14/12
Siliceous rocks	(11×11)/(10/12)	
silica	11/10, 11/12, 13/10	

Table 6.6 b Common ratio & band combinations for ASTER

Features	Red	Green	Blue
ALOH minerals/advanced argillic alteration	5/6 (phen)	7/6 (musc)	7/5 (kaol)
Clay, amphibole, laterite	(5×7)/6² (clay)	6/8 (amph)	4/5 (lat)
Gossan, alteration, host rock	4/2 (goss)	4/5 (alt)	5/6 (host)
Silica, carbonate	(11×11)/(10×12)	13/14	12/13
Discrimination for mapping	4/1	3/1	12/14
General Discrimination	4/7	4/1	(2/3) × (4/3)

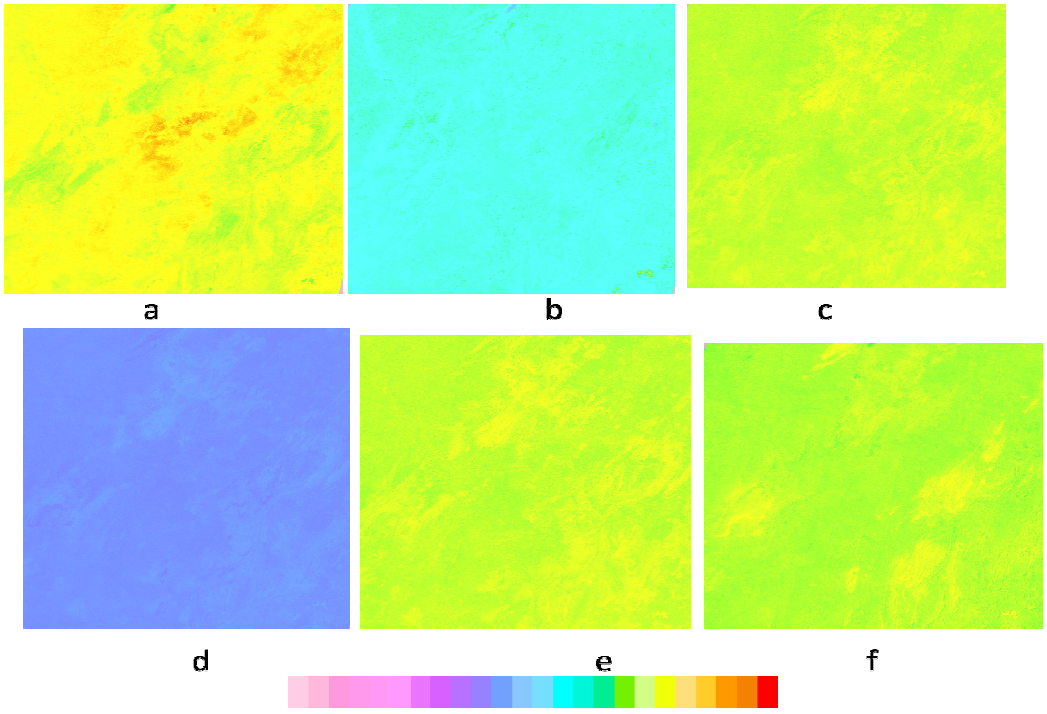

Fig 6.22: ASTER Spectral Indices a) Ferric, b) Ferrous, c) amphibole, d) epidote/chlorite, e) Mg-OH, f) alunite/kaolinite/pyrophyllite

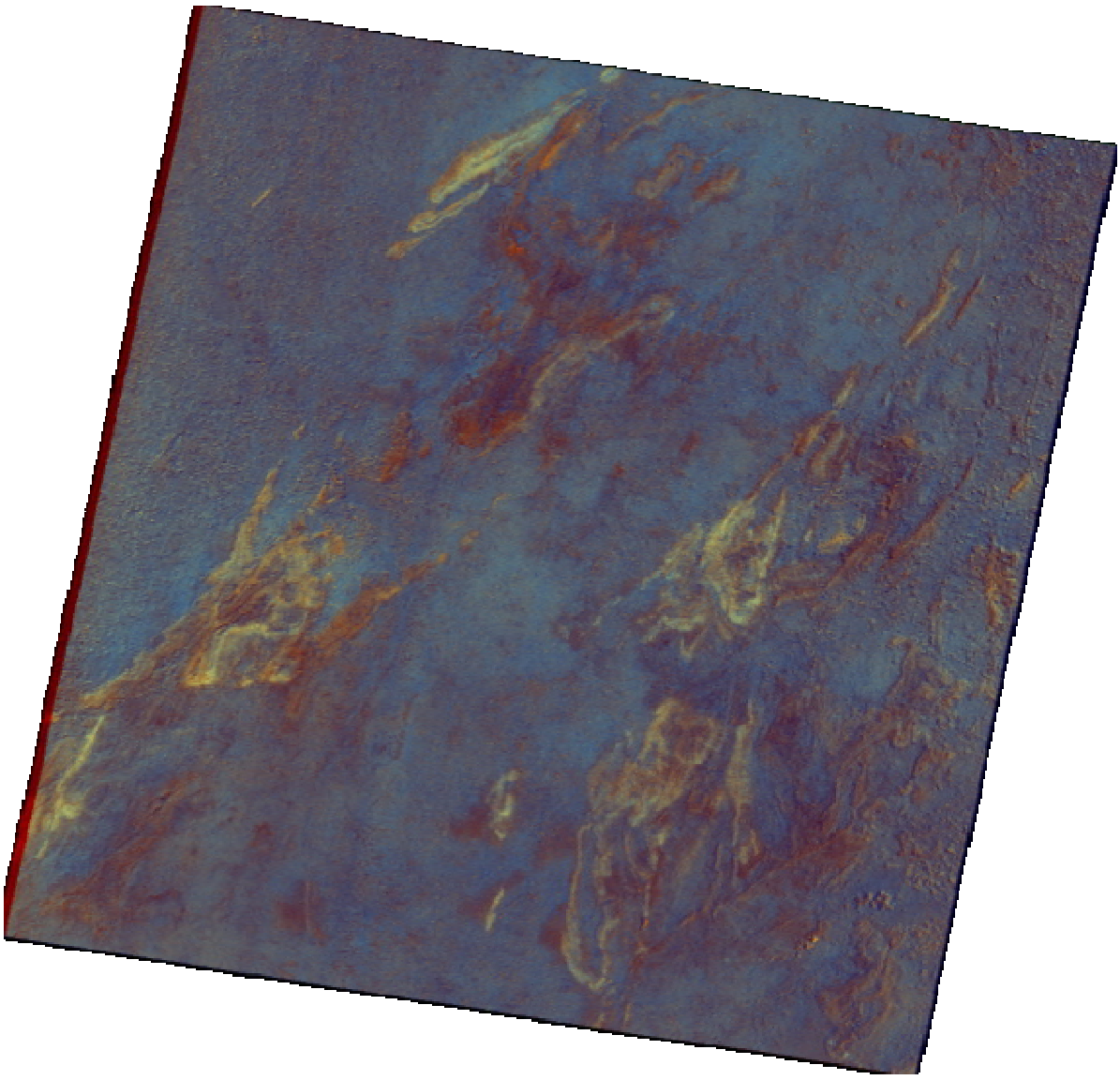

Fig. 6.23: Colour Ratio Composite of band ratios (red: 5/6, green: 7/6 and blue: 7/5) for phengitic, sericitic and kaolinitic alteration in the study area. The minerals typical of phyllic and argillic alteration are concentrated along the NE-SW trending shear zone, on both sides of the albitite zone

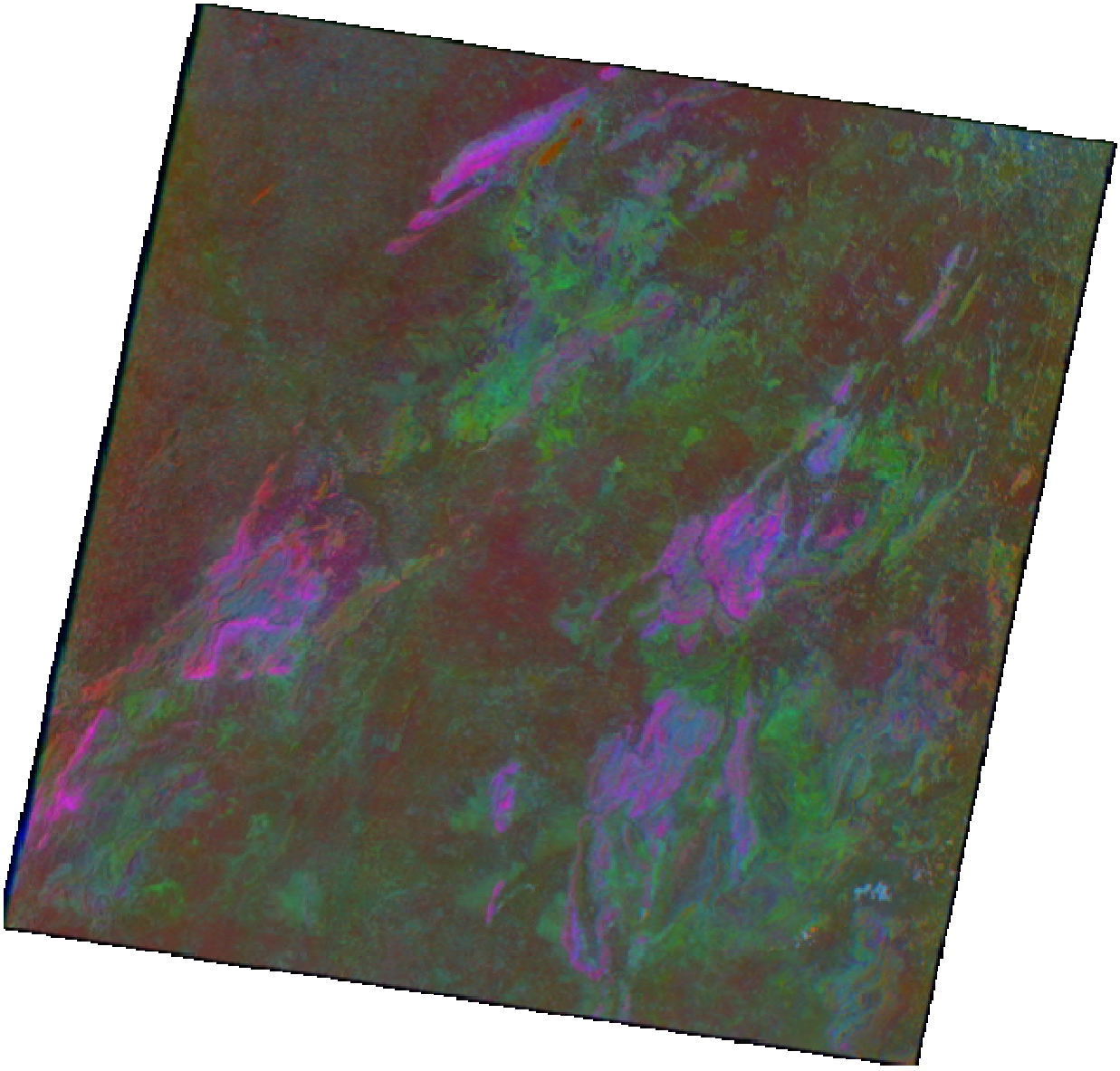

Fig 6.24: Color Ratio Composite of band ratios (red: $5*7/6^2$, green: 6/8 and blue: 4/5) for clay, amphibole and laterite alteration in the study area. Clay is mapped in red colour, amphibole in green and laterite in blue colour. Clay minerals and amphibole are concentrated along the reported shear zone. Laterite is seen adjoining the clay minerals. A laterite patch is also seen in the SE part of the image.

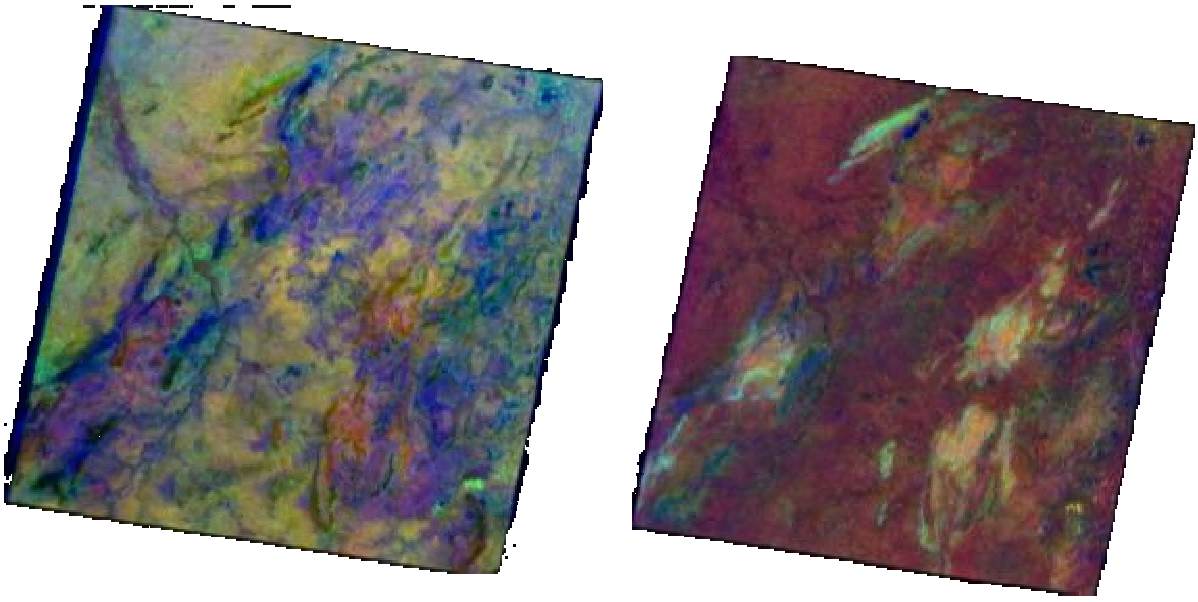

a **b**

Fig 6.25: Color Ratio Composite of band ratios a) General Lithological Mapping red: 4/1, green: 3/1, blue: 12/14 b) Gossan Alteration red: 4/2, green: 4/5, blue: 5/6.

6.3.4 Spectral Similarity Analysis for VNIR-SWIR ASTER data

To map a particular mineral, it is imperative to have a thorough understanding of its spectral signature. The nature of the spectral signature is governed by the chemical composition of the material and also on the proportion of the constituent materials (Tripathi and Rampal, 1990). The spectral signature is largely dependent on specific wavelengths, thus neglecting the contribution from remaining part of the spectrum. Feature mapping is particularly problematic for some minerals like albite which does not contained well defined absorptions. Instead of diagnostic absorptions these minerals are characterized by their continuous shapes and broad absorptions. Minerals with similar diagnostic spectral features or the ones without well defined spectral features are susceptible to mixed mapping which may lead into inaccuracies in the final mapping.

The data recorded by satellite sensor measures reflectance at surface and has no information of mineralogy at depth. Thus, even in arid areas like Khetri, the remotely sensed data will not provide much information about the mineral prospectively of the ground beneath the cover. For utilizing imaging spectrometry (hyperspectral remote

sensing) for geological applications, the information of the mineralogical composition is obtained by finding out similarity between the rock spectra and image spectra. The comparisons can be done using spectral similarity algorithms readily available in commercial off the shelf software. The spectra matching techniques allow the user to perform quantitative analysis of surface reflectance in remotely sensed data set with known diagnostic reflectance spectra of minerals (Kruse and Lefkoff, 1993).

The basic work flow for mineral identification and mapping includes various steps. The radiance data collected by the sensor is first corrected to apparent reflectance. To improve the information to noise ratio of the dataset, linear transformation is applied to minimize noise. The spectral signature of the relevant classes (reference spectra) is derived either from the library spectra or through a field work. The reference spectra are then matched with image spectra and thus the spatial mapping of the material is carried out. For the research work the main aim was to map albite rich areas in the image. For accomplishing the task, reference spectra are collected from the ground. A total number of 20 samples are collected from various locations of the ground. Out of 20 samples, 2 samples are fully albitized and 4 samples are partially albitized. The analytical spectral device Fieldspec. has been used to generate the laboratory spectra of the rock samples that have been collected from the field. The field spectra collections was undertaken within 2 hours before and after solar noon to simulate the similar illumination conditions as during the satellite pass. The spectra are resampled to ASTER wavelengths. A detailed description of the samples and reflectance spectra is provided in Chapter 5. These 6 reference spectra pertaining to samples of different degree of albitization are utilized for classification. The image was then subjected to various classification techniques. The classification methods applied are: Spectral Angle Mapper (SAM), Mixture Tuned matched Filtering (MTMF) and Spectral Feature Fitting (SFF).

6.3.4.1 *Spectral Angle Mapper*

The SAM algorithm is one of the most important and used algorithm for spectral similarity analysis. The algorithm calculates spectral similarity between the reference and image spectra. For this study the reflectance spectra has been collected using ASD spectroradiometer and then resampled to ASTER wavelengths. The spectral angle is

calculated between the reference spectra and the image derived spectra and used as a measure of similarity. The DN value of the pixel is plotted in N dimensional feature space. In this N dimensional multi (or hyper) spectral space, a pixel vector "x" has both magnitude (length) and an angle measured with respect to the axis that defines the coordinate of system of the space.

SAM algorithm works on the logic that an observed reflectance can be considered as a vector in a multidimensional space. Here the number of dimensions is equal to the number of spectral bands. Any change in the sunlight conditions result in increase or decrease of overall illumination. This in turn results in the change in length of the vector while preserving its angular orientation. Fig. 6.26 (a) shows that for any object, the vector corresponding to its spectrum lies along the line passing through the origin. The magnitude of the vector depends on the illumination, the magnitude of the vector being smaller (A) or larger (B) under low or high illumination, respectively. Fig. 6.26 (b) shows the vector for an unknown feature type (C) to a known material with laboratory measured spectral vector (D). The two features are similar if the angle between the two vectors is less than a specified tolerance value.

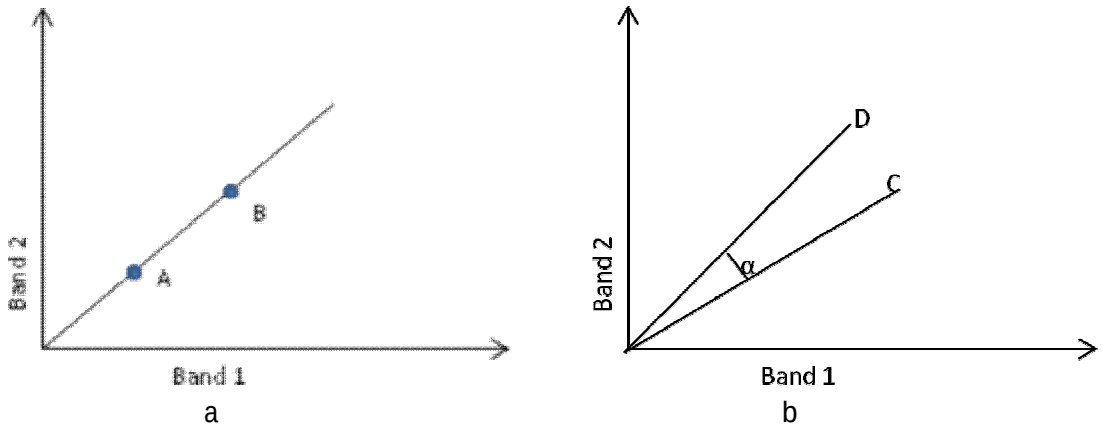

Fig. 6.26 Spectral Angle Mapping concept. (a) For a given feature type, the vector corresponding to its spectrum will lie along a line passing through the origin, with the magnitude of the vector being smaller (A) or larger (B) under lower or higher illumination, respectively. (b) When comparing the vector for an unknown feature type (C) to a known material with laboratory measured spectral vector (D), the two features match if the angle 'a' is smaller than a specified tolerance value. (After Kruse and Lefkoff, 1993)

Pixels having larger spectral angle than the specified threshold are not classified into the particular feature. The reference endmember spectra to be used for SAM classification can be taken either from ASCII files, from already existing spectral libraries, or can also be extracted directly from the image as end members.

SAM classification is applied on the ASTER reflectance image using the reference spectra collected for the field samples. The average of fully and partially albitized spectra (6 in number) are taken as the reference spectra. A maximum threshold angle of 0.08 radians was selected based on the literature review and trial and error method. A threshold angle smaller than the said value results in very less classified areas whereas a larger angle included many other areas also. Fig. 6.27 shows SAM classified image for albitite rich areas. The names of major locations in the area are given below in the Table 6.7.

Table 6.7: Major Locations in the classified image

Map symbol	Location Name	Map symbol	Location Name
1	Khetri	17	Pachlagi
2	Tonda	18	Guhala
3	Mewara Jatuwas	19	Chala
4	Mewara Gurjawas	20	Salwari
5	Basai	21	Chawki
6	Bhurwali Dhani	22	Kanwat
7	Biharipur	23	Rampura
8	Dabla	24	Khandela
9	Babai	25	Silkibara
10	Kanal ki Dhani	26	Gura

11	Lakha	27	Mahogarh
12	Chunara	28	Jhilo
13	Kushwali ki Dhani	29	Kurl ki Dhani
14	Mavanda Tarla	30	Tatia ki Dhani
15	Neem ka Thana	31	Patan
16	Sirohi		

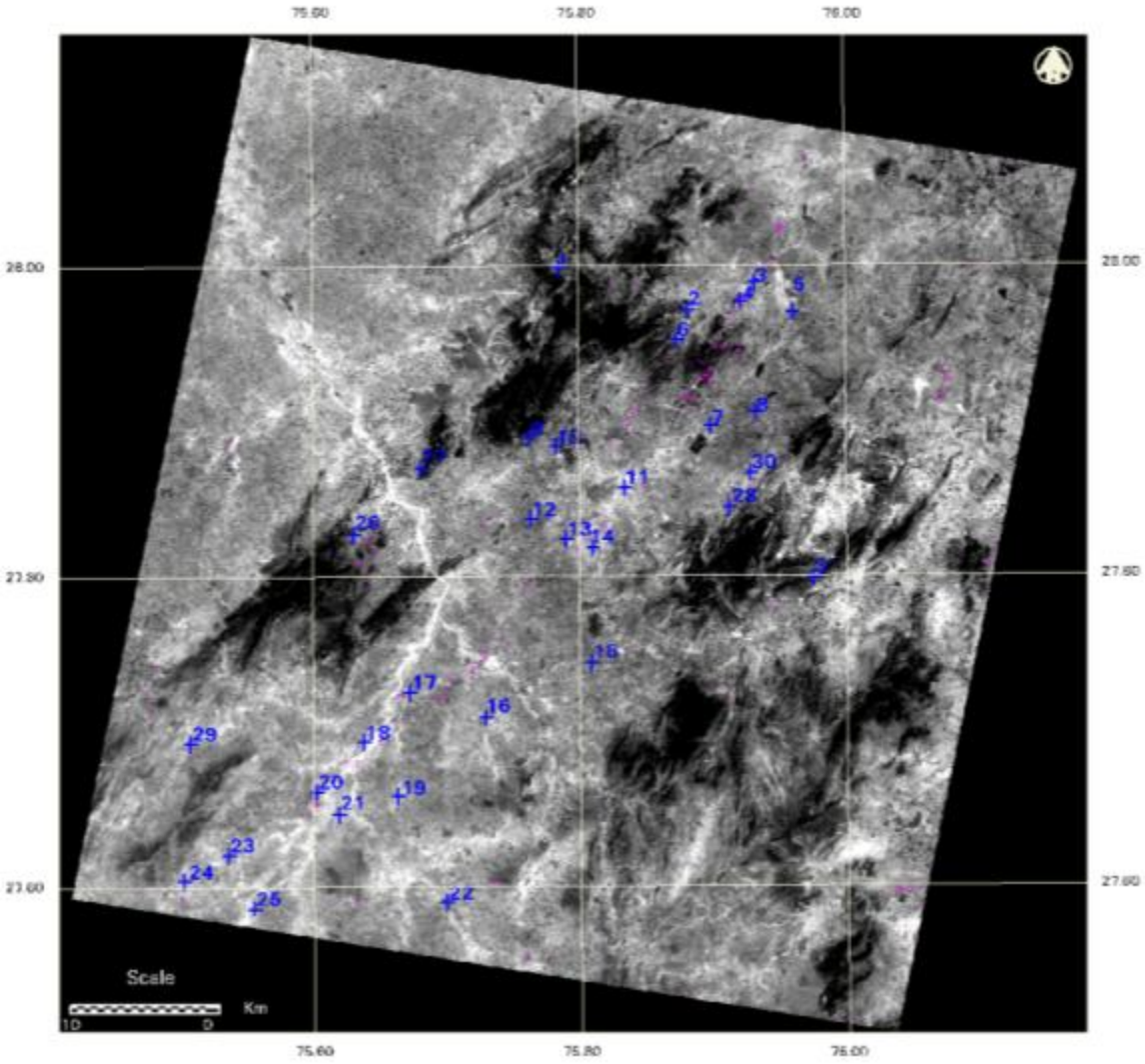

Fig. 6.27: Albitite classified area (VNIR-SWIR ASTER) - SAM classification

6.3.4.2 *Mixture Tuned matched Filtering*

The classification algorithm for MTMF suppresses background noise and gives an estimate of single target abundance by using a partial unmixing method. The MTMF method works in three stages: first a minimum noise fraction (MNF) transformation of apparent reflection dataset is calculated (Green *et al.*, 1988). The MNF output image is then subjected to matched filtering for estimating abundance of material. Finally mixture tuning is carried out to identify infeasible or false-positive areas (Boardman, 1998). MTMF technique finds out the abundance of reference spectra in the image. The technique focuses on maximizing the response of known endmember and also suppressing the response of the unknown background. The result of mixture tuned matched filtering is a set of grey scale images. The value of these grey scale images range from zero to one. These images provide a degree of matching between the reference and the image spectra. The score zero indicate a complete mismatch between the reference and the image spectra while score one indicate total match between the two. Intermediate values in the score image represent varying degree of matching. The false positives may sometimes occur when using matched filtering (Fig. 6.28). MTMF also generates an infeasibility image as output. The number of false positives reduces significantly if infeasibility image is used. Pixels with a high infeasibility are likely to be matched filter false positives. A low value of infeasibility and matched filter score higher than background distribution around zero will indicate correctly mapped pixels. The infeasibility values calculated is in noise sigma units which vary according to matched filter score. MTMF algorithm is a reliable and fast method of individual mineral identification based on the match score between the reference and image spectra. The technique can also work for single material and does not require the knowledge of all the materials within the image scene.

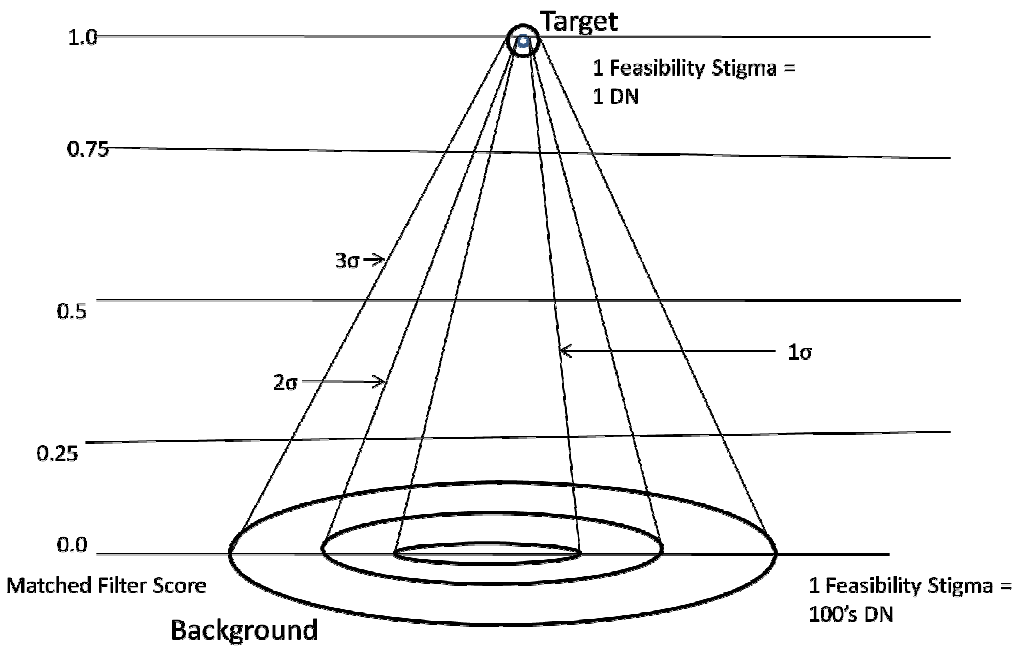

Fig. 6.28: Diagram Showing Mixture Tuned Matched Filtering Technique

MTMF classification is applied on ASTER image. To start with a MNF transformation is carried out on the original image. The lab spectra of the albitized samples is selected and score and infeasibility images are generated for albitite. The score and infeasibility are generated. Pixels having high match score and low infeasibility value are selected as albitite pixels. Fig. 6.29 shows the results of MTMF classification on ASTER band 1 image. The names of major locations in the area are given in the Table 6.7.

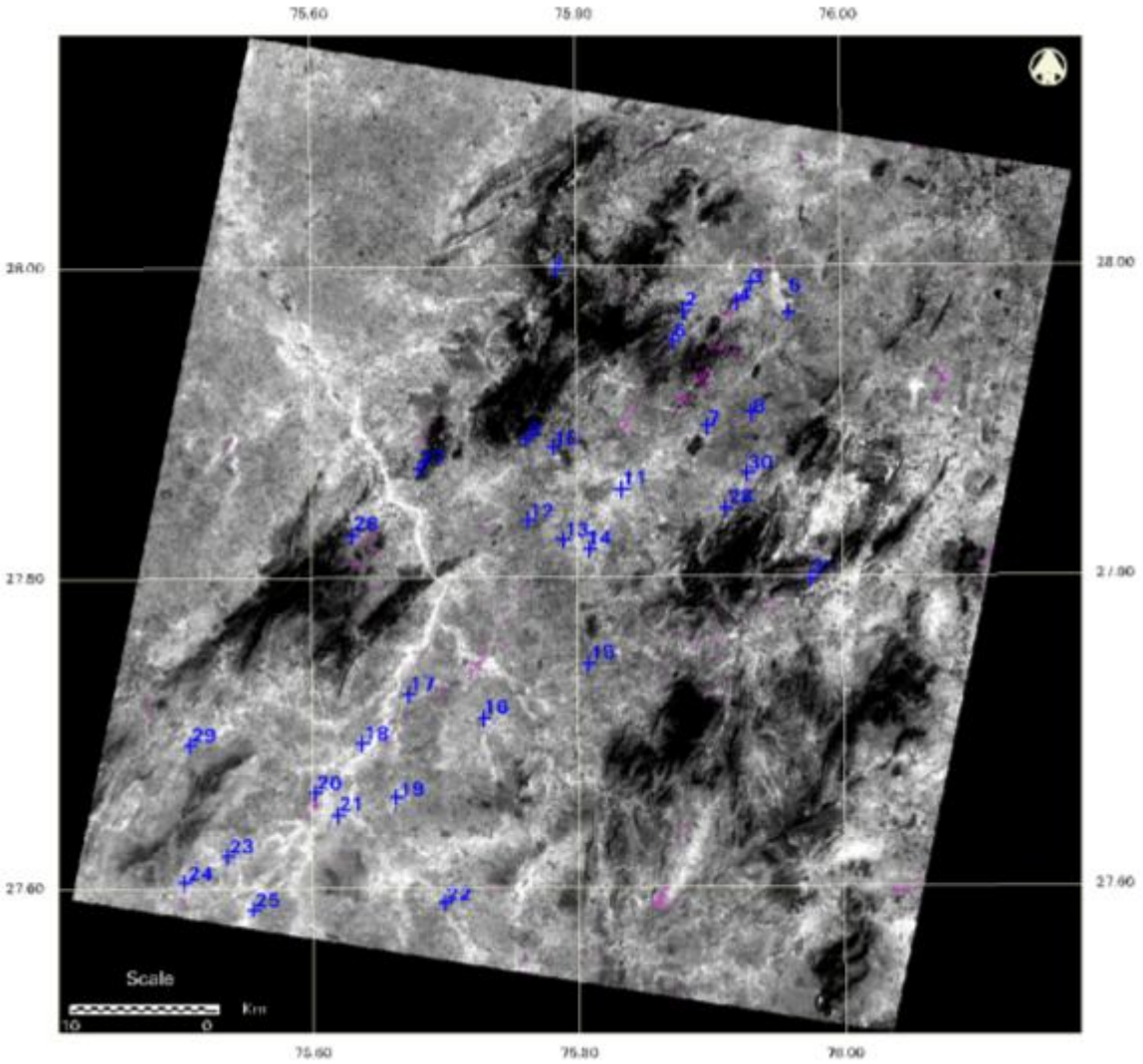

Fig. 6.29: Albitite classified area (VNIR-SWIR ASTER) - MTMF classification

6.3.4.3 *Spectral Feature Fitting*

Most classification methods used for material identification do not directly identify specific materials. They only have a tendency to indicate the similarity and uniqueness of a material with respect to another known material. For identifying the materials directly from a remotely sensed image, specific spectral features are to be extracted from field and laboratory reflectance spectra. This is in practice since last many years (Green and Craig, 1985; Kruse *et al.*, 1985; Yamaguchi and Lyon, 1986; Clark *et al.*, 1990). Now days such information is applied to hyperspectral data for geologic applications (Kruse, 1988; Clark *et al.*, 1992, 1993, Clark, 1999). For such spectral analysis of the data, the

data needs to be reduced to reflectance and continuum should be removed. A continuum is a mathematical function which can be utilized to enhance and take out isolate a particular absorption feature (Kruse *et al.*, 1985; Green and Craig, 1985). A background signal without having a relation with the specific absorption feature of interest is used for continuum removal. A continuum is created using local maxima of the spectrum and then by fitting straight line segments between these points. The spectra are normalized to this continuum. The continuum is now removed by dividing it into the original spectrum (Clark *et al.*, 2002). Spectral Feature Fitting available in ENVI is based on this algorithm. Spectral feature fitting starts with the specification of range of wavelengths which contain the unique absorption feature for the specific target. The depth of the absorption feature for target and reference spectra as well as shape of the absorption feature are measured to check the similarity between the two spectra. For SFF algorithm the reference spectra could be selected either from the spectral library or directly from the image. The continuum is removed both from the reference and unknown spectra. The reference end member is scaled to match the unknown spectra. For each end member the continuum removed spectra is subtracted from unit value resulting in inverting them and continuum made to zero. This results in a scale image. Then a single multiplicative scaling factor is calculated to match the reference spectra to the unknown spectra. Assuming that a considerable spectral range was selected, a large scaling factor represents a deep feature, while a small scaling factor indicates a weak spectral feature. A least square fit is calculated band by band between the reference end member and the unknown spectra. An RMS image is created for each end member by summing up the total root-mean-square (RMS) error. A ratio between the Scale and RMS is a measure of matching between the unknown and the reference spectrum on a pixel-by-pixel basis and can be visualized a "Fit" image.

The reference spectrum for albitite collected from the field samples are used for classification. The continuum was removed from the reference spectrum and the image. Since the albitite has weak spectral feature, thus a small scaling factor was selected. On the scatterplot scale values 0.2, and RMS values less than 0.04 are selected for albitite. Fig. 6.30 shows the RMS and scale image Fig. 6.31 shows the albitite classified areas using SFF algorithm. The names of major locations in the area are given in the Table 6.7.

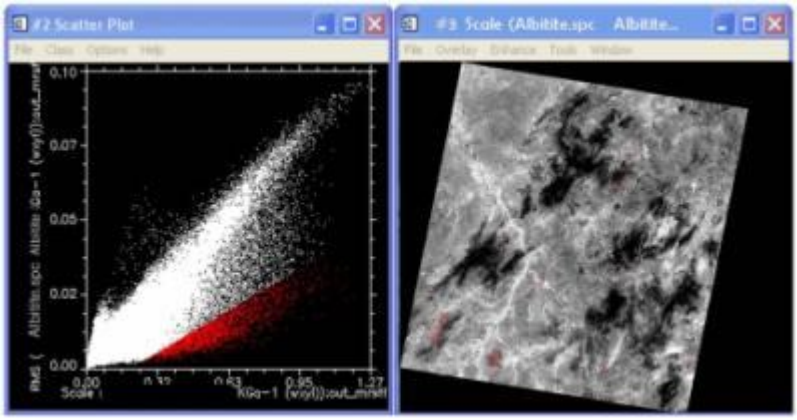

Fig. 6.30: RMS and Scale images for Albitite

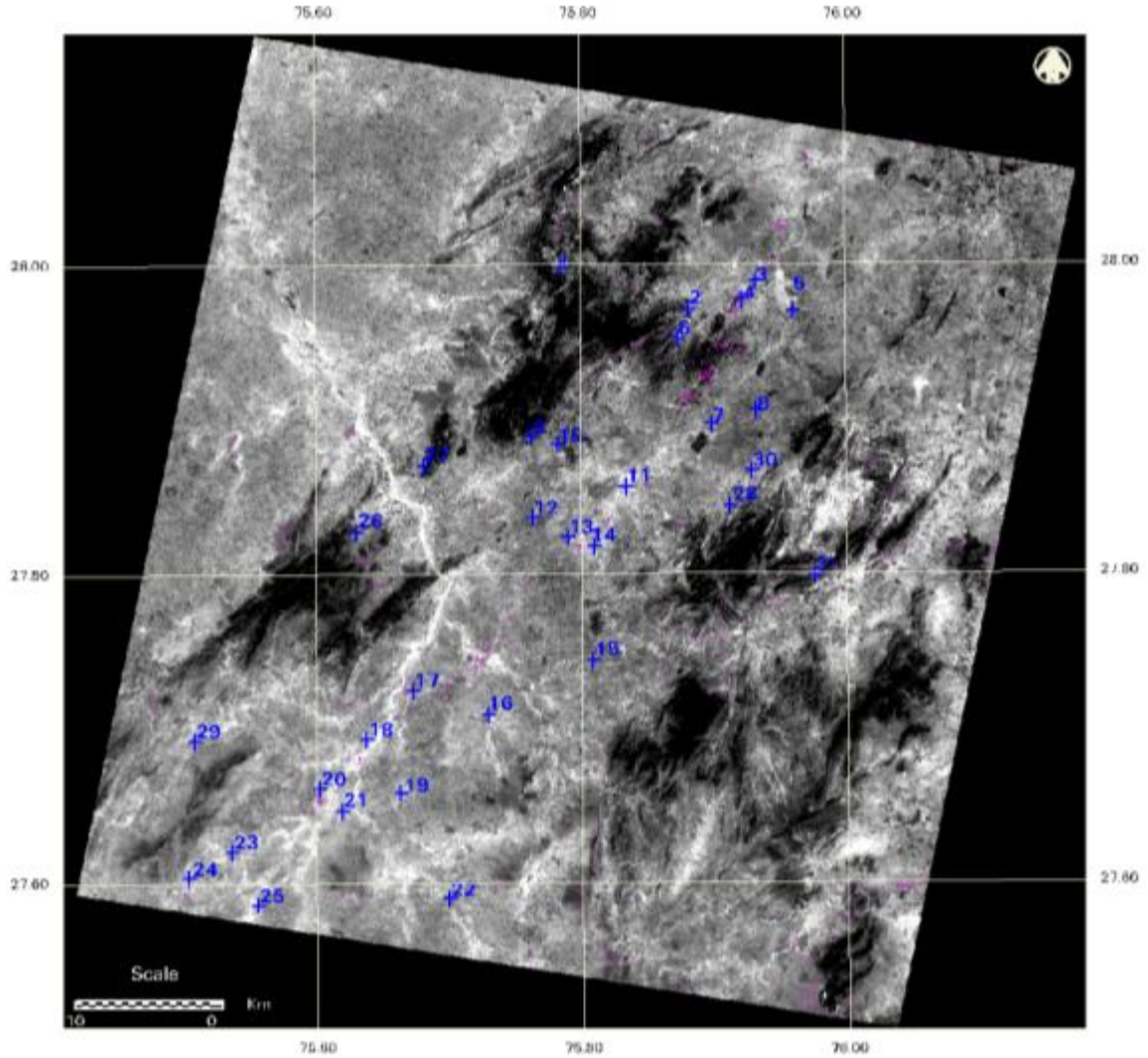

Fig. 6.31: Albitite classified area (VNIR-SWIR ASTER) - SFF classification

6.3.5 Spectral Similarity Analysis for TIR ASTER data

Most of the important rock-forming silicate minerals have their diagnostic spectral features in the TIR region (7.0-14.0 μm) (Lyon, 1965; Hunt and Salisbury, 1970a, 1970b). Feldspar minerals have a very strong absorption at around 8.6 μm (ASTER band 11), and as a result, exhibits lower emissivity in band 11 than in bands 10 and 12. (Ninomiya *et al.*, 2005). Analysis of the spectral properties of albite minerals obtained from the ASTER spectral library (Baldridge *et al.*, 2009) showed that, albite reflectance curve is nearly flat in VNIR and SWIR regions of electromagnetic spectrum. In TIR range albite spectrum shows higher values in bands 12, 13 and 14 than in bands 10 and 11 (Fig. 6.4).

The 5-band atmospherically corrected ASTER TIR data, has been processed using a hierarchical method as provided within the ENVI software. There are two major steps involved in the spectral processing selection of the spectral end-members, and applying the suitable classification algorithm for spectral mapping.

Since the spectral data for the collected rock samples was generated with Field Spec Pro. which collects the spectral reflectance curve in the range from 0.4 – 2.5 μm. Thus the spectral library collected was not valid for TIR bands. For classification of albitite using TIR bands, the field locations of the collected samples are utilized. The end members are collected at the specific locations of field samples. These end members are subsequently used for the classification.

Three classification algorithms are applied for identification of albitite zone in the study area viz. SAM, MTMF and SFF. The salient features of the classification algorithms have been explained in section 6.3.4. Fig. 6.33, 6.34 and 6.35 depicts the results of the classification of TIR bands using various classification algorithms. The names of major locations in the area are given in the Table 6.7. The results are discussed in detail in chapter 7.

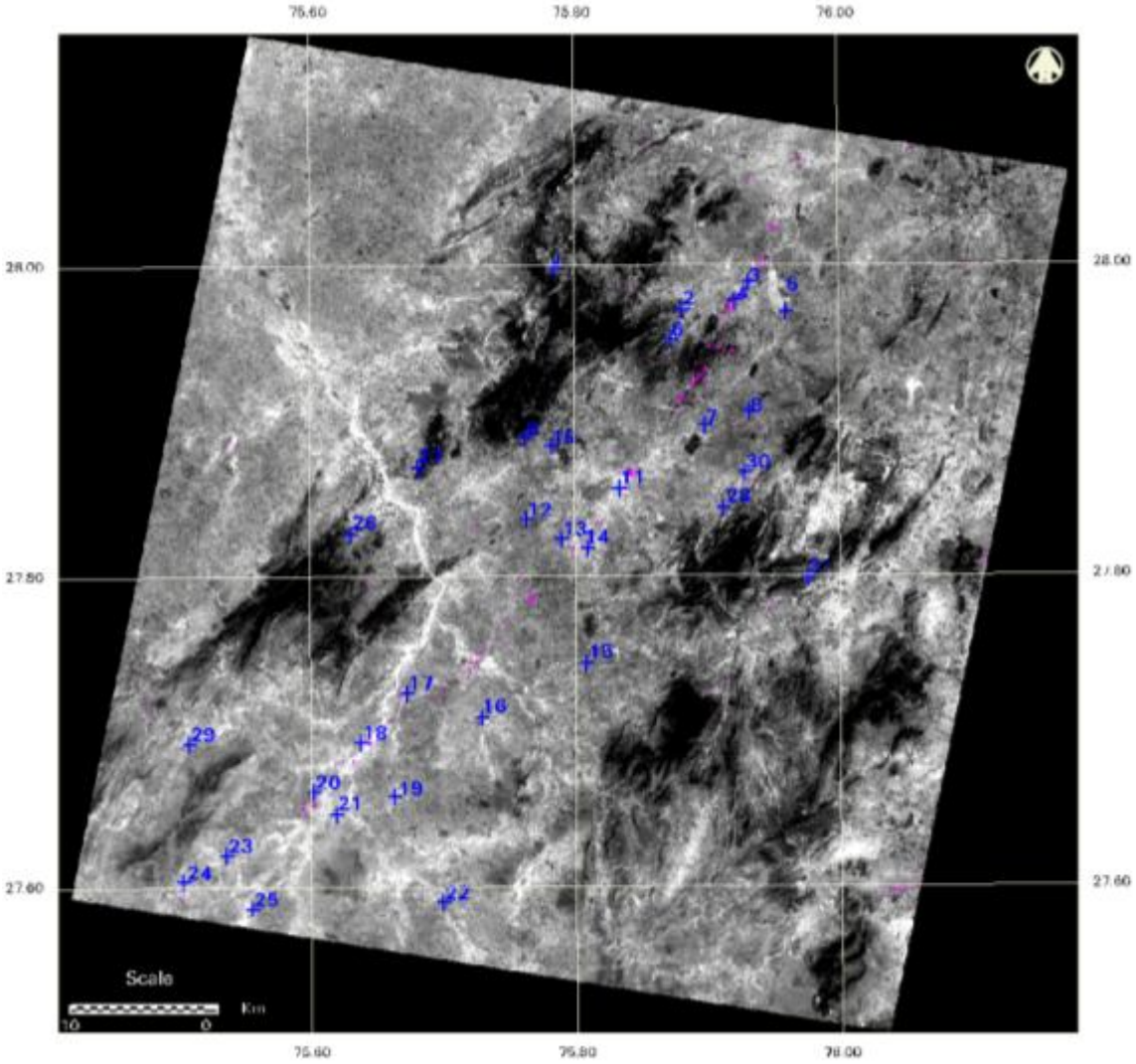

Fig. 6.33: Albitite classified area (TIR ASTER) - SAM classification

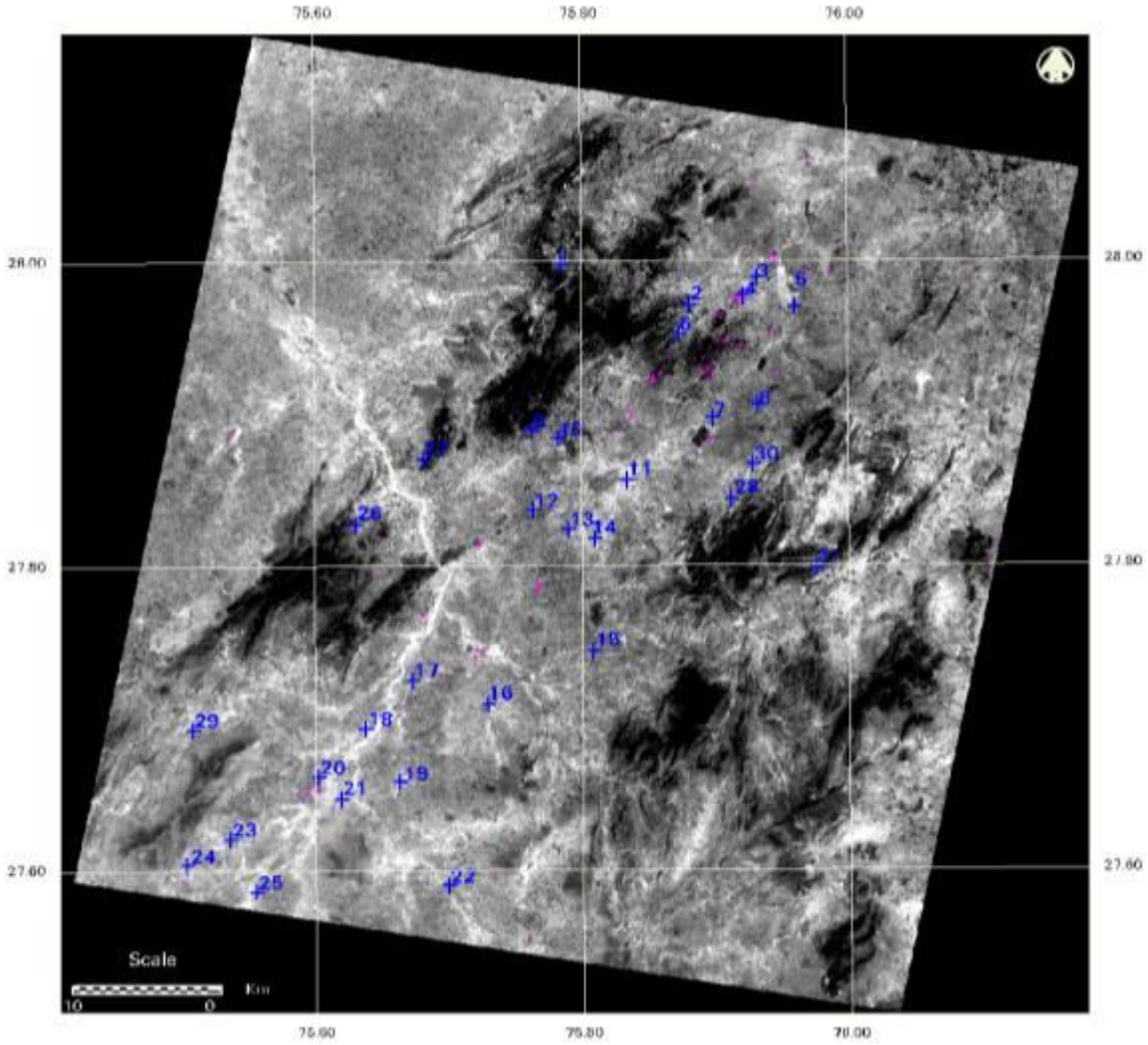

Fig. 6.34: Albitite classified area (TIR ASTER) - MTMF classification

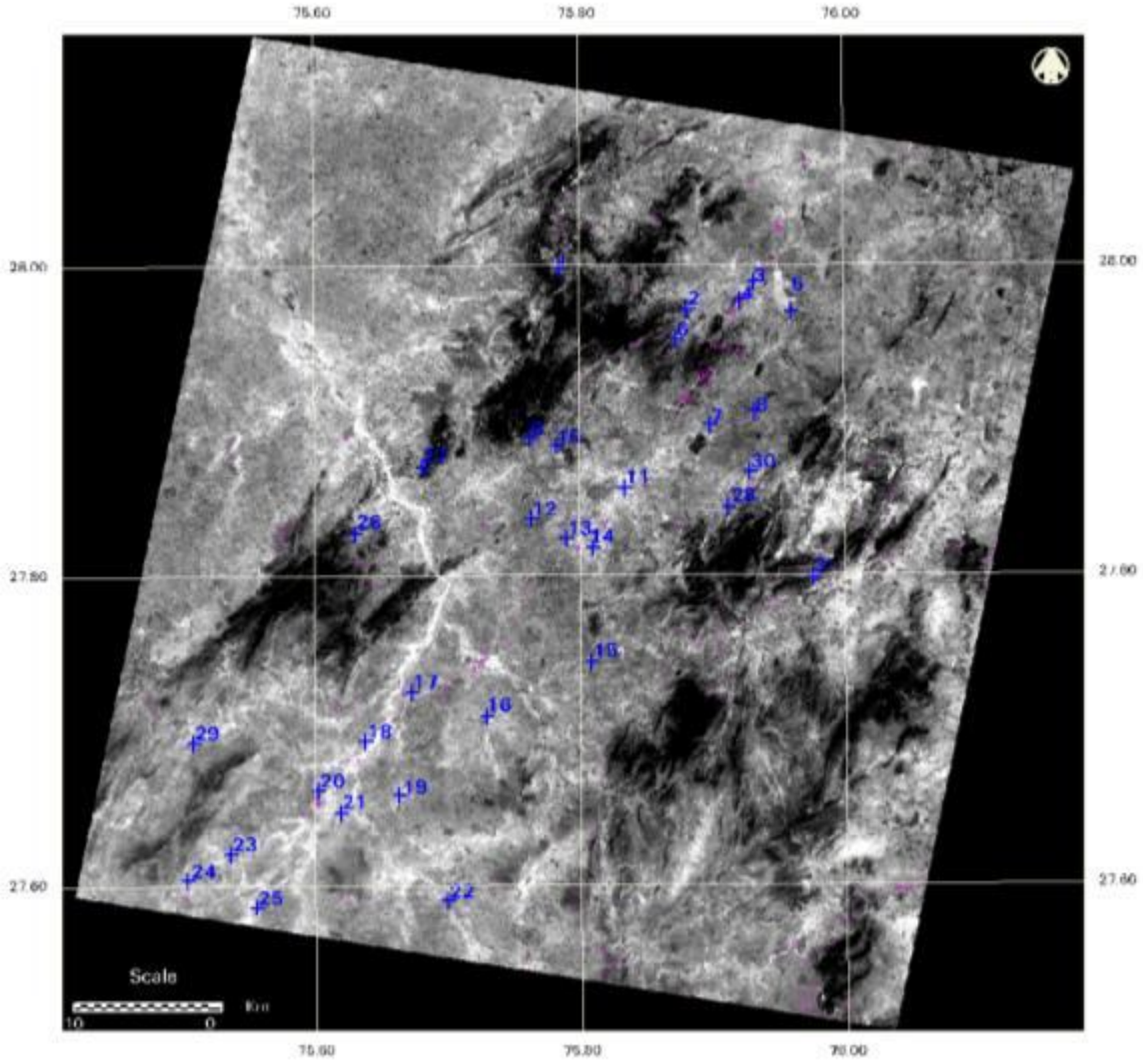

Fig. 6.35: Albitite classified area (TIR ASTER) - SFF classification

CHAPTER 7

SYNTHESIS OF RESULTS AND INTERPRETATION

In order to assess the usefulness and credibility of the research work carried out, it is necessary to analyze them in light of existing field and laboratory evidences as well as the documented literature about the study area (Gupta *et al.*, 2000). Remote sensing based analysis for mineral mapping is governed by several factors at every stage of the image analysis. These include proper selection of the problem in the study area, thorough understanding of the geological processes that led to the present lithology, proper selection of the remote sensing and ancillary data, effective preprocessing which provides good comparison between the image spectra and field spectra and a proper processing which generates results that match with the collateral information available.

This chapter, therefore, attempts to synthesize the results of image analysis contained in previous chapters and interprets them in a geologically meaningful way. In nutshell, the main focus of this chapter is to describe the results of satellite-based spectral analysis for mineral mapping and specifically albitite mapping through a comparative analysis of well-described geology, field locations and laboratory data and their representation on the respective spectral maps. The main aim of the research was to explore the utility of multispectral and hyperspectral remote sensing datasets for discriminating albitite zone in KCB area and to demarcate the albitite zone in the study area. A number of image analysis operations have been carried out on the Landsat and ASTER data. This chapter summarizes the results obtained for every step of methodology. Limitations arising due to spatial and spectral resolution inadequacies, atmospheric and topographic correction inaccuracies, and spectral mixing have been discussed at appropriate places.

7.1 DATA PREPROCESSING: CORRECTION OF ATMOSPHERIC EFFECTS

Before the data can be used for detailed spectral analysis, it is vital to compensate for the radiometric, atmospheric and topographic influences on the target radiance reaching the remote sensor. Atmosphere selectively absorbs and scatters the solar radiation in different wavelength regions. The main topographic effects are in the form of differential terrain illumination and terrain adjacency effects.

Sensor calibration is necessary to convert the digital number (DN) values of the image to the units of at-sensor radiances. In the shorter wavelength VNIR region, the atmospheric scattering is the dominant mode of atmospheric influence on the radiances recorded by the remote sensors; this effect is primarily additive in nature. On the other hand, in the SWIR region, the main atmospheric effects are in the form of atmospheric absorption, which are characteristically multiplicative in nature. Data preprocessing involves removal of these atmospheric influences such that an estimate of the true target radiance and reflectance (in the solar reflective VNIR-SWIR region), can be made.

A number of methodologies have been developed in previous years to address this objective. These have been grouped under relative and absolute atmospheric correction methods. Relative methods are generally scene based, with no external inputs and include such methods as Log Residuals (LR). Flat Field (FF, and Modified Flat Field, MFF), Internal Average Relative Reflectance (IARR), etc.; whereas, the absolute methods are based on the physical laws of radiative transfer and commonly require external inputs in the form of local atmospheric data, and include various radiative transfer codes (RTCs) such as MODTRAN (Moderate Resolution Atmospheric Radiance and Transmittance) and 6S (Second Simulation of the Satellite Signal in the Solar Spectrum), and the image-based Dark Object Subtraction (DOS) technique.

Preprocessing the ASTER VNIR-SWIR has involved application of the known methods of atmospheric correction to select the best correction. The methods of relative atmospheric correction applied include Log Residual, Flat Field, Modified Flat Field and Internal Average Relative Reflectance. The absolute atmospheric correction has been attempted using the FLAASH, and ATCOR program. Comparison of the corrections has been done by plotting the pixel spectra of a flat homogeneous surface within the image after application of various atmospheric correction procedures, and examining the plots

with reference to the JHU library spectrum of urban settlement. It was observed that the relative atmospheric correction methods are unable to

The ATCOR and FLAASH corrected spectra for the sample pixel has a close match with lab spectrum, except for band 1, 2 and 4. For bands 1, 2 and 4 the reflectance is low in ATCOR corrected image while reflectances are higher for other bands. FLAASH extracted spectra also exhibit similar trend but the difference from reference spectra is less. Both ATCOR and FLAASH display high reflectance values in SWIR bands of ASTER. Because ASTER Level 1A bands are not co registered, one cannot directly input the VNIR or SWIR data sets into FLAASH. Thus 'Layer Stacking' tool was used to combine the visible near-infrared (VNIR) and shortwave infrared (SWIR) bands into a single data set to input into FLAASH.

Best correction has been observed in case of FLAASH-corrected image spectrum. FLAASH Calibrated ASTER (converted from DN value to reflectance) are used and processed spectrally for albitite mapping. The thermal atmospheric correction tool was utilized for atmospheric correction of thermal bands.

7.2 SATELLITE DATA PROCESSING FOR ALBITITE MAPPING

One of the primary advantages of ASTER over ETM+ data is the improved resolution of the important SWIR region (2.0-2.5 μm) where the diagnostic signatures of the main minerals are present. In place of single broad bands in SWIR (2.08-2.35 μm) and TIR (10.4 - 12.5 μm), ASTER records data in 5 strategic bands in the SWIR (2.0-2.5 μm) and 5 bands in TIR (8.125 – 11.65 μm) wavelength region. This makes the ASTER data of special utility in mapping of minerals related with most kinds of mineralizing environments.

The primary objective of this study has been mapping of minerals using satellite data. Towards this end, the composite 14-band ASTER VNIR-SWIR-TIR reflectance data obtained after the atmospheric correction has been processed using various image processing techniques to uniquely identify and map the surface/alteration minerals present in the study area. The processing has been designed to exhaustively evaluate the potential of methods from simple to advanced, in extracting usable mineral information from the remote sensing data. The processing flow has been designed such that it

hierarchically grows from a simple level of processing involving image enhancement and color display of 3-band composites, to image transformation (DCS, PCA and DPCS), band ratioing and spectral indices

Based on the optimum index factor (OIF) approach, two band combinations have been selected - ASTER bands 6-3-1, for the 9-band VNIR-SWIR combined dataset, having enhanced discrimination of Fe-O and OH altered areas; and ASTER bands 4-6-8, for the SWIR dataset, displaying the distribution of Al-OH and Mg-OH bearing surfaces, respectively showing clay/muscovite and chlorite/carbonate alterations. Improved color discrimination for the above band composites and the respective mineralogical and alteration information has been obtained using the decorrelation stretch processing. Spectral indices based on the ASTER bands have been prepared to map the distribution of clay, amphibole, laterite, phengitic, sericitic, kaolinitic and gossan alteration. It has been observed that most of these minerals are concentrated within the main shear zone passing through the study area, as well as in the feldspathic quartzites.

Crosta processing has been used to distinguish and map the distribution of minerals with spectral features in the SWIR and TIR region. Surficial maps for albite, epidote, calcite, chlorite and kaolinite have been prepared through the crosta procedure.

7.3 SPECTRAL PROCESSING OF ASTER DATA

Full spectral processing of the VNIR-SWIR reflectance dataset has been carried out to uniquely identify and map the albitite rich areas based on their spectral shape and absorption features.

The reference spectra were collected from the samples collected from the ground. In order to expand the size of end-member spectral classes so that the diverse spectral categories present within the area are brought out more representatively, a total of 6 samples pertaining to various stages of albitization were utilized for the classification purpose. Spectral Angle Mapper (SAM), Mixture Tuned Matched Filtering (MTMF), Spectral Feature Fitting (SFF) was used to identify and map albitite in the study area.

Spectral processing of the atmospherically corrected ASTER TIR data has been carried out to identify the albitite rich areas based on their unique spectral features. The end members to be used for classification were collected from the image itself. The spectral

curve of the pixels at the sample site collection location was utilized as end members. All the six sample sites representing various stages of albitization were used for end member generation. The image was classified using Spectral Angle Mapper (SAM), Mixture Tuned Matched Filtering (MTMF), Spectral Feature Fitting (SFF) algorithms. The results of the three classification methods have been described in chapter 6.

From the classified results of VNIR –SWIR data and TIR data it is evident that though the albitite identification is more accurate with TIR data, however albitite is identified in few areas with VNIR-SWIR bands. Hence a combined use of ASTER VNIR-SWIR and TIR data enable optimized discrimination of specific minerals because of the complementary nature of information from the thermal and shorter wavelengths. Thus to identify and demarcate albitite zone, both the classified results were merged. The overall area classified as albitite is given in table 7.1.

Table 7.1: Area Statistics for Albitite with ASTER data

Algorithm	**Albitite Area (hectares)**
Spectral Angle Mapper	672.13
Mixture Tuned Matched Filtering	1015.98
Spectral Feature Fitting	1097.57

Surficial albitite map was generated, which depicts the spatial distribution of the albitite in the study area. The visual inspection of the three classified images indicate that major patches of pixels corresponding to class albitite are occurring follow a linear pattern trending NE-SW. However there are also few random pixels classified as albitite. A concentrated occurrence of albitite to east of Khetri in Mewra Gurjawas area is observed. Another massive occurrence of albitite is identified to the south west of Mewra Gurjawas near Guhala. The classified image exhibits most patches of albitite falling in a narrow band and exhibiting a linear trend. Though some scattered patches are also classified. Here it is observed that SAM classified image exhibit lesser random pixels than both MTMF and SFF classified image. Though the results look excellent visually, still a through statistical accuracy assessment needs to be performed.

7.3.1 Accuracy Assessment for ASTER Classification

In order to assess the usefulness and credibility of the results of albitite mapping, it is necessary to analyze the results in light of existing field and laboratory evidences. The results of ASTER-based albitite mapping have been synthesized and interpreted in a geologically meaningful way through a comparative analysis of well-described geology, field locations, and laboratory petrographic constituting the ground-truth, and their corresponding representation on the respective spectral maps. For performance analysis of classification, the classified images were analyzed using reference data from the reported albitite occurances referred in various scientific publications. Apart from the six locations of sample collection for albitite, eleven occurances of albitite is reported in various scientific publications, viz Khandela, Guhala, Maonda, Sior, Salwari, Lakha, Pachlangi, Karoth Dhanian, Banjaron Ki Dhani, Sagdu Ki Dhani and Saladipura (Jain *et al.*, 1999; Ray, 1987; Ray and Ghosh, 1989; Ray, 1990). Fig. 7.1 shows the reported occurances of albitite in red color and sample sites in yellow color.

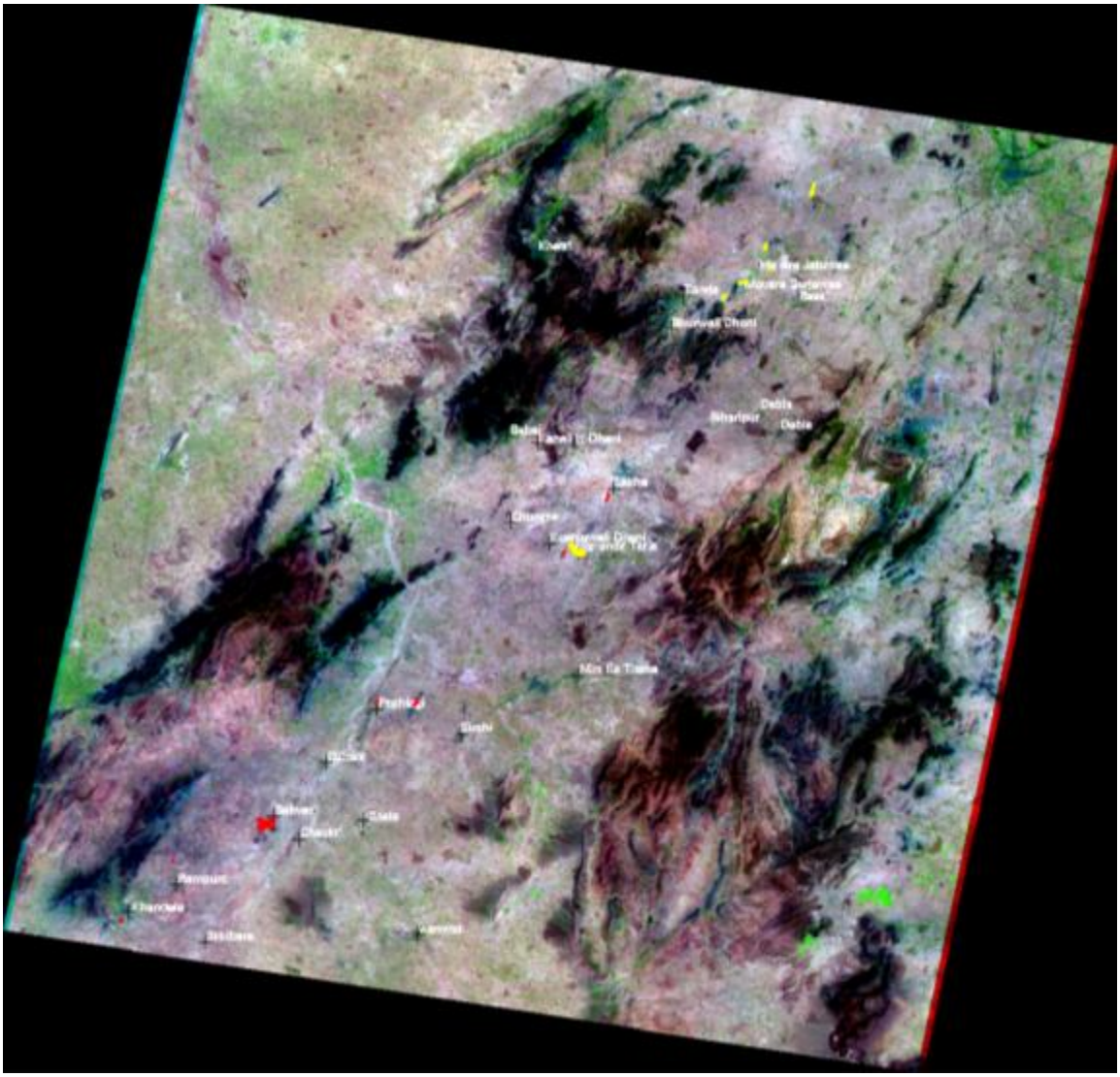

Fig. 7.1: Reported Albitite Occurances and Sample Sites

It was observed that for Khandela, Guhala, Maonda, Salwari and Banjaron Ki Dhani all the three algorithms are able to identify albitite. SAM failed to classify albitite at Pachlangi and Sagdu Ki Dhani. MTMF is unable to distinguish albitite from host rocks at Lakha, Pachlangi and Saladipura while with SFF surface outcrops of albitite at Karoth Dhanian and Sior, are not identified. Table 7.2 summarizes the accuracy of various classified results.

Table 7.2: Accuracy Assessment of ASTER classified products

S.No.	Area of Occurrence	Classified Output		
		SAM	**MTMF**	**SFF**
1	Khandela	Y	Y	Y
2	Guhala	Y	Y	Y
3	Maonda	Y	Y	Y
4	Sior	Y	Y	N
5	Salwari	Y	Y	Y
6	Lakha	Y	N	Y
7	Pachlangi	N	N	Y
8	Karoth Dhanian	Y	Y	N
9	Banjaron Ki Dhani	Y	Y	Y
10	Sagdu Ki Dhani	N	Y	Y
11	Saladipura	Y	N	Y
	% Accuracy	**81.81%**	**72.72%**	**81.81%**

The above table indicates that SAM and SFF algorithm are giving maximum accuracy of 81.81% and are able to distinguish albitite form other classes in the study area. MTMF is able to achieve an accuracy of 72.72% by using ASTER data for classification. But visual inspection of the classified results indicate that there are many random pixels classified as albitite in MTMF and SFF algorithm whereas SAM results have less random patches. Ambiguities and differences in albitite identification for different algorithms investigated have arisen primarily because of limitations of ASTER's spectral resolution resulting in multiple (and sometimes erroneous) matches of the pixel spectrum with reference spectra. Also, residual effects of vegetation within an average pixel area of 30x30 m^2 also adds to the difficulty in exaction and identification. The results show that the ASTER data can provide fast and dependable support in identifying and mapping albitite which

can be linked with the presence of economic mineralization especially uranium mineralization.

7.3.2 Identification of Albitite Zone

The final aim of the study was to identify and mark the spatial extent of the albitite zone in the study area and to match it with available collateral information.

To achieve the objective an albitite abundance map was generated from the classified image. The abundance map represented the spatial concentration of albitite. A 3x3 spatial convolution filter was applied pixel by pixel on the entire image. The filter counted the occurrences of albitite in the central pixel and adjoining eight pixels. In the classified image random pixels which are not useful, they can be filtered out according to their sizes. This is sometimes referred to as eliminating the salt and pepper effects, or sieving. The abundance map filters out the random pixels classified as albitite and only big chunks of pixels are left out. The abundance range was generated for filtering out random pixels. Table 7.3 shows the range selected for mapping albitite abundance in the study area.

Table 7.3: Albitite Abundance Range

S.NO	Albitite Pixel count	Albitite Abundance Range
1	9	Very High Abundance
2	7-8	High Abundance
3	5-6	Medium Abundance
4	3-4	Low Abundance
5	1-2	Very Low Abundance
6	0	Zero Abundance

The abundance map for all the three classified outputs were generated. Fig. 7.2 shows the abundance map of SAM classified data with an enlarged area.

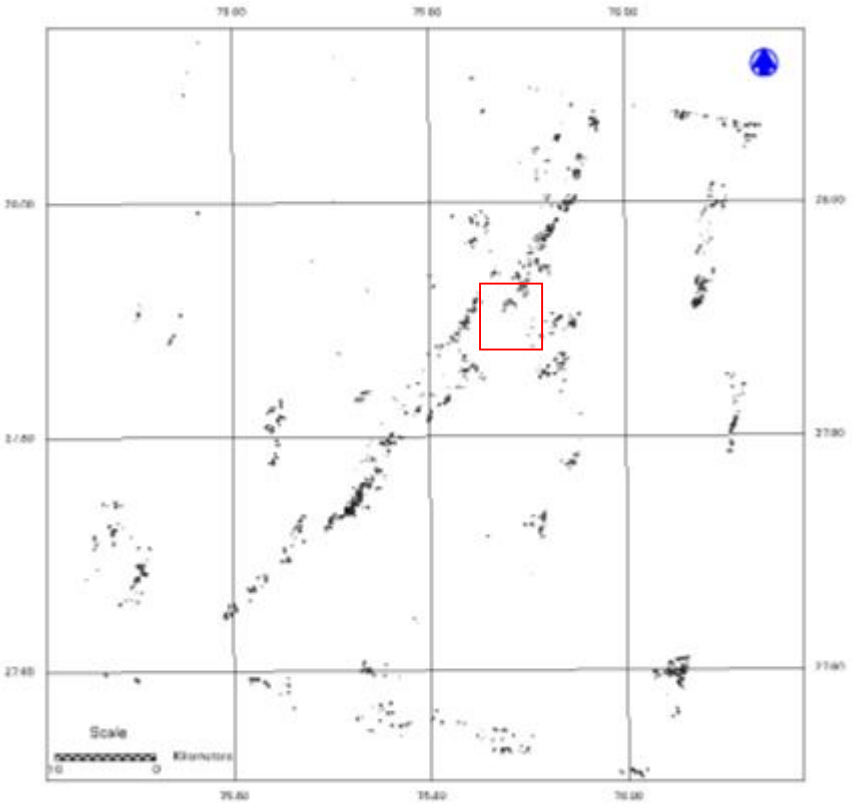

Fig. 7.2 a: Abundance Map of SAM Classified Data

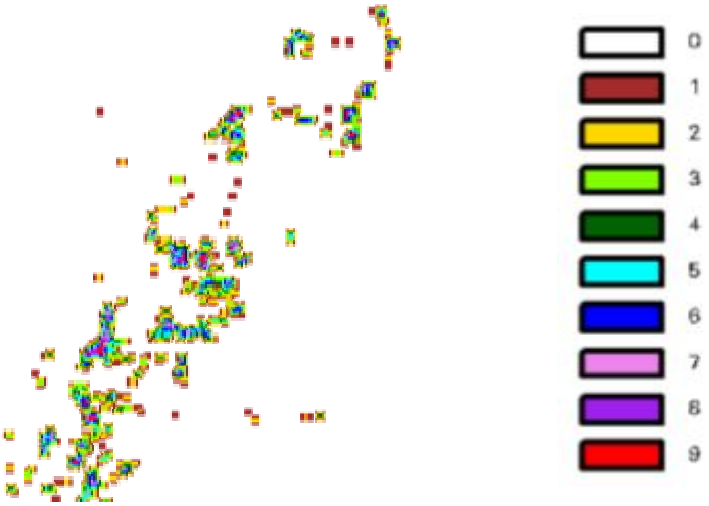

Fig. 7.2 b: Zoomed view of abundance map with abundance range

To demarcate the albitite zone, the abundance values were plotted against the longitudinal axes. Since the image contained extremely large number of points (more than 1 lakh), the abundance image was first degraded to lower resolution. The degraded

image of the three classification methods was plotted against respective longitudinal coordinates. The coordinates were reprojected into Universal Transfer Mercator, so as to get albitite zone extent in meters. A grid based analysis to demarcate the albitite zone boundary was carried out. A latitudinal slicing at regular interval of 500 m was done. Each 500 m grid was then subjected to statistical analysis. For every rectangular image slice, the longitudinal coordinate of the image was plotted against abundance values ranging from 0-1. Fig. 7.3 depicts the abundance values plotted versus longitudinal coordinates for SAM classified image.

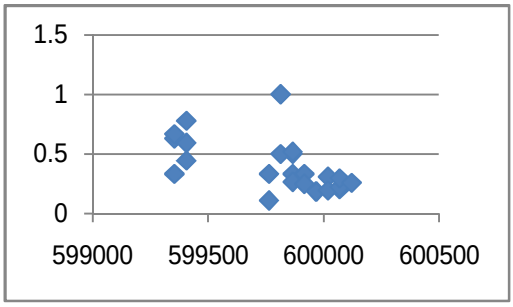

a (3040001 N – 3045000 N)

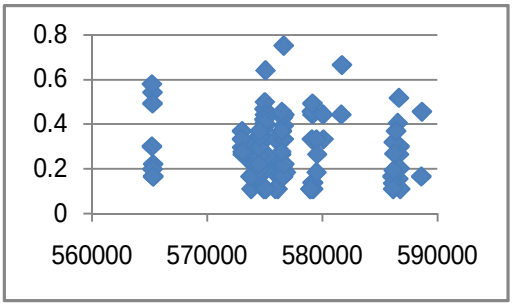

b (3045001 N – 3050000 N)

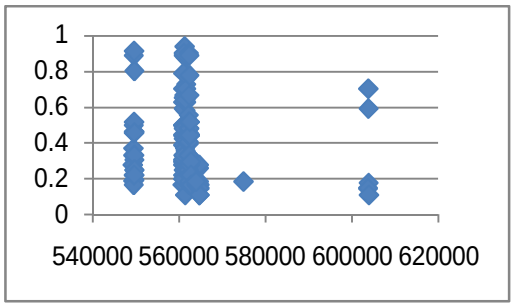

c (3050001 N – 3055000 N)

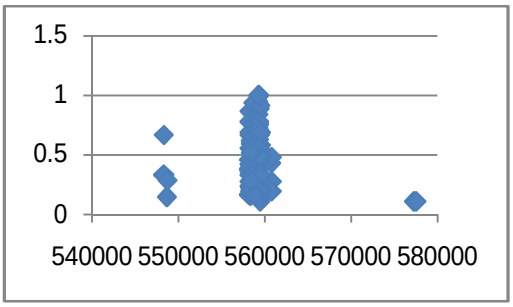

d (3055001 N – 3060000 N)

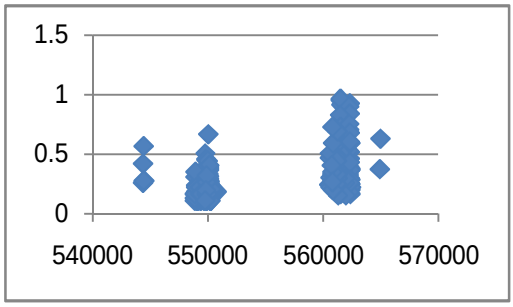

e (3060001 N – 3065000 N)

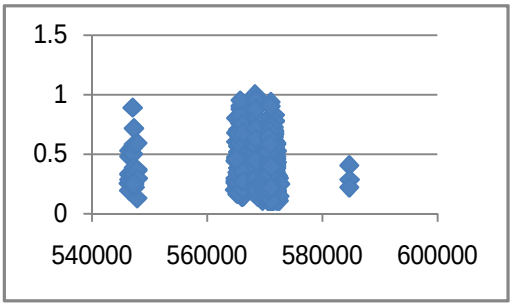

f (3065001 N – 3070000 N)

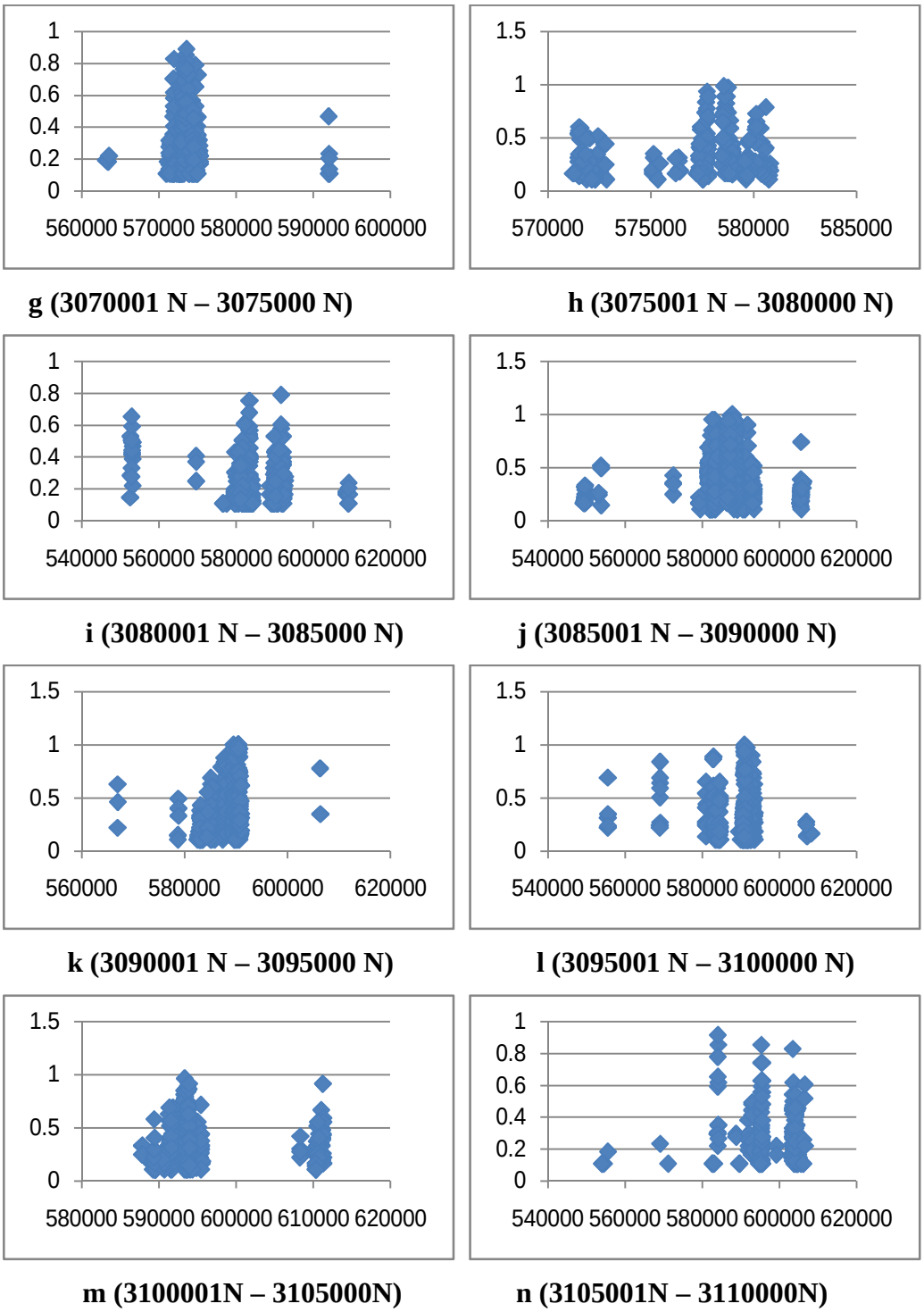

Fig. 7.3: Abundance values wrt longitudinal Coordinate for SAM classified image

The analysis of the statistical data plots and classified output indicate that the albitite pixels falling in the latitudinal range of 3040000 N – 3050000 N (Fig. 7.3 a & b) may be ruled out for further consideration since their location is at a significant distance from the reported albitite zone. These may be attributed to classification error. Fig. 7.3 c & d correspond to Salwari area which falls in the middle section of the reported albitite zone. The figure indicates that the pixels of interest abound mostly 555000 E to 5630000 E thus indicating the width of the albitite zone. A few outliers are observed at 550000 E and 604000 E. Fig. 7.3 e corresponds to Guhala area which also lies in the middle section of the albitite zone. In this area the albitite abundance is indicated in the longitudinal range 560000 E to 563000 E. A significant outlier is observed at 550000 E. On examination of the image and abundance map, it was analyzed that even though pixel density is considerable, however the abundance value is less. Fig 7.3 f corresponds to Pachlagi area. The albitite abundance is witnessed in the longitudinal range from 565000 E to 572000E. A few outliers are observed at 548000 E and 585000 E. The latitudinal section ranging from 3070001 N to 3075000 N in Fig. 7.3 g indicates the albitite abundance in the region 5710000E to 5760000 E with a few misclassified pixels at 563000 E and 5920000 E. Fig. 7.3 h corresponds to Mavanda Tarla and Kushwali Dhani area. Field data collection was carried out in this area at selected locations. Rock samples of different stages of albitization were collected for laboratory analysis. In this area the albitite zone stretches from 572000 E to 582000 E. Fig. 7.3 i correspond to Lakha area where albitite zone ranges from 580000 E to 591000 E. A few outliers are observed at 551000 E and 610000 E. Fig. 7.3 j corresponds to latitudes ranging from 3085001 N to 3090000 N. This area lies in the north section of the reported albitite zone. In this area the albitite abundance is seen from 581000 E to 592000 E. A few misclassified pixels are also observed at 550000 E and 605000 E. Fig. 7.3 k corresponds to Mewara Gurjawas area in the field. This also forms the main area in the north zone of albitite zone. Here albitite occurs between 582000 E to 590000 E. Fig. 7.3 l corresponds to Mewara Jatuwas area. The albitite zone extends from 584000 E to 593000 E. A few outliers are observed at 555000E and 570000 E. Fig. 7.3 m & n further north of the Mewara Jatuwas area show major occurrence of albitite from 589000 E to 595000 E. with a concentrated outlier at

610000 E. These outlier pixels are located at significant distance from the albitite zone and exhibit low abundance.

Analysis of Fig. 7.3 indicates a maximum extent of 11 km for the albitite zone. Fig. 7.4 depicts the albitite zone demarcated in totality from SAM algorithm. This result is in concurrence with the available literature, which states that the extent of the zone is 8 -10 km (Yadav *et al*., 2000). It is observed that the majority of pixels classified as albitite fall within the designated albitite zone, however a small patch of albitite is also observed near Gura, around 9.5 km from the western fringe of the albitite zone. A few pixels near Kurl ki Dhani and Bansiyal are also classified as albitite and forming a linear pattern with the Gura patch. In the eastern part of the study area small scattered patches are found from Tatia ki Dhani to Jhilo. Further field investigation may be carried out to confirm the presence of albitite in these areas. Details related to location name in the map have been given in Table 6.7.

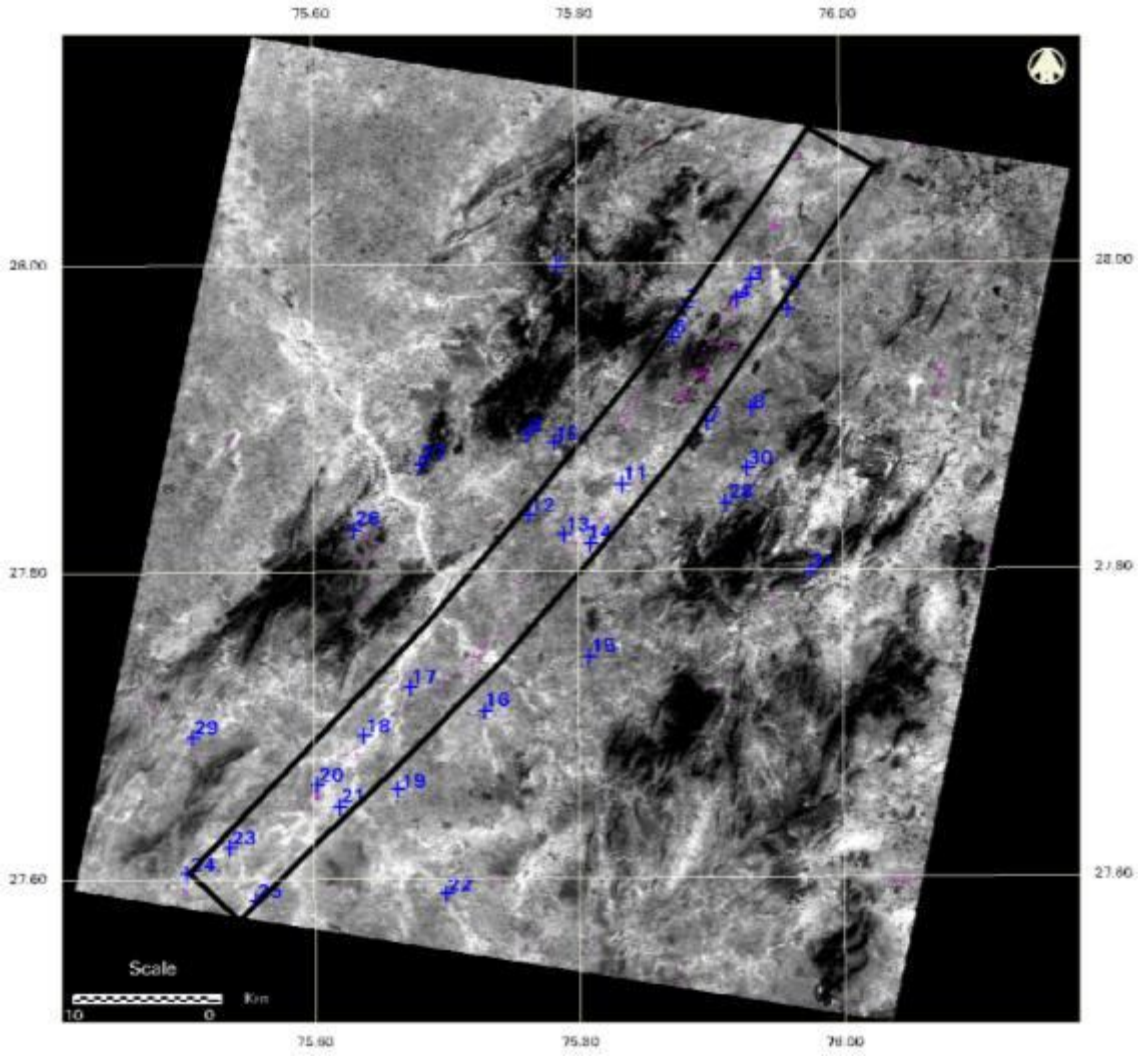

Fig. 7.4: Albitite Zone classified using SAM Algorithm

The albitite abundance image from SFF algorithm was also statistically analyzed in a manner similar to the above mentioned procedure. The spatial extent of albitite for SFF classified image ranges from 3045000 N to 3110000 N. Accordingly the area is divided into 13 zones of 500 m each. Fig. 7.5 depicts the graphs for albitite abundance with respect to longitude range for SFF algorithm.

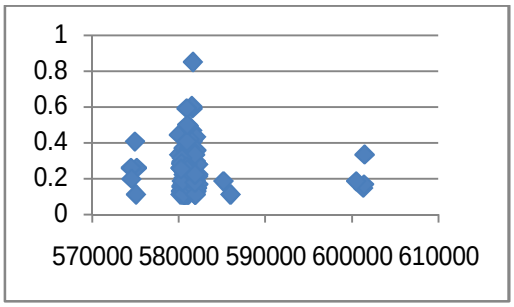

a (3045001 N – 3050000 N)

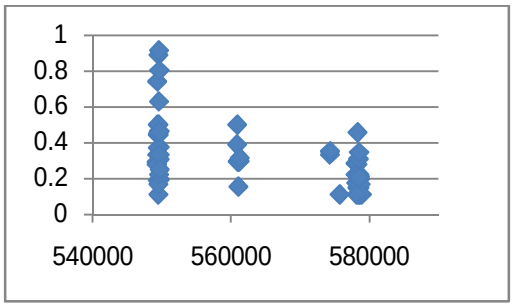

b (3050001 N – 3055000 N)

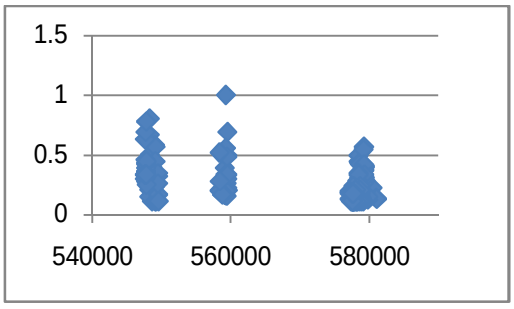

c (3055001 N – 3060000 N)

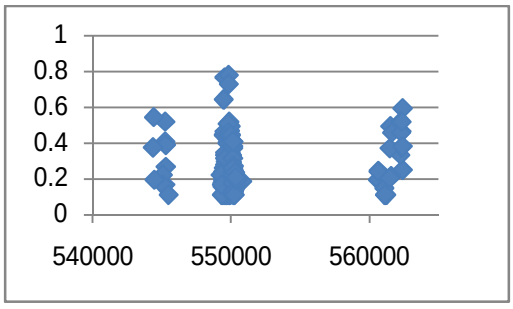

d (3060001 N – 3065000 N)

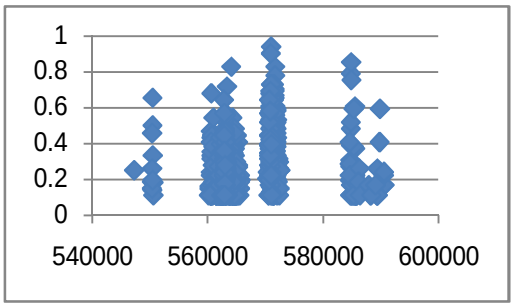

e (3065001 N – 3070000 N)

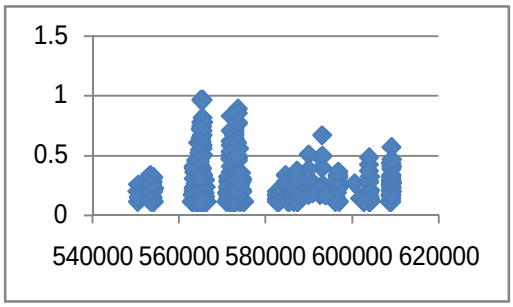

f (3070001 N – 3075000 N)

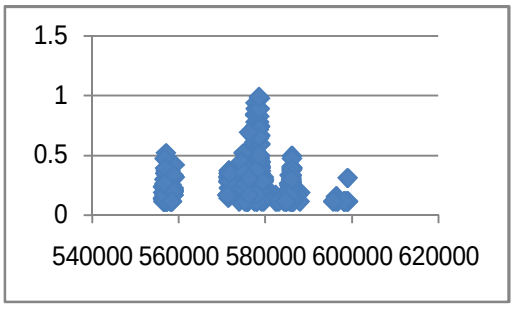

g (3075001 N – 3080000 N)

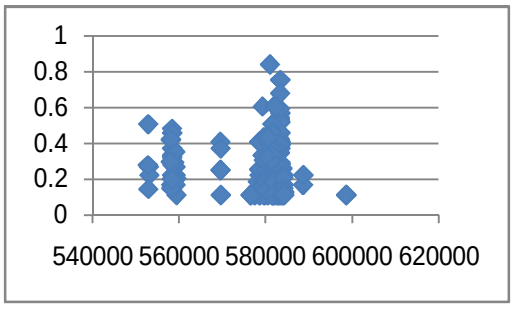

h(3080001 N – 3085000 N)

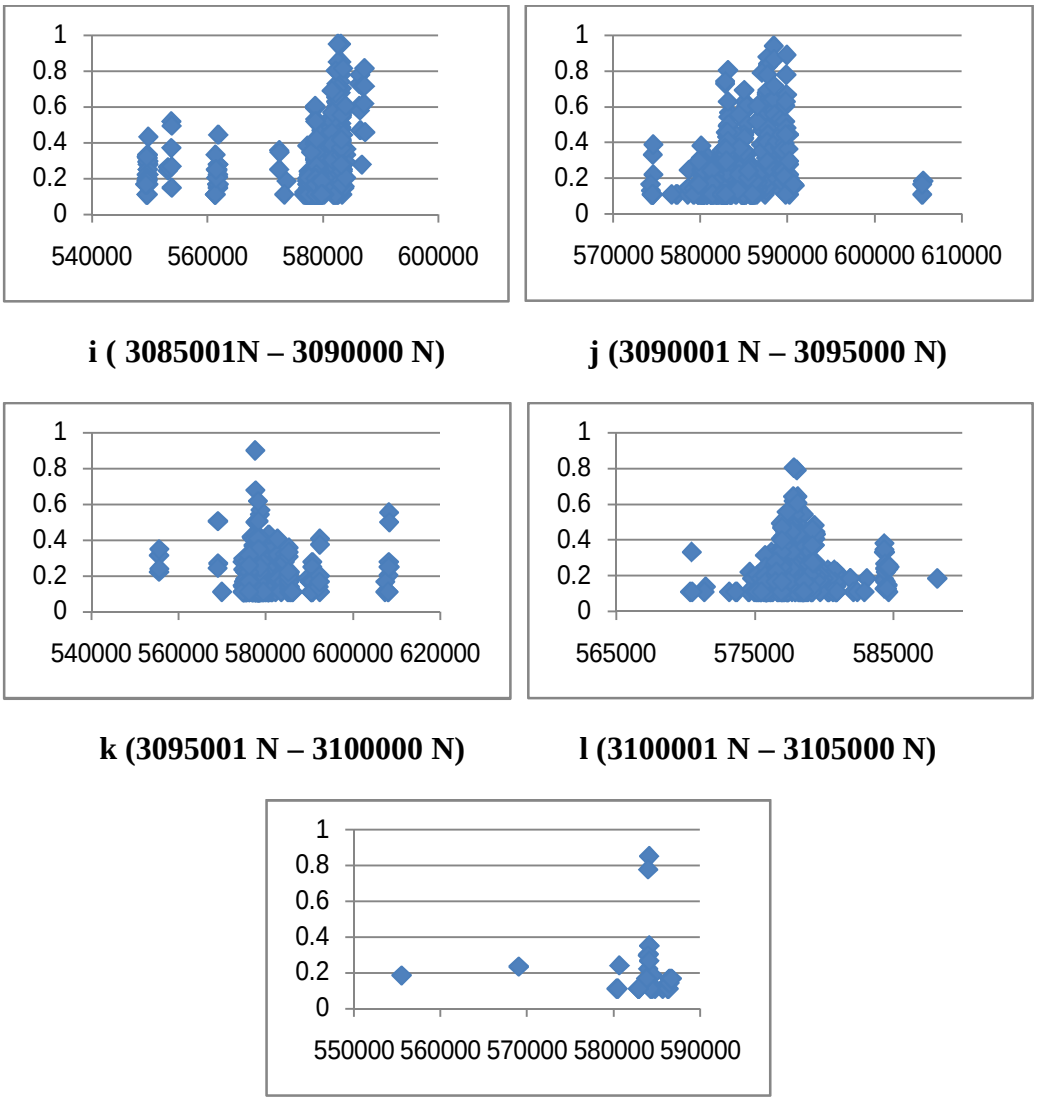

i (3085001N – 3090000 N)

j (3090001 N – 3095000 N)

k (3095001 N – 3100000 N)

l (3100001 N – 3105000 N)

m (3105001 N – 3110000 N)

Fig. 7.5: Abundance values wrt X Coordinate for SFF classified image

The analysis of the data plots and SFF classified image indicate that the albitite pixels falling in the latitudinal range of 3045000 N – 3055000 N (Fig. 7.5 a and b) may be exempted for further analysis as it is quite far off from the reported albitite zone. Thus these pixels might be misclassified pixels. Fig. 7.5 c indicates occurrence of albitite pixels from 549000 E to 559000 E. An outlier with low abundance value is observed at 578000 E. Fig. 7.5 d corresponding to Guhala area lies in the middle section of the albitite zone. In this area three albitite patches are located at 550000 E, 561000 E and a few outlier pixels at 545000 E. Fig. 7.5 e corresponds to Pachlagi area. The albitite

abundance is witnessed in the longitudinal range from 560000 E to 571000E. A few low abundance classified pixel are observed at 550000 E and 585000 E, which may be attributed to errors in classification. The latitudinal section ranging from 3070001 N to 3075000 N in Fig. 7.5 f indicates the albitite abundance in the region 5630000E to 5720000 E with scattered outliers of low abundance in neighbouring areas. Fig. 7.5 g corresponds to Mavanda Tarla and Kushwali Dhani area. In this area the albitite zone stretches from 571000 E to 580000 E, outliers occurring at 558000 E, 585000 E and 600000 E. Fig. 7.5 h corresponds to Lakha area where albitite zone ranges from 576000 E to 585000 E. A few scattered outliers are observed at 560000 E. Fig. 7.5 i corresponding to latitude range 3085001 N to 3090000 N lies in the north section of the reported albitite zone. In this area the albitite abundance is seen from 578000 E to 585000 E with a few scattered outliers to the west of the albitite zone. Fig. 7.5 j corresponds to Mewara Gurjawas area in the field. This forms the main area in the north part of albitite zone. Here concentrated albitite occurrences are observed from 579000 E to 590000. Fig. 7.5 k corresponds to Mewara Jatuwas area. The albitite zone extends from 574000 E to 586000 E. Fig. 7.5 l corresponding to latitude 3100000 N to 3105000 N also indicate major occurrence of albitite from 575000 E to 581000 E. In Fig. 7.5 m few albitite pixels are observed at 585000 N.

Analysis of Fig. 7.5 indicates that the maximum extent of albitite zone classified with SFF algorithm is 12 km. Fig. 7.6 depicts the albitite zone demarcated in totality from SFF algorithm. Even though the majority of albitite patches are falling within the demarcated albitite zone, however a small patch of albitite is also observed near Gura, though the size is smaller than the SAM classified image. A few scattered patches are also observed in a linear extension from Chanth to Chawra about 10 km from the western boundary of the albitite zone. Towards the eastern edge a small patch is observed at Balwar and a few scattered pixels are seen extending from Bhawa Singh ki Dhani to Patan. Extensive field and laboratory investigation might be required to ascertain the nature of these classified patches. Details related to location name in the map have been given in Table 6.7.

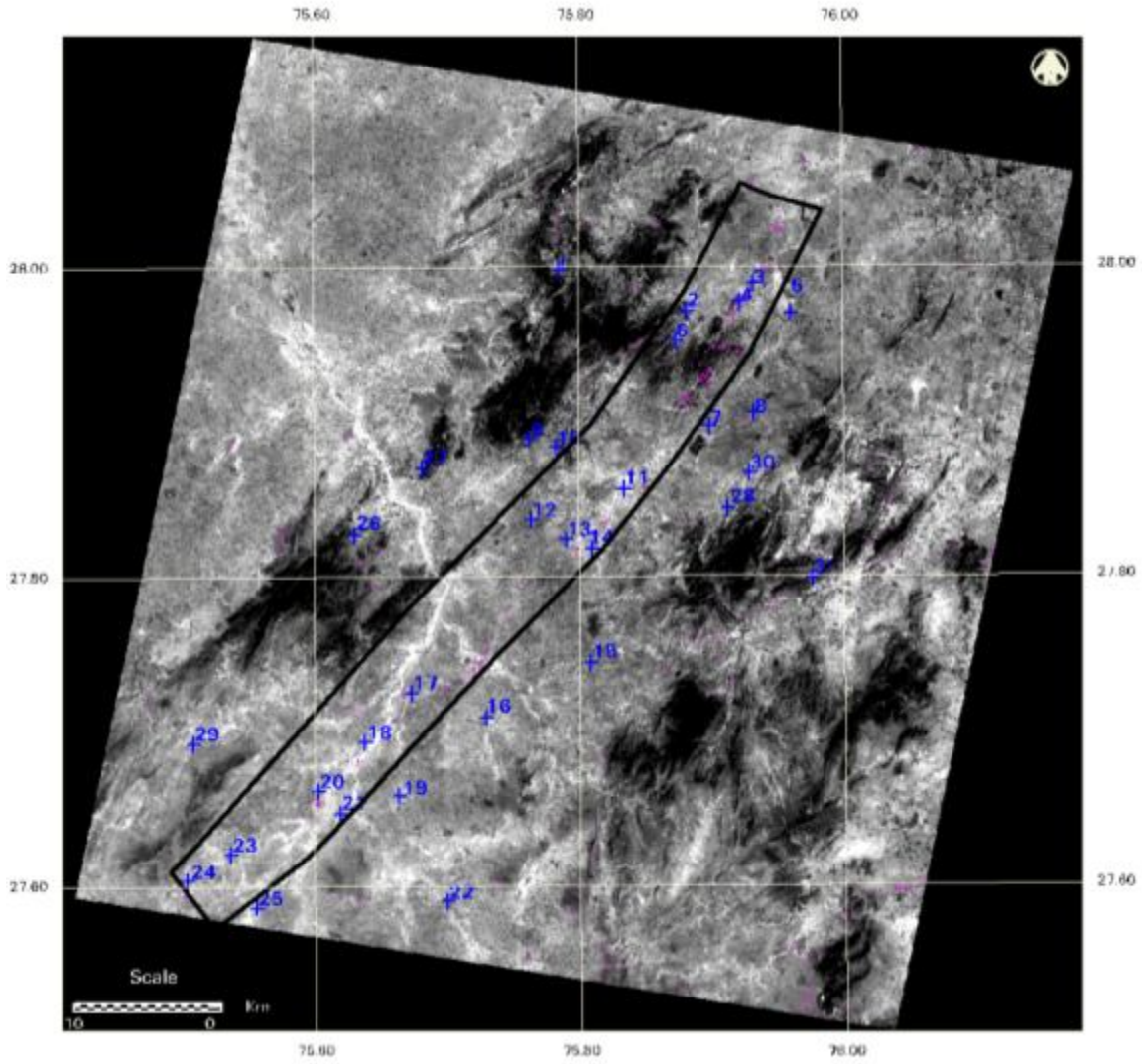

Fig. 7.6 Albitite Zone classified using SFF Algorithm

For MTMF classified image the albitite extent ranges between 3040000 N to 31100000 N. The graph plots show concentrated occurrences of albitite at few longitudes. The complete latitudinal range was again sliced into sections of 500 m each thus yielding 14 image sections. The statistical plots of albitite abundance versus longitude is shown in Fig. 7.7.

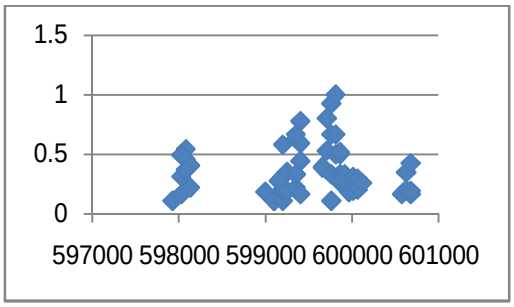

a (3040000 N– 3045000 N)

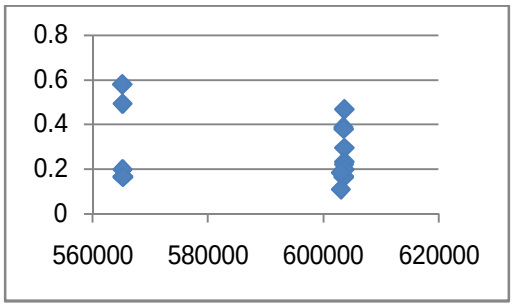

b (3045001 N – 3050000 N)

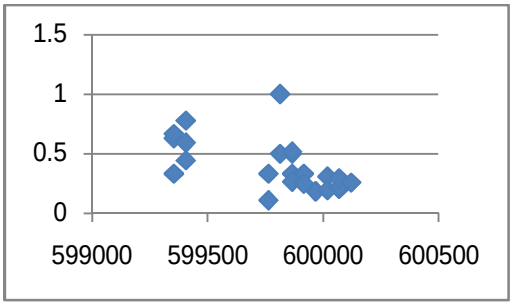

c (3050001 N– 3055000 N)

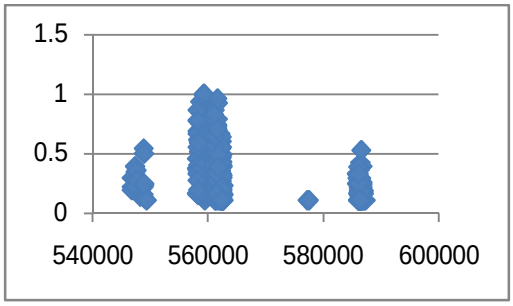

d (3055001 N – 3060000 N)

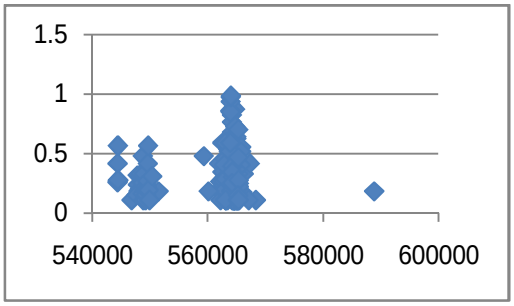

e (3060001 N – 3065000 N)

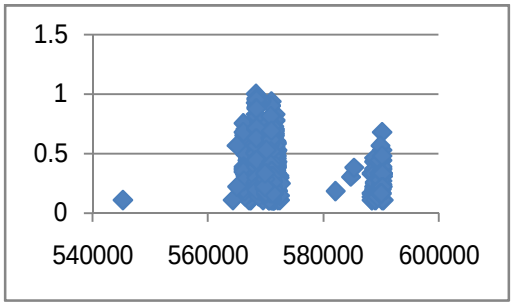

f (3065001 N – 3070000 N)

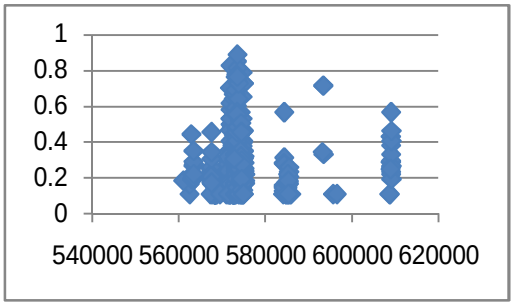

g (3070001 N– 3075000 N)

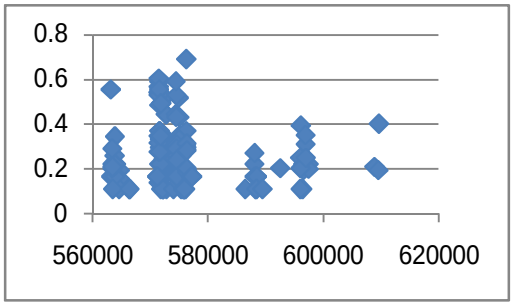

h (3075001 N – 3080000 N)

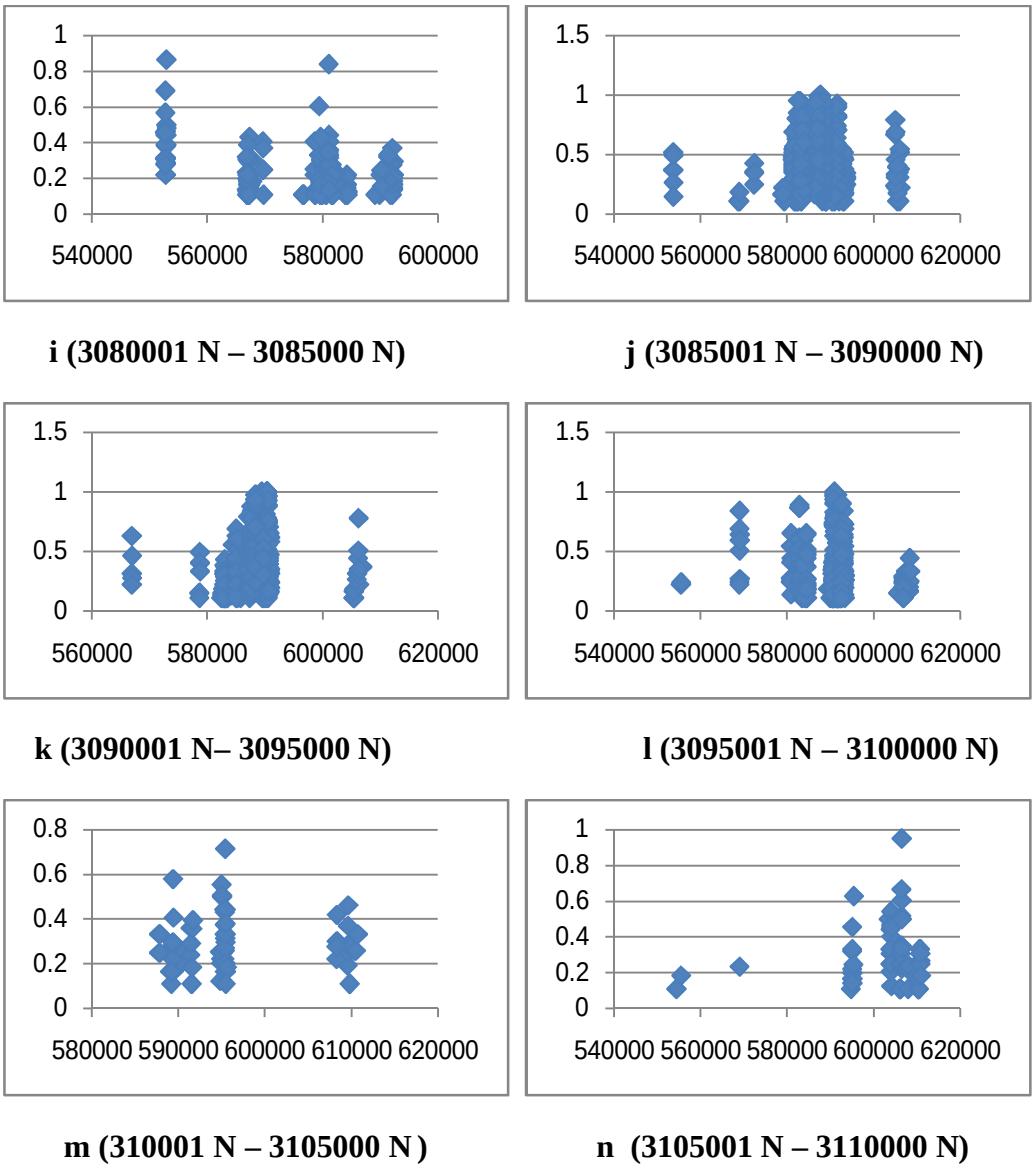

Fig. 7.7: Abundance values wrt X Coordinate for MTMF classified image

The analysis of the statistical data plots and classified output indicate that the albitite pixels falling in the latitudinal range of 3040000 N – 3055000 N (Fig. 7.7 a, b & c) may be ruled out for further consideration due to scatted low abundance pixels at considerable distance from the reported zone. Fig. 7.7 d corresponds to Salwari area located in the middle part of the albitite zone. The figure indicates that the albitite pixels abound mostly

in the range 558000 E to 5620000 E thus indicating the width of the albitite zone. A few outliers are observed at 549000 E and 589000E. Fig. 7.7 e corresponds to Guhala area also in the middle part of the albitite zone. In this area the albitite abundance is indicated in the longitudinal range 562000 E to 568000E. A significant outlier is observed at 550000 E. Observation of the image and abundance map indicates that this outlier shows low pixel density and abundance values. Fig. 7.7 f corresponds to Pachlagi area. The albitite abundance is witnessed in the longitudinal range from 566000 E to 572000E. A few outliers are observed at 590000 E. The latitudinal section ranging from 3070001 N to 3075000 N in Fig. 7.7 g indicates the albitite abundance in the region 5660000E to 5750000 E with scattered misclassified pixels at 563000 E, 5880000 E and 610000 E. Fig. 7.7 h corresponds to Mavanda Tarla and Kushwali Dhani area. Field data of different stages of albitization were collected for laboratory analysis. In this area the albitite zone stretches from 571000 E to 578000 E with scatted low abundance outliers on both sides of the zone. Fig. 7.7 i corresponds to Lakha area. In this area albitite zone ranges from 579000 E to 585000 E, outliers occurring at 551000 E, 568000 E and 591000 E. Fig. 7.7 j corresponds to latitudes ranging from 3085001 N to 3090000 N. This area lies in the north section of the reported albitite zone. In this area the albitite abundance is seen from 581000 E to 592000 E. A few misclassified pixels are also observed at 551000 E, 571000 E and 608000 E. Fig. 7.7 k corresponds to Mewara Gurjawas area in the field. This forms the main area in the north part of albitite zone. Here albitite occurs between 582000 E to 590000E. Fig. 7.7 l corresponds to Mewara Jatuwas area. The albitite zone extends from 582000 E to 592000 E. A few outliers are observed at 609000E and 570000 E. Fig. 7.7 m further north of the Mewara Jatuwas area show a few scattered occurrences of albitite in the reported zone. An outlier is also observed at 610000 E. Fig. 7.7 n exhibit scattered pixel occurrences at 610000 E. These outlier pixels are located at significant distance from the albitite zone.

Analysis of Fig. 7.7 indicate a maximum extent of 10 km for the albitite zone. Fig. 7.8 depicts the albitite zone demarcated in totality from MTMF algorithm). Outside the designated albitite zone, towards the western part a considerable patch is observed near Gura. Few pixels are also classified as albitite on the western fringe of Madhogarh block protected forest. Towards the eastern edge of the albitite zone, a small patch is observed

at Tatia ki Dhani. A few scattered patches are also observed from Bhawa Singh ki Dhani to Patan. These areas need to be thoroughly surveyed to check whether these pixels are misclassified pixels or albitite is exposed in the area. Details related to location name in the map have been given in Table 6.7.

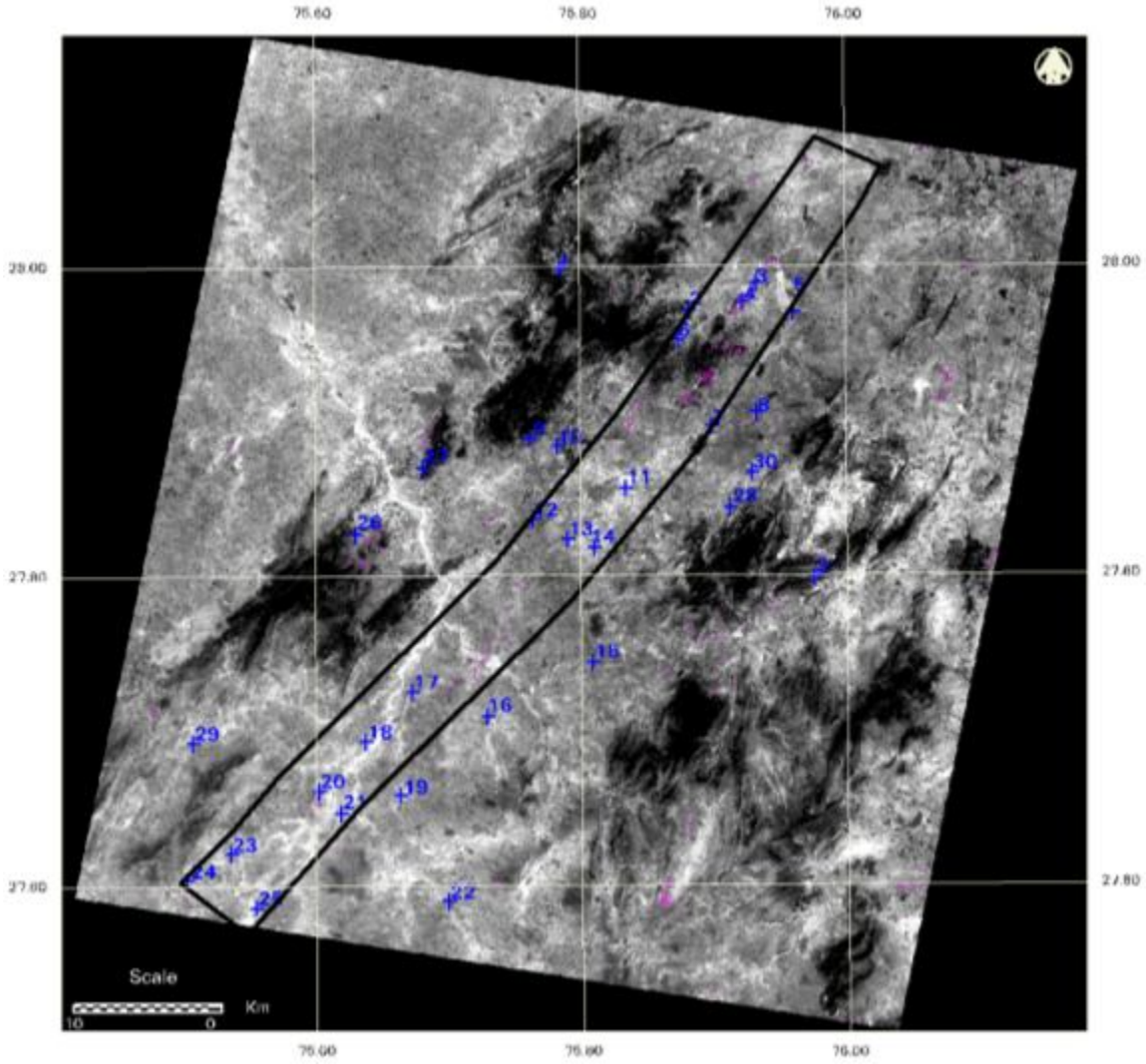

Fig. 7.8: Albitite Zone classified using MTMF Algorithm

7.4 SYNTHESIS OF RESULTS AND INTERPRETATION

The results of a research study need to be compared systematically with an authentic reference before arriving at scientifically logical conclusions. Thus in order to assess the credibility of the results it is necessary to analyze them in light of existing evidences. The next sections will cover the findings for each category and draw a brief conclusion.

For analyzing the atmospheric correction, the reflectance spectra of corrected image were analyzed with the lab spectra from JHU Library. Except band 1, 2 and 4, where the corrected reflectances were lower than the reference, the remaining bands exhibited a close correlation with reference spectra which indicates that FLAASH and ATCOR are suitable algorithms for atmospheric correction of ASTER data.

Synthesis and interpretation of the results of albitite mapping using the ASTER data have been done by simultaneously examining the compiled reference lithologic map, mineralogical and textural data obtained from microscopic study of the thin-sections of field samples with their GPS-locations, and spectral classification results for the three classification algorithms. Six field samples were utilized for generation of reference spectra of albitite and then classifying ASTER data using Spectral Angle Mapper, Mixture Tuned Matched Filtering and Spectral Feature Fitting algorithm. Since site-specific field samples from these areas have been analyzed petrographically and spectrally, other eleven locations have been used to validate the results of albitite mapping based on the available literature. The accuracy of classifications was found to be 72.72%, 63.63% and 63.63% respectively. For demarcation of albitite zone in the study area, the abundance of albitite was plotted with respect to longitude. It was observed that using all the three algorithms we are able to demarcate the albitite zone and the width of the zone is 10 - 12 km. This result is in concurrence with the available literature, which states that the extent of the zone is 8 – 10 km (Yadav *et al.*, 2000).

An important observation after synthesis of results highlights few locations outside the designated albitite zone exhibiting similar spectral characteristics as albitite. A few noteworthy ones being a linear extension of scattered pixels extending from Madhogarh to Gura upto Kurl ki Dhani running parallel at a distance of approximately 10 km to the western boundary of the confirmed zone. Towards the eastern fringe a short linear extension is observed from Tatia ki Dhani to Jhilo about 6 km and running parallel to the zone boundary. An isolated patch is also observed further southeast of Jhilo at Patan approximately 7 km from Jhilo (Fig 7.9). The names of major locations in the area are given in the Table 6.7. These probable patches of albitite as brought out by multisensor investigation and digital image classification techniques will provide crucial understanding for further geological exploration in the area. Once confirmed after field

verification these yet undiscovered patches are expected to throw new light on geological setting of the albitite zone.

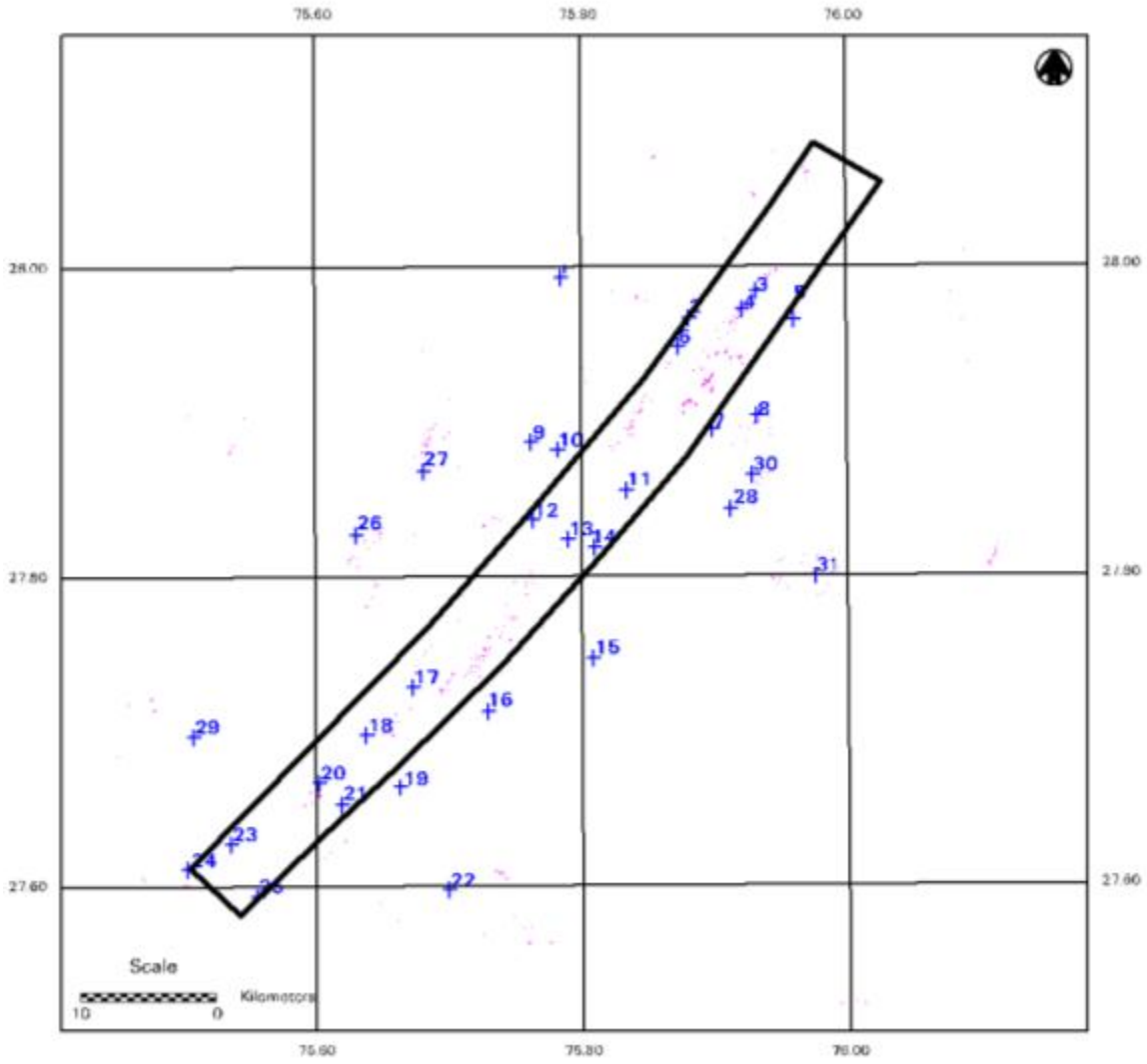

Fig. 7.9: Locations outside the albitite zone exhibiting high spectral similarity to albitite

From comparative examination of albitite in the classification results for three classification algorithms used in spectral analysis, it has been observed that ASTER data has been successful in spectrally identifying surface occurrences of albitite. Ambiguities and differences in albitite identification for different algorithms investigated have arisen primarily because of limitations of ASTER's spectral resolution resulting in multiple (and sometimes erroneous) matches of the pixel spectrum with reference spectral library.

Also, residual effects of vegetation within an average pixel area of 30x30 m^2 also add to the difficulty in exact identification. The results show that the ASTER data can provide fast and dependable support in identifying and mapping specific minerals which can be linked with the presence of economic mineralization.

7.5 SUMMARY OF CONCLUSIONS

The success of remote identification and mapping of surface materials is governed by the unique retrieval of their spectral signatures. Credible radiometric, atmospheric and topographic corrections are vital in the reliable application of remote sensing in geology. This study has demonstrated that methods of atmospheric correction utilizing principles of radiative transfer can effectively achieve this objective, but availability of local atmospheric data for the image (constrained by date, time and area) are necessary. Useful improvements can be made by combining image-based approaches with these methods.

Digital image processing techniques such as band ratios and DPCA were implemented on both Landsat and ASTER dataset. These techniques offer geo scientists a cost and time efficient solution for regional mineral and lithological mapping. Subtle changes in spectral reflectance recorded across various wavelength regions (specifically VNIR-SWIR and TIR) form an important basis for identification of individual minerals.

The investigation and analysis of visible, near infrared (VNIR), short wave infrared (SWIR) and thermal infrared (TIR) wavelength regions highlighted the impact of combining VNIR/SWIR and TIR data for surficial albitite mapping. It was found that all the classification algorithms applied to the combined data resulted in improvement in overall accuracy of classification. The synergistic use of VNIR, SWIR, and TIR data complement one another and hence improve the ability of remote detection, identification and mapping of albitite.

Mineral mapping based on ASTER data processing has revealed the specific advantages of ASTER over the existing spaceborne remote sensors. ASTER provides data in a wide spectral region spanning from the visible to the thermal infrared with improved spatial, spectral and radiometric resolution. The TIR data enables identification of quartz, mafic minerals and carbonate rocks, the SWIR bands diagnose the characteristic spectral

features of hydrothermal alteration associated with hydroxyl, sulfate and carbonate minerals and the three VNIR bands are provide important information pertaining to absorption in transition metals especially iron and some rare-earth elements (REE). These properties highlight the significant advantages of using ASTER since this data enables the analysis of the complete range of the electromagnetic spectrum most useful for geoscientists in terms of mineral identification.

In the present study identification and mapping of albitite has been successfully achieved using ASTER data. The results were acceptable because of field spectral data collected from the ground, since it gave a truly representative end-member spectrum for albitite, used in spectral classification. Mapping albitite using satellite images facilitates in detecting uranium occurrences which are expected to have a significance impact in locating economically viable albitite hosted uranium deposits. The study is based on qualitative analysis of spectral similarity measures for identification of albitite as spectroscopic principles have not been utilized due to limitations in availability of higher spectral resolution image data.

To summarize, the most significant contribution of this research is the creation of spectral signature for adventuring albitite in Indian scenario. This is also a first attempt of delineating albitite zone of eastern Rajasthan using multisensory remotely sensed images. The analysis of data from multiple sources has resulted in spatial demarcation of albitite zone over the region. Apart from reported zone other probable albitite occurrences, which need to be validated through ground observation have been brought out based on digital image classification.

The credibility of target mineral mapping results is largely influenced by the spatial and spectral resolution. The factors of spectral mixing in relatively large areas represented in a single 30x30 m^2 pixel of the ASTER data lead to spectral flattening and loss of absorption features. This is an area with a scope of further improvement. The end members in TIR range for identification of albitite were generated using sample location in the image. Significant improvement in classification is expected if the ground instrument enabled spectra collection in thermal range is included.